UC Berkeley
UC Berkeley Electronic Theses and Dissertations

Title

Understanding and Engineering Surface and Edge Defects of Transition Metal Dichalcogenides

Permalink

https://escholarship.org/uc/item/60p2f9cb

Author

Zhao, Peida

Publication Date

2018

Peer reviewed|Thesis/dissertation

Understanding and Engineering Surface and Edge Defects of Transition Metal Dichalcogenides

By

Peida Zhao

A dissertation submitted in partial satisfaction of the

requirements for the degree of

Doctor in Philosophy

in

Engineering – Electrical Engineering and Computer Science

in the

Graduate Division

of the

University of California, Berkeley

Committee in charge:

Professor Ali Javey, Chair

Professor Ming C. Wu

Professor Daryl Chrzan

Spring 2018

Abstract

Understanding and Engineering Surface and Edge Defects of Transition Metal
Dichalcogenides

by

Peida Zhao

Doctor of Philosophy in Engineering – Electrical Engineering and Computer Sciences

University of California, Berkeley

Professor Ali Javey, Chair

Since the inception of solid state semiconductors and device fabrication techniques, continuous scaling has been implemented as a key driver behind realizing faster electronics while optimizing for power consumption, improving the field in an exponential fashion (i.e. Moore's Law) and facilitating modern technological advances that otherwise would have been impossible. In recent years, transistor gate length has entered into the single nanometer regime, encountering significant engineering and cost challenges. While efforts at mitigating these challenges have extended the lifetime of silicon-based semiconductors (all-around gate FETs for example), a more fundamental overhaul of the transistor is needed for long term progress if Moore's law is to be upheld in terms of power reduction and performance improvement.

2D materials serve as an ideal candidate for addressing scaling issues on various fronts. Possessing atomic scale smoothness, varying band alignment, and desirable bandgap in the single layer limit, 2D transition metal dichalcogenides (TMD) material can serve as the active channel layer for transistors geared towards various different applications. Given their atomic smoothness and interlayer van der Waal interactions, 2D TMDs provides the intrinsic scaling advantage in the vertical axis while the ideal uniformity allows for predictability of carrier behavior across lateral areas. However, realistic integration of 2D TMDs into devices have been far from ideal, and the existence of both surface and edge defects on the system becomes the current bottleneck prohibiting any realistic integration of 2D TMDs into modern devices. In this report, we examine both surface and edge defects of 2D TMDs, their effects on carrier movements and recombination, establish an analytical model of defect analysis, and introducing a new approach to TMD patterning considering effects on the resultant edges.

Specifically, the surface defects on tungsten diselenide (WSe_2) will be discussed in relation to traditional field effect transistor applications, and how we can take advantage of such surface defects and engineer them into sites of p-type doping via covalent functionalization. In this way, we demonstrate a 5 order of reduction in the contact resistance tunable degenerate doping.

Additionally, edge defects of tungsten disulfide (WS_2) are characterized by ways of experimentally measuring generated carrier recombination. A universal metric applicable to all 2D semiconductor is introduced here towards describing the edge defect quality called Edge Recombination Velocity (ERV). A qualitative discussion of the edge defect will also be presented here with respect to edge etching methods, differences in the 2D material chosen, and intrinsic edge orientation.

Finally, we demonstrate scanning probe lithography (SPL) as a reliable top down method towards nanoscale patterning of 2D materials, and expand the ERV characterization platform to MoS_2, $MoSe_2$, WS_2, and WSe_2. Additionally, we demonstrate that through SPL, different materials possess drastically different ERVs, highlighting the lessened impact of the process induced edge defects, establishing a platform for material-based edge passivation experiments.

Acknowledgements

I would like to first and foremost thank Professor Ali Javey for giving me the opportunity to work in his lab. His hands-on approach, encouragements, and support have all allowed me to not only learn a great deal about conducting experiments, but more importantly problem-solving skills and setting a vision for the direction of research. This realization helped me think about research in a meaningful way and allowed me to conduct my experiments with purpose.

In addition, I would like to thank Professor Ming Wu and Daryl Chrzan for being on my dissertation committee, and the insightful comments you have all made about my work.

I would also like to thank Professor Eli Yablonovitch for serving on my qualification committee. Your feedback has made me think on a deeper level for my research topics.

Next, I would like to thank my lab members. Hui Fang, Rehan Kapadia, and Daisuke Kiriya have all been invaluable mentors to me during my formative Ph.D. years, constantly giving me sound advices and offering encouragements through difficult times. Mahmut Tosun showed me the importance of humility and intelligence. His research insights, coupled with his willingness to share self-deprecating humors helped me become a better person. Sujay Desai is without a doubt, one of the most intelligent people I have ever met. Mark Hettick always astounds me with his great memory, and the encyclopedic knowledge of any topics we could be discussing. They have been my "brothers in the trenches": same year colleagues who have supported and helped each other throughout this journey. Danny Lien and Geunho Ahn have been incredible friends during my last few years at Ph.D., offering insights and introducing me to great restaurants in the bay area. Kevin Chen, James Bullock and Thomas Rembert have been great friends, those I always trust to share things and come out feeling much better.

There are so many others: Matin, Fahad, Aiden, Steve Chuang, Angada, Tania, Luke, Gary, Julia, Alla, Emma, Yasser, Nishita, Ben, Franiece, Dwi, Steve Volkman, Daniel, Oliva, Hector and many more, thank you all for making my Ph.D. such a great experience.

To my undergraduates, Fatih Dinc, and Leslie Wang: thank you for putting up with my incessant demands. I have learned just as much from you as you have from me. I wish you great success in the future.

Finally, I'd like to thank Will Scheideler, Rose Jin, and my mother. Will has become one of my closest friends in grad school. His positive outlook, subtle confidence, and humility have served as a compass during my time of crisis. He also pushed me to do snowboarding and ride down blacks without preparations. Rose has been an incredible pillar for me to lean on during my hectic days of graduation. Her unconditional support, encouragements, empathy and kindness has changed the way I look at the people around me. For mother, I'll just say thank you. You have done so much more for me than you'll ever know.

Table of Content

Chapter 1: Introduction

1.1 Scaling and Its Respective Challenges

The astoundingly fast advancements made in the modern information age is mostly hinged on the rapid technological advancements of solid state semiconductors. Residing at the heart of this progression is Moore's law, a self-evident empirical predictor for the growth of the semiconductor field,[1, 2] The law states that transistors are to halve in size per roughly every 18 months. The exponentially decreasing size directly translates to faster performance due to an increase in on-currents at less power, coupled with a higher areal density and increased functionality at the same physical chip size. This performance improvement has enabled the modern "smaller, faster, smarter" electronic devices to exist and is behind many of the higher level technological innovations.
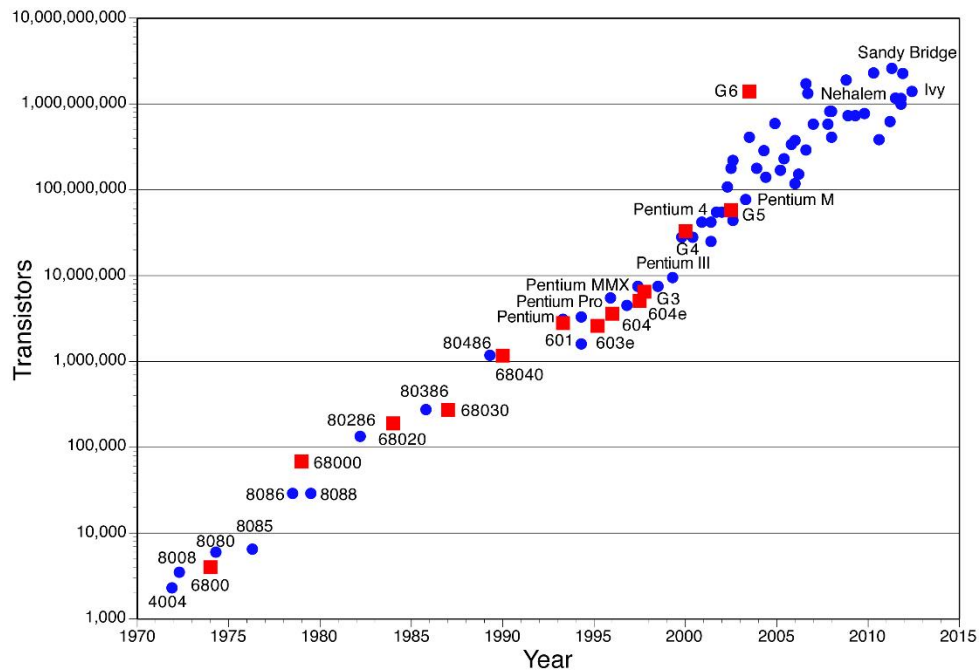
Figure 1.1. *A representative graph of number of transistors present on an Intel processor versus time. Note the roughly linear progression of transistor packing, corresponding to an exponential increase at a logarithmic plot in the y-axis.*

Presently, single nanometer gate length Fin-field effect transistors (FinFETs) have been achieved based on silicon/germanium utilizing extreme ultra-violet lithography (EUV).[3] While scaling is still viable in the near future, this highlights an urgency for alternatives towards performance enhancement, as the atomic dimension is only one order away. Additionally, scaling becomes incrementally more difficult as various length parameters enter the low 10s and single digit nanometer regime. Therefore, a combination of engineering and economical challenges has introduced significant barriers even ahead of the fundamental limit of the atomic scale.

On the processing and engineering front, defect tolerance has become much stricter, as the total number of atoms in the system continues to decrease.[4-6] This leads to both a requirement for cleaner and more stringent environmental and process control. A calculation for a 7nm channel length silicon means approximately ~20 silicon atoms (assuming a 0.2nm van der Waal radius) lined back to back. A single atomic defect becomes a 5% atomic defect, equivalent to 5×10^{-2} cm^{-1} or roughly 6×10^{18} cm^{-3} in unintentional doping. This number is potentially too high for proper channel performance for various device applications, and a singular atomic defect is already difficult to achieve. Additionally, processing challenges such as nanometer scaled lithography further complicates continuous scaling, with each new fabrication method bringing with it its own set of challenges and restrictions (an example being EUV requiring special optics and ultra-high vacuum environments).

Unsurprisingly, overcoming the aforementioned engineering challenges requires higher costs, and this cost increase has been mitigating the decreasing per-transistor cost that scaling is supposed to provide.[7] Figure 1.2 traces the cost of per-transistor in the last few years, and an obvious cost plateau is seen despite further scaling of node sizes.
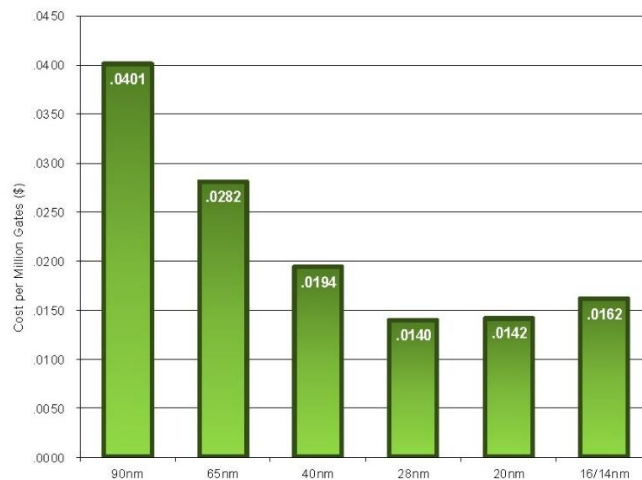
Figure 1.2. Cost per million gates as a function of node size. Note at 28nm and beyond, the cost has remained stagnant despite further size reduction. Factors such as more stringent process demands and new engineering challenges have played a key role in mitigating (or cancelling entirely) the cost reduction scaling is supposed to bring.[8]

Moving forward, a host of possible solutions have been proposed by the industry and academic research alike. From the more intuitive 3D integration of devices, to the more radical "electronic blood" idea of combining coolant and interconnects to mimic that of a biological system.[9, 10] In this work, we look to other 2D semiconducting material systems and probe some of their unique advantages that can potentially overcome the aforementioned problems of Moore's Law.

1.2 Transition Metal Dichalcogenides (TMD)

Transition metal dichalcogenides consist of the transition metal element (A) bonded to one of three chalcogens (B; sulfur, selenium, or tellurium) in the AB_2 stoichiometry. They exist as a family with many possible permutations, spamming from semimetal to semiconducting (Figure 1.3a). Structurally, they are arranged in a layer by layer configuration with a hexagonal unit cell, with in-plane covalent bonding while each layer is weakly bond via van der Waals interaction in the out-of-plane direction. Each collective TMD layer possesses 3 individual layers of atoms, resulting in a thicker monolayer (0.65nm) than graphene and a possible variation in the stacking periodicity both within a single layer (octahedral or tetrahedral configurations) and between the different layers (polytypes).[11, 12]
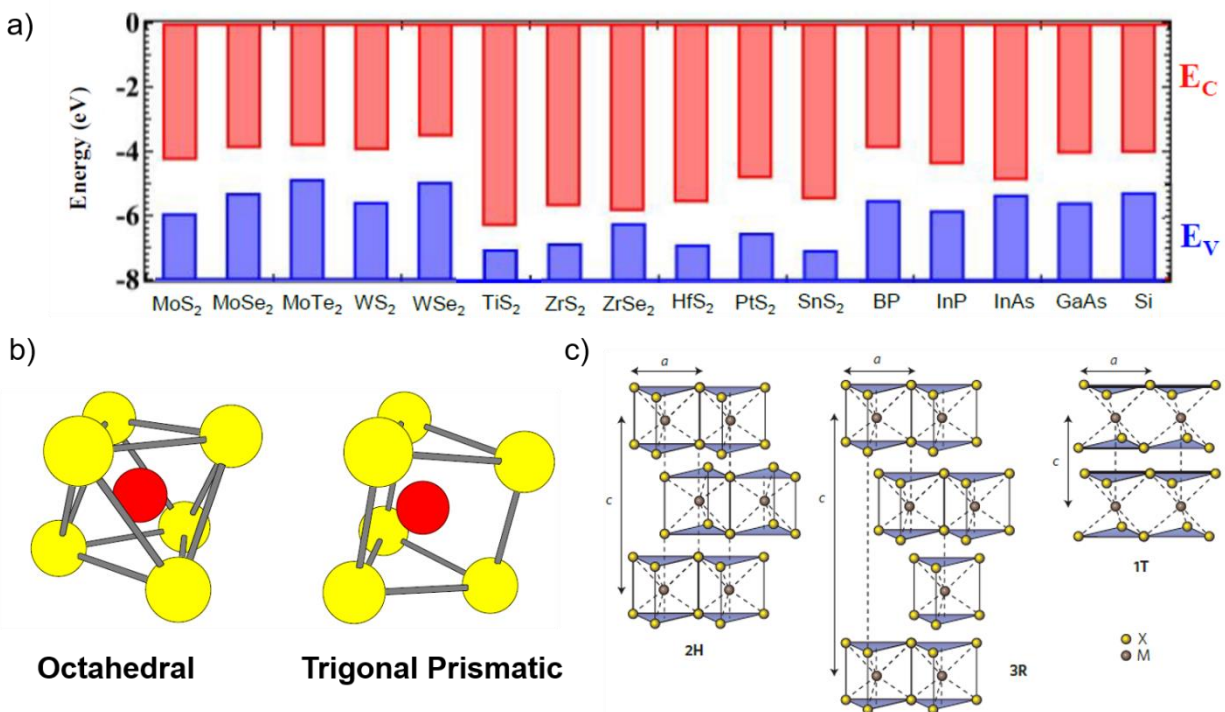
Figure 1.3. *a) Various TMDs and their respective bandgaps compared to other 2D materials and more traditional semiconductors such as silicon. b). Two possible configurations of stacking within each layer. The left side is known as "octahedral" while the right side is "trigonal prismatic". c). The various interlayer stacking periodicities that are possible along with the appropriate naming conventions.*[13]

Under ideal conditions, TMD possesses two traits that readily addresses the aforementioned scaling challenge in more traditional semiconductors while bringing TMDs directly to the scaling limit. First, each layer is to be free of dangling bonds on both its top and bottom surfaces. This is due to the van der Waals nature of their interlayer bonds. In comparison to other staple semiconducting materials such as III/Vs, silicon or germanium, one of the TMD's three dimensions can be scaled down, free of defects, at the cost of minimal energy. At the monolayer regime, TMD effectively becomes a surface

and edge system, and the surface is energetically inclined to be pristine. This ideality ensures uniformity in the band structure and addresses the stringent defect tolerance that exists due to nanometer scaling. Second, the low energy intra-layer van der Waal interaction means that scaling becomes trivial in the z-direction as minimal energy is required to achieve such pristine surface.

This thesis will address some key understanding and engineering techniques developed for addressing the various practical defects that can exist in 2D materials, and how these understandings can impact the progression of 2D material research applied towards future nanoelectronics. The rest of chapter 1 will lay down some nuances of the 2D material system relevant for later discussions.

1.2.1. TMD Layer Dependence

Due to the unique structure of such 2D materials, important material properties will also vary depending on the number of layers stacked together. The most obvious example is the properties of various monolayers possessing direct bandgap, while transitioning into indirect bandgap as layer number increases to 2 or above. The most studied TMDs known to possess such properties are MoS_2, WS_2, $MoSe_2$. Figure 1.4 shows both the experimental and theoretical validation of drastic band structure change from mono- to multi-layers:
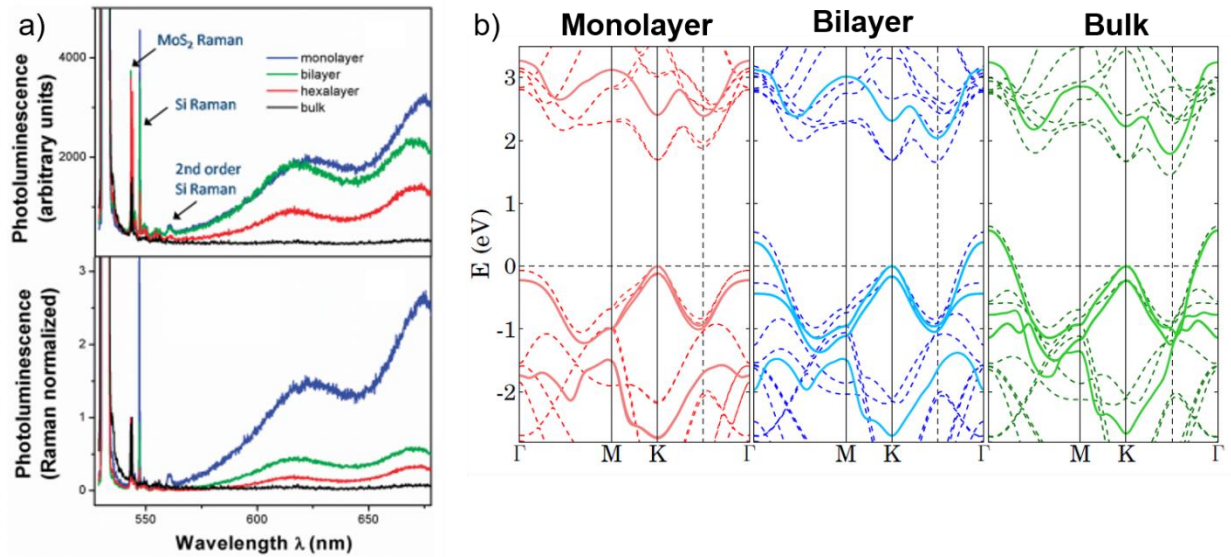
Figure 1.4. a) (top) Measured Raman spectroscopy and photoluminescence of MoS_2 as a function of different layers. After adjusting for Raman intensity (bottom), a clear trend of much brighter MoS_2 is seen by comparison. b). Density functional theory calculated MoS_2 band structure for mono-, bi-, and bulk layers. A clear indirect to direct transition is observed for layer thickness moving from mono to multi. The dashed line signifies local density approximation (LDA) while the solid line signifies GW approximation.[14, 15]

1.2.2. Excitonic System

Interestingly, 2D materials share a similarity with other low dimensional systems (organic photovoltaic materials, low dimensional silicon, germanium, III/Vs, and perovskites) in possessing excitons as a dominated carrier transport mechanism compared to the free electrons/holes. Excitons are coupled single electron and hole pairs weakly bonded to each other after energy or free carrier injection into the TMDs. They are electrically neutral and modelled as a quasi-particle similar to hydrogen atoms with their own energy levels. Generally, the energy required to break free the exciton into its constituent parts is called the binding energy. Under equilibrium, the bonded electron of an exciton rests on an energy level lower than the conduction band edge by an amount equal to the exciton binding energy. This added inter-carrier interaction produces complex characterization results. Photoluminescence of monolayer TMDs for example, will no longer produce energy relative to the actual band gap, but that of the bandgap minus the excitonic energy. Additionally, different energy excitons and quasi-particles (excitons from different valence band split off, direct and indirect conduction band valley, and charged trions consisting of 2 electrons with 1 hole or vice versa) can all co-exist in TMDs, resulting in multiple energy peaks in photoluminescence measurements.[15, 16] Finally, these species are also reflected in the absorption of TMDs each with their own distinct peaks.[17]

Overall, characterizations (especially optical) of TMDs can be harder to interpret due to this added carrier complexity. This introduction is to set a starting point for later discussions in this work where optical characterization techniques are implemented and their data interpreted with relation to TMD defects.
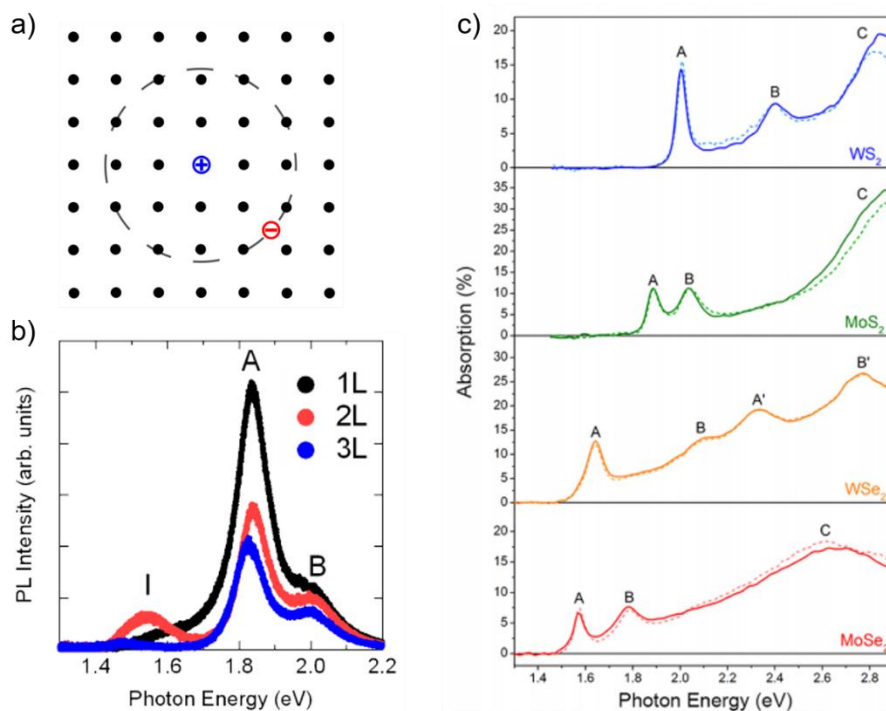
Figure 1.5. *a). Basic structure of an exciton, where a rough hydrogenic atom interaction happens across the periodic crystal potential lattice between a free-moving hole and electron. b). Layer dependent MoS$_2$ PL spectra, where A and B refers to excitons originating from 2 different valence band peaks respectively, with I indicating indirect valley transition c). Experimentally measured absorption of WS$_2$, MoS$_2$, WSe$_2$, and MoSe$_2$, all absorption peaks accounted by different exciton levels.*

1.2.3. Bandgap

A significant complication arises from an excitonic system is the lack of accurate means for bandgap determination. Usual optical characterization methods such as PL and absorption measurements depends on two factors for accurate data: 1. Optical transitions are band-to-band 2. No significant defect states exist close to either the valence or conduction band to hamper the observation of sharp absorption onset for band edge fitting after absorption measurements. As discussed in 1.2.2., the unique exitonic system of TMD, coupled with the myriad of quasi-particle species that can exist, places practical restraints in fulfilling both requirements.

Due to the lack of accurate optical characterization methods for accurate bandgap measurements, other techniques are applied with various degrees of success, all placing more prevalent TMDs (MoS$_2$, WSe$_2$, WS$_2$) above or around the 2eV threshold.
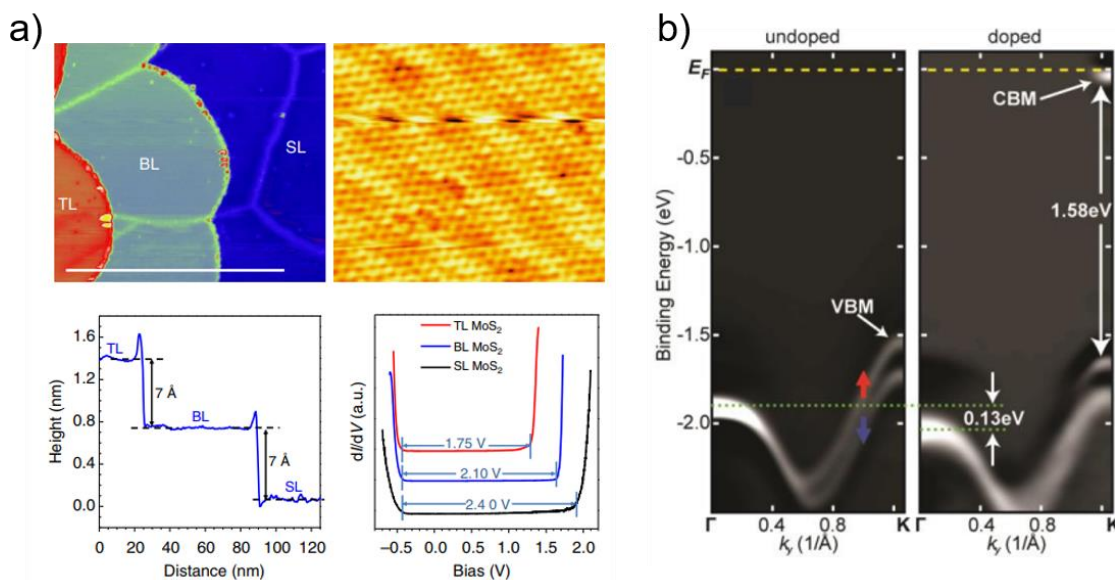
Figure 1.6. *a). STM measurements of a MoS$_2$ sample with three different layer thickness. From top left and rotating clockwise: large-scale STM image of a MoS$_2$ with three different thickness and labeled; High resolution at bilayer MoS$_2$ region; Topological scan of flake with three thickness; dI/dV taken at three thickness regions respectively, with corresponding mapping of the forbidden gap energy range. b). ARPES measurements of*

a MoSe$_2$ before and after doping in order to extract the energy distance between conduction and valence band edge.

Other limitations exist for each of the above example however. Angled-resolved photoelectron spectroscopy (ARPES) can only observe band structure below the fermi level for example, and therefore requires degenerate electron doping in order to observe the entire band structure.[18] This however will change the bandgap due to high doping effects. Scanning tunneling microscopy (STM) has also been used to measure bandgap.[19] However, the application of a drift field to extract charged carriers for density of state mapping relies on one important assumption – free and charged carriers in the semiconductor responsive to an external electric field. Given the neutral charge of excitons and the various different ways they can respond to an external field (disassociate into free carriers, completely ignore, or even respond after trion formation), the extracted "bandgap" does account for the complexity of such multi- quasi-particle systems. Finally, there have also been many attempts at directly predicting the real band gap via density functional theory simulation. This approach has its own shortcoming where by using different potential approximations, bandgap prediction can change by as much as ~0.5eV, as seen by Figure 1.4 c).

1.3 TMD Material Engineering

After establishing a basic knowledge of the material system, we delve deeper into the recent TMD material engineering works. Matured silicon (or more recently silicon germanium) processing techniques such as doping, strain, and contact engineering have all been extensively studied and applied in recent technology nodes to reach higher device performance. A similar tool box is therefore required for the 2D material family in order to fully exploit the system towards high performance devices.

1.3.1. TMD Doping

Fig. 1.7 highlights the four major approaches taken towards TMD doping, including surface charge transfer[20], covalent functionalization[21], fixed charge layer deposition for remote charge doping[22], and substitutional doping[23]. Each approach presents its own pros/cons for a given TMD in terms of maximum doping concentration, reliability, stability and ease of processing. Table 1.1 collates the quantitative results for the various doping schemes presented in literature.
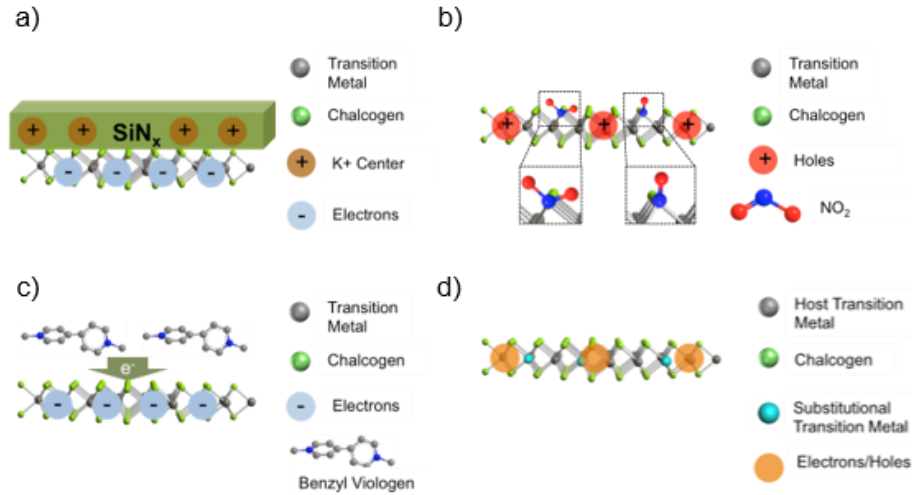
Figure 1.7. *Various TMD doping schemes using specific examples. a) SiN$_x$ as the fixed charge layer. b) Functionalization using NO$_2$ c) Molecular physisorption of benzyl viologen d) Transition metal substitutional doping*

Dopant Species	Polarity on TMD	Max Sheet Concentration (cm^{-2})	Contact Resistance (kΩ*μm)	Ambient Stability
Surface Charge Transfer				
NO$_2$ [23]	WSe$_2$ (p)	2.2 x 10^{12}	NA	NA
K [24]	WSe$_2$ (n) MoS$_2$ (n)	MoS$_2$: 2.5 x 10^{12} WSe$_2$: 1.0 x 10^{13}	NA	NA
Benzyl Viologen [16]	MoS$_2$ (n)	1.2 x 10^{13}	1.1	≥ 9 days
AuCl$_3$ [29, 34]	MoS$_2$ (p)	3 x 10^{13}	NA	NA
Chloride [30]	WS$_2$ (n) MoS$_2$ (n)	MoS$_2$: 9.2 x 10^{12} WS$_2$: 6.0 x 10^{11}	MoS$_2$: 0.3 WS$_2$: 0.4	≥ 4 weeks
Cs$_2$CO$_3$ (n) MoO$_3$ (p) [33]	BP (n) BP (p)	1.5 x 10^{12} (n) 6 x 10^{12} (p) V$_{BG}$ = +/-30V	5.1 x 10^{-3} (n) 2.6 x 10^{-2} (p)	NA
TiO$_x$ [32]	MoS$_2$ (n)	7.4 x 10^{12}	NA	Stable
Covalent Functionalization				
NO$_x$ [15]	WSe$_2$ (p)	1.3 x 10^{13}	2.54	≥ 2 days
Octadecyltrich-lorosilane [31]	WSe$_2$ (p)	5.2 x 10^{11}	NA	≥ 3 days
Substitutional Doping				
Nb [17]	MoS$_2$ (p)	2.8 x 10^{14}	NA	≥ 1 week
Remote Charge Doping				
SiN$_x$ [14]	WSe$_2$ (n)	9.5 x 10^{13}	NA	≥ 2 weeks

Table 1.1 *Summary of major doping schemes reported in literature. The doping methods are classified overall as surface charge transfer, covalent functionalization, substitutional doping, and remote charge doping.*[20-31]

1.3.2. Contact Engineering

Fig. 1.8(a) underlines the challenge associated with obtaining ohmic contacts to TMDs, specifically due to Fermi level pinning at the metal/contact interface[32]. The use of ultra-high (ultra-low) work function metal contacts together with heavy doping is needed for low contact resistance for holes (electrons). In this regard, exploring non-elemental metals with extreme work functions is advantageous. One example is MoO_x ($x < 3$)[33], a high work function (Φ) material (Φ up to 6.6eV) used to contact the valence band of MoS_2. p-type conduction achieved using MoO_x is comparable to the n-type characteristics obtained with Pd contacts as seen in Fig. 1.8(b-c).
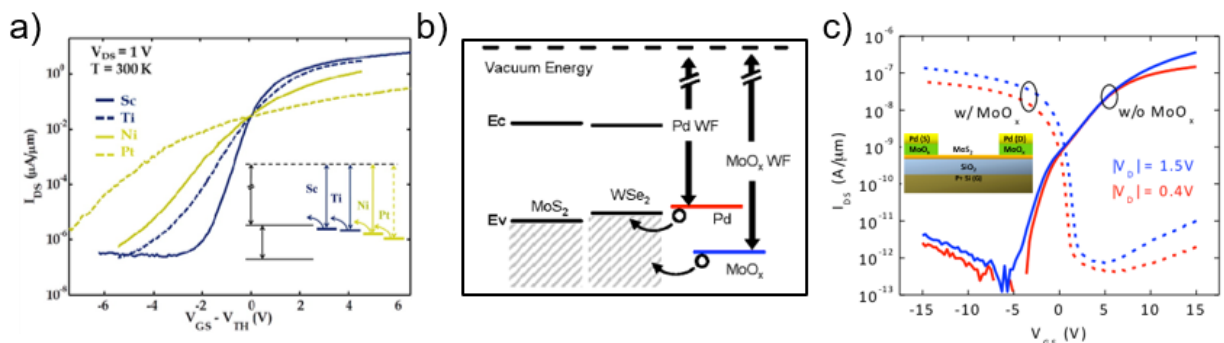
Figure 1.8 *TMD Contact Engineering. a) Fermi level pinning at the MoS$_2$ Schottky barrier. b) Using MoO$_x$ as a high work function metal oxide p-type contact. c) I$_D$V$_G$ of MoS$_2$ FETs with Pd (n-FET) and MoO$_x$/Pd (p-FET) S/D contacts.*

1.3.3. Strain Engineering

Strain can be used to engineer the electronic band structure and optoelectronic properties of TMD materials[34, 35]. An interesting case is that of WSe$_2$ multilayers, which undergo an indirect to direct bandgap transition under uniaxial tensile strain[34], similar to Ge as shown in Fig. 1.9(a-c). This enables application of multilayer TMDs in optoelectronic device applications like photodiodes, solar cells, LEDs, etc. Also a change in bandstructure would lead to a change in the carrier mobility, enabling mobility engineering via strain[36].
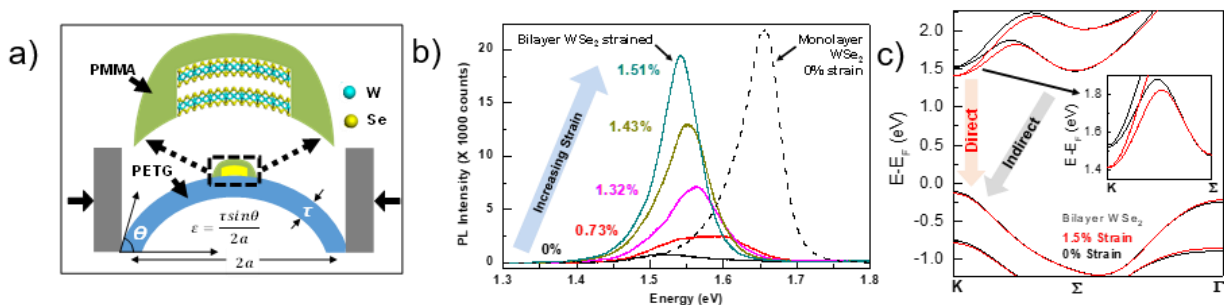
Figure 1.9. *a) Schematic of the 2-point bending apparatus for uniaxial tensile strain. WSe$_2$ encapsulated by PMMA is transferred onto PETG. τ is the thickness of the PETG, ε is the*

strain, θ is the tangent angle at the min. strain point and 2a is the separation of the bent PETG. b) Bilayer WSe₂ photoluminescence (PL) spectra at different strain. PL of unstrained monolayer WSe₂ is shown for comparison. c) Electronic band structure for bilayer WSe₂ with and without strain using HSE-DFT.

1.4 TMD Electronic Devices

This section will address some of the overall advances made in relation to various configurations of TMD field effect transistors (FET). In particular, demonstration of traditional metal oxide semiconductor FETs with 60mV/dec room temperature swing with ~250 cm²/Vs effective hole mobility (without any material passivation) is significant in displaying the intrinsic potential TMDs hold for future device applications. Other advanced structures (including all 2D FETs and tunneling FETs) are also realized, underlying the practical roles such TMD materials can provide in more advanced nanoelectronics.

1.4.1. Metal Oxide Semiconductor Field Effect Transistors

Fig. 1.10(a) shows a top-gated WSe₂ MOSFET fabricated with doped source/drain (S/D) extensions which decreases the series contact resistance and enable exploration of the intrinsic material performance. Fig. 1.10(b-c) show the transfer characteristics of WSe₂ MOSFETs incorporating S/D extension doping using surface charge transfer from NO₂ and K, achieving high performance WSe₂ p-FETs (subthreshold swing ~ 60mV/dec and hole mobility ~250 cm²/Vs)[24] and n-FETs (electron mobility ~110 cm²/Vs)[25] respectively. Moreover, using the aforementioned techniques, WSe₂ p-FET (using Pt contacts) and n-FET (using S/D extension K doping) are fabricated on the same flake as shown in Fig. 1.10(d)[37], forming a WSe₂ CMOS inverter with output and voltage transfer curves shown in Fig. 1.10(e-f) respectively.
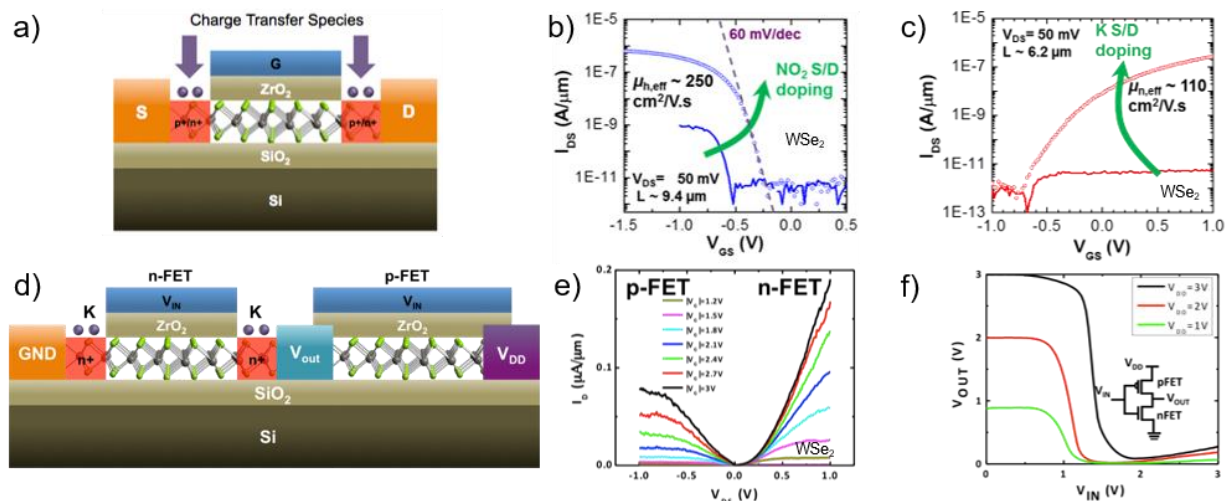
Fig 1.10. *a) General schematic of a top-gated TMD MOSFET with degenerately doped source/drain (S/D) contacts. Here the top-gate acts as the mask to protect the active channel from dopant species. b) Transfer characteristics of a monolayer WSe₂ device*

with L ~9.4μm before and after NO$_2$ S/D contact doping[24] c) Transfer characteristics of a 3 layer WSe$_2$ MOSFET before and after K contact doping[25] d) Schematic of a WSe$_2$ CMOS inverter. e) Output characteristics of a WSe$_2$ p-FET and n-FET fabricated on the same WSe$_2$ flake. f) Voltage transfer characteristics of a WSe$_2$ CMOS inverter at different supply voltages[37].

1.4.2. All 2D Field Effect Transistors

Fig. 1.11 shows the schematic and device characteristics of an all-2D FET, a new device platform using MoS$_2$ as channel, graphene as source, drain and gate electrodes and h-BN as the gate dielectric[38]. This device operates as an n-FET with $I_{ON}/I_{OFF} \sim 10^6$. The mobility of MoS$_2$ is extracted to be ~33 cm^2/Vs after correcting for the contact resistance. Notably, the mobility of the channel does not degrade at high gate electric fields, suggesting the absence of surface roughness scattering. This experimental observation demonstrates a key advantage of layered materials like TMDs over conventional semiconductors especially as scaling progresses towards ultrathin body devices.
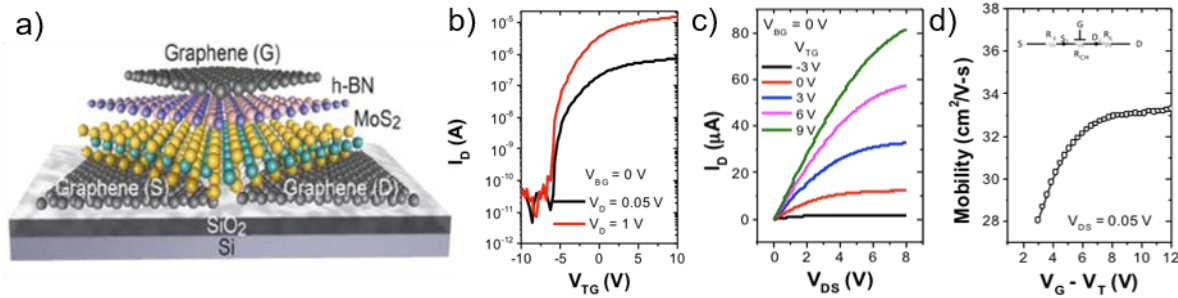
Fig. 1.11. *a) Device schematic of an all 2D FET realized using heterogeneous integration of two-dimensional materials for all of the components, including the channel, gate dielectric and contact layers[38] b) I$_D$V$_G$ characteristics at different V$_D$ (c) I$_D$V$_D$ characteristics. (d) Extracted field effective mobility as a function of gate overdrive, V$_G$-V$_T$. The inset shows the circuit model of the device used for mobility extraction. Note that mobility does not degrade as a function of surface scattering at large gate overdrive voltages. The Si substrate is grounded during all measurements.*

1.4.3. 2D Heterostructures

Atomically smooth heterostructures with strain free interfaces and sharp band edges are made possible because of the unique properties of layered materials like TMDs.[39] Fig. 1.12(b) shows the transmission electron microscope (TEM) image of a WSe$_2$/MoS$_2$ hetero-bilayer. Due to vdW interlayer bonding, the heterostructure exhibits no structural stress and displays a pristine Moiré pattern arising from the difference in lattice constant and angular orientation. Photoluminescence and absorption measurements as shown in Fig. 1.12(c) indicate a spatially direct absorption but spatially

indirect emission mechanism which is explained in Fig. 1.12(d). The strong intensity of the spatially indirect emission indicates significant charge coupling across the vdW gap of these heterostructures.
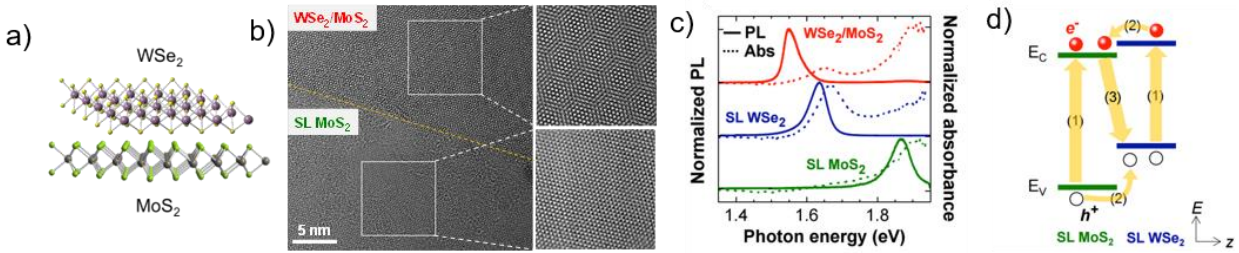
Figure 1.12. *a) Schematic of a WSe₂/MoS₂ hetero-bilayer.[40] b) Transmission emission microscopy (TEM) of a WSe₂/MoS₂ hetero-bilayer, note that a clear Moiré pattern is seen at the hetero-bilayer. c) Normalized photoluminescence (solid lines) and absorbance (dashed lines) spectra of single-layer WSe₂, MoS₂, and the corresponding heterostructure. d) Band diagram of WSe₂/MoS₂ heterostructure under photo excitation, depicting (1) absorption and exciton generation in WSe₂ and MoS₂ single layers, (2) relaxation of excitons at the MoS₂/WSe₂ interface driven by the band offset, and (3) radiative recombination of spatially indirect excitons.*

1.4.4 TMD Tunnel FETs

TMD heterostructures can be configured as tunnel FETs, taking advantage of the theoretically sharp band edges of these layered semiconductors.[40] Fig. 1.13 shows the operation of a four-terminal gate-tunable WSe₂/MoS₂ vdW heterojunction diode.[39] In this dual-gated structure, the bottom and top gates can exert independent electrostatic control over the MoS₂ and WSe₂ layers respectively. In this configuration, the two gates can modulate the band offset and the doping concentrations of WSe₂ and MoS₂ layers thereby tuning the operation of the diode. As the band offset is increased, the diode performance is tuned from a p/n diode to a Zener diode and at the p+/n+ condition to an Esaki diode as shown in Fig. 1.13(c) and (d).
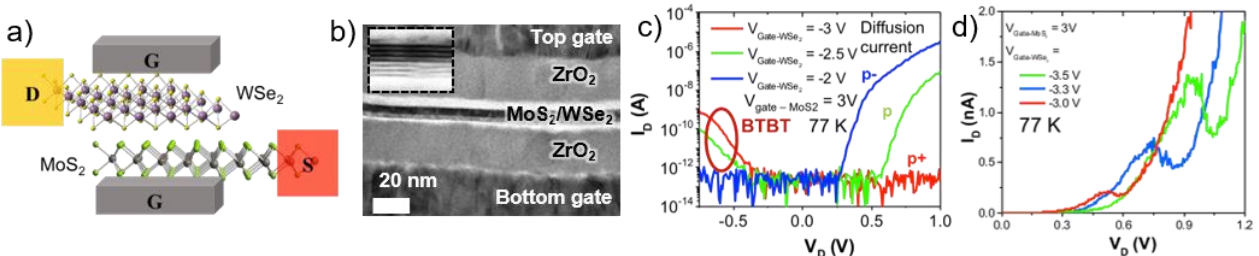
Fig 1.13. *Tunnel-FETs based on vdW heterostructures.[39] a) Schematic of a dual-gated TFET, note that the top and bottom gates are able to electrostatically control the band alignment of the top and bottom TMD layers respectively, allowing for effective band offset modulation at the hetero-interface. b) TEM cross sectional image of a fabricated device, note that MoS₂ and WSe₂ are 4 layers each in thickness for this device. c) Gate tunability*

of a dual-gated MoS$_2$/WSe$_2$ device at 77 K. d) I$_D$V$_D$ at V$_{Gate-MoS2}$ = 3 V and V$_{Gate-WSe2}$ varied. Negative differential resistance is observed at forward bias.

Moving forward, investigation of material systems with appropriate band alignments and carrier effective mass values, interface engineering, and doping contacts to reduce parasitic resistances are required to achieve high performance TFETs based on heterostructure TMDs.

1.5 Thesis Organization

This chapter is meant to set a motivation for the rest of the thesis along with a rundown of relevant introductory knowledge available at the time of writing. In chapter 2, an in-depth look of surface defects, and how we can engineer such defects to our advantage in relation to device applications will be investigated. In chapter 3, we will focus on using optical characterization to probe edge defects. Specifically, we will derive the relationship between generated diffusing excitons and edge recombination, realizing a metric directly related to the TMD edge quality called edge recombination velocity (ERV). In chapter 4, we will discuss the impact various semiconducting processing has on ERV, specifically in relation to critically choosing the proper etching methods for edge passivation. We will introduce scanning probe lithography as an alternative TMD edge patterning method where extracted TMD varies widely by the material probed, highlighting the lessened impact process-induced defects has on the created edge defects.

Finally, the report will conclude with a summary of contributions made in understanding and engineering various TMD defects, along with suggestions and possible research directions moving forward addressing key remaining challenges as TMD becomes one step closer to the ideal candidates for next generation solid state semiconducting materials that we envision them to be.

REFERENCE

1.   Moore, G. E. *Proc. IEEE* **1998,** 86, (1), 82-85.
2.   *International Technology Roadmap* **2015**

3.   Xie, R.; Montanini, P.; Akarvardar, K.; Tripathi, N.; Haran, B.; Johnson, S.; Hook, T.; Hamieh, B.; Corliss, D.; Wang, J.; Miao, X.; Sporre, J.; Fronheiser, J.; Loubet, N.; Sung, M.; Sieg, S.; Mochizuki, S.; Prindle, C.; Seo, S.; Greene, A.; Shearer, J.; Labonte, A.; Fan, S.; Liebmann, L.; Chao, R.; Arceo, A.; Chung, K.; Cheon, K.; Adusumilli, P.; Amanapu, H. P.; Bi, Z.; Cha, J.; Chen, H. C.; Conti, R.; Galatage, R.; Gluschenkov, O.; Kamineni, V.; Kim, K.; Lee, C.; Lie, F.; Liu, Z.; Mehta, S.; Miller, E.; Niimi, H.; Niu, C.; Park, C.; Park, D.; Raymond, M.; Sahu, B.; Sankarapandian, M.; Siddiqui, S.; Southwick, R.; Sun, L.; Surisetty, C.; Tsai, S.; Whang, S.; Xu, P.; Xu, Y.; Yeh, C.; Zeitzoff, P.; Zhang, J.; Li, J.; Demarest, J.; Arnold, J.; Canaperi, D.; Dunn, D.; Felix, N.; Gupta, D.; Jagannathan, H.; Kanakasabapathy, S.; Kleemeier, W.; Labelle, C.; Mottura, M.; Oldiges, P.; Skordas, S.; Standaert, T.; Yamashita, T.; Colburn, M.; Na, M.; Paruchuri, V.; Lian, S.; Divakaruni, R.; Gow, T.; Lee, S.; Knorr, A.; Bu, H.; Khare, M. In *A 7nm FinFET technology featuring EUV patterning and dual strained high mobility channels*, 2016 IEEE International Electron Devices Meeting (IEDM), 3-7 Dec. 2016, 2016; pp 2.7.1-2.7.4.

4.   Ohtou, T.; Sugii, N.; Hiramoto, T. *IEEE Electron Device Letters* **2007,** 28, (8), 740-742.

5.   Shin, C.; Sun, X.; Liu, T. J. K. *IEEE Trans. Electron Devices* **2009,** 56, (7), 1538-1542.

6.   Diebold, A. C. *Physics Challenges Facing the Semiconductor Industry Based on the ITRS*; American Physical Society Physics: 2004.

7.   Technology Quarterly: After Moore's Law. *Economist* 2016.

8.   Jones, H. *Design Automation Conference* **2018**.

9.   Knickerbocker, J. U.; Andry, P. S.; Dang, B.; Horton, R. R.; Patel, C. S.; Polastre, R. J.; Sakuma, K.; Sprogis, E. S.; Tsang, C. K.; Webb, B. C.; Wright, S. L. In *3D silicon integration*, 2008 58th Electronic Components and Technology Conference, 27-30 May 2008, 2008; pp 538-543.

10.   Morgan, J., IBM unveils computer fed by 'electronic blood'. *BBC News Zurich* 2013.

11.   Tonti, D. Photoelectron Spectroscopy Study of the Intercalation Reaction of Alkali Metals in Transition Metal Dichalcogenides. Dissertation, Free University of Berlin, 2000.

12.   Wang, Q. H.; Kalantar-Zadeh, K.; Kis, A.; Coleman, J. N.; Strano, M. S. *Nature Nanotechnology* **2012,** 7, 699.

13.   Zhao, P.; Desai, S.; Tosun, M.; Roy, T.; Fang, H.; Sachid, A.; Amani, M.; Hu, C.; Javey, A. In *2D layered materials: From materials properties to device applications*, 2015 IEEE International Electron Devices Meeting (IEDM), 7-9 Dec. 2015, 2015; pp 27.3.1-27.3.4.

14.   Molina-Sánchez, A.; Sangalli, D.; Hummer, K.; Marini, A.; Wirtz, L. *Phys. Rev. B* **2013,** 88, (4), 045412.

15.   Splendiani, A.; Sun, L.; Zhang, Y.; Li, T.; Kim, J.; Chim, C.-Y.; Galli, G.; Wang, F. *Nano Lett.* **2010,** 10, (4), 1271-1275.

16.   Mouri, S.; Miyauchi, Y.; Matsuda, K. *Nano Lett.* **2013,** 13, (12), 5944-5948.

17.   Amani, M.; Taheri, P.; Addou, R.; Ahn, G. H.; Kiriya, D.; Lien, D.-H.; Ager, J. W.; Wallace, R. M.; Javey, A. *Nano Lett.* **2016,** 16, (4), 2786-2791.

18.   Zhang, Y.; Chang, T.-R.; Zhou, B.; Cui, Y.-T.; Yan, H.; Liu, Z.; Schmitt, F.; Lee, J.; Moore, R.; Chen, Y.; Lin, H.; Jeng, H.-T.; Mo, S.-K.; Hussain, Z.; Bansil, A.; Shen, Z.-X. *Nature Nanotechnology* **2013,** 9, 111.

19.   Huang, Y. L.; Chen, Y.; Zhang, W.; Quek, S. Y.; Chen, C.-H.; Li, L.-J.; Hsu, W.-T.; Chang, W.-H.; Zheng, Y. J.; Chen, W.; Wee, A. T. S. *Nat. Commun.* **2015,** 6, 6298.

20.   Kiriya, D.; Tosun, M.; Zhao, P.; Kang, J. S.; Javey, A. *J. Am. Chem. Soc.* **2014,** 136, (22), 7853-7856.

21.   Zhao, P.; Kiriya, D.; Azcatl, A.; Zhang, C.; Tosun, M.; Liu, Y.-S.; Hettick, M.; Kang, J. S.; McDonnell, S.; Kc, S.; Guo, J.; Cho, K.; Wallace, R. M.; Javey, A. *ACS Nano* **2014,** 8, (10), 10808-10814.

22.   Chen, K.; Kiriya, D.; Hettick, M.; Tosun, M.; Ha, T.-J.; Madhvapathy, S. R.; Desai, S.; Sachid, A.; Javey, A. *APL Materials* **2014,** 2, (9), 092504.

23.   Suh, J.; Park, T.-E.; Lin, D.-Y.; Fu, D.; Park, J.; Jung, H. J.; Chen, Y.; Ko, C.; Jang, C.; Sun, Y.; Sinclair, R.; Chang, J.; Tongay, S.; Wu, J. *Nano Lett.* **2014,** 14, (12), 6976-6982.

24.   Fang, H.; Chuang, S.; Chang, T. C.; Takei, K.; Takahashi, T.; Javey, A. *Nano Lett.* **2012,** 12, (7), 3788-3792.

25.   Fang, H.; Tosun, M.; Seol, G.; Chang, T. C.; Takei, K.; Guo, J.; Javey, A. *Nano Lett.* **2013,** 13, (5), 1991-1995.

26.   Choi, M. S.; Qu, D.; Lee, D.; Liu, X.; Watanabe, K.; Taniguchi, T.; Yoo, W. J. *ACS Nano* **2014,** 8, (9), 9332-9340.

27.   Yang, L.; Majumdar, K.; Liu, H.; Du, Y.; Wu, H.; Hatzistergos, M.; Hung, P. Y.; Tieckelmann, R.; Tsai, W.; Hobbs, C.; Ye, P. D. *Nano Lett.* **2014,** 14, (11), 6275-6280.

28.   Kang, D.-H.; Shim, J.; Jang, S. K.; Jeon, J.; Jeon, M. H.; Yeom, G. Y.; Jung, W.-S.; Jang, Y. H.; Lee, S.; Park, J.-H. *ACS Nano* **2015,** 9, (2), 1099-1107.

29.   Rai, A.; Valsaraj, A.; Movva, H. C. P.; Roy, A.; Ghosh, R.; Sonde, S.; Kang, S.; Chang, J.; Trivedi, T.; Dey, R.; Guchhait, S.; Larentis, S.; Register, L. F.; Tutuc, E.; Banerjee, S. K. *Nano Lett.* **2015,** 15, (7), 4329-4336.

30.   Xiang, D.; Han, C.; Wu, J.; Zhong, S.; Liu, Y.; Lin, J.; Zhang, X.-A.; Ping Hu, W.; Özyilmaz, B.; Neto, A. H. C.; Wee, A. T. S.; Chen, W. *Nat. Commun.* **2015,** 6, 6485.

31.   Kiriya, D.; Zhou, Y.; Nelson, C.; Hettick, M.; Madhvapathy, S. R.; Chen, K.; Zhao, P.; Tosun, M.; Minor, A. M.; Chrzan, D. C.; Javey, A. *Adv. Funct. Mater.* **2015,** 25, (39), 6257-6264.

32.   Das, S.; Chen, H.-Y.; Penumatcha, A. V.; Appenzeller, J. *Nano Lett.* **2013,** 13, (1), 100-105.

33.   Chuang, S.; Battaglia, C.; Azcatl, A.; McDonnell, S.; Kang, J. S.; Yin, X.; Tosun, M.; Kapadia, R.; Fang, H.; Wallace, R. M.; Javey, A. *Nano Lett.* **2014,** 14, (3), 1337-1342.

34.   Desai, S. B.; Seol, G.; Kang, J. S.; Fang, H.; Battaglia, C.; Kapadia, R.; Ager, J. W.; Guo, J.; Javey, A. *Nano Lett.* **2014,** 14, (8), 4592-4597.
35.   Conley, H. J.; Wang, B.; Ziegler, J. I.; Haglund, R. F.; Pantelides, S. T.; Bolotin, K. I. *Nano Lett.* **2013,** 13, (8), 3626-3630.
36.   Welser, J.; Hoyt, J. L.; Takagi, S.; Gibbons, J. F. In *Strain dependence of the performance enhancement in strained-Si n-MOSFETs*, Proceedings of 1994 IEEE International Electron Devices Meeting, 11-14 Dec. 1994, 1994; pp 373-376.
37.   Tosun, M.; Chuang, S.; Fang, H.; Sachid, A. B.; Hettick, M.; Lin, Y.; Zeng, Y.; Javey, A. *ACS Nano* **2014,** 8, (5), 4948-4953.
38.   Roy, T.; Tosun, M.; Kang, J. S.; Sachid, A. B.; Desai, S. B.; Hettick, M.; Hu, C. C.; Javey, A. *ACS Nano* **2014,** 8, (6), 6259-6264.
39.   Roy, T.; Tosun, M.; Cao, X.; Fang, H.; Lien, D.-H.; Zhao, P.; Chen, Y.-Z.; Chueh, Y.-L.; Guo, J.; Javey, A. *ACS Nano* **2015,** 9, (2), 2071-2079.
40.   Fang, H.; Bechtel, H. A.; Plis, E.; Martin, M. C.; Krishna, S.; Yablonovitch, E.; Javey, A. *Proceedings of the National Academy of Sciences* **2013,** 110, (29), 11688.

Chapter 2: Surface Covalent Functionalization

2.1 Surface Defects

Ideally, TMDs possess pristine surface with no defects and inter-layer van-der Waals (vdW) interactions. However, we live in an ideally imperfect world. Currently, TMDs always suffer from a variety of surface defects dependent on the synthesis/deposition methods. For few layer TMD research, two general deposition approaches exist, with the most frequently used technique as: tape exfoliation[1] (top down) and chemical vapor deposition[2] (bottom up). All of the flakes used in this work are tape exfoliated unless otherwise stated. Tape exfoliation involves first growing (or directly purchasing) as-grown bulk TMD crystals in a closed vapor transport setup (with a usual transport gas of chlorine or iodine). Researchers then proceed to utilize commercially available scotch tapes (or tapes of varying adhesive force) to mechanically exfoliate the bulk crystal on a substrate of choice, separating out individual layers.

The most common substrate used for exfoliation is thermal silicon oxide grown on silicon owning to the ease of subsequent electrical characterizations. Additionally, certain thickness of silicon oxide is known to improve contrast of the TMD monolayer and render them optically visible due to interferences.[3]

In most cases involving surface defect discussions, the heavily investigated interface is that of air and TMD. Additionally, this top surface directly affects the TMD/substrate interface as well, especially in the few (or mono-) layer limit. Therefore, discussion of surface defects in this section will focus on the top facing air/TMD interface. So far, extensive STM/AFM characterizations have been done showing vacancy or vacancy clusters present on freshly cleaved surfaces.[4-7] Subsequent density of state conduction and XPS measurements suggest mostly chalcogen vacancies.[8, 9] Various works have also attributed these vacancies as the cause for n or p-type behavior seen from field effect transistor measurements, characterizing for example sulfur vacancies as electric donors in MoS_2.[4] At the extreme, cases of MoS_2 nanoribbon (NR) has been experimentally fabricated with constant He^+ bombardment as a method of shrinking the NR width.[10] At the single nanometer width limit, the authors observed metallic behavior and attributed this to an overabundance of chalcogen vacancies while the left-over metals reassemble locally to form metallic conduction path. This study further underlines the effects of defects on the electrical transport of TMDs, underlining the necessity of effective passivation methods.

2.1.1. Surface Defect Passivation

For both interfaces, various work exists in passivation attempts. It is obvious that the air-TMD interface is much easier to passivate, and many different approach have been used towards this aim. Works utilizing thiols, solution-based chemistry, and gas-based chemistry have all demonstrated varied degrees of passivation.[11-14] Subsequently, various characterization methods have been used to validate the passivation results. Out of the methods used, PL internal quantum yield (iQY) and surface topology

characterization provide some of the most sensitive and direct results. This is because the former describes an efficiency that is directly related to the minority carrier concentration of the system, while the latter presents direct experimental evidence of the species present on the TMD monolayer.

A clear example of wet chemistry passivation with PL iQY characterization demonstrated a 6-order pump regime mapping of a monolayer MoS_2 PL iQY, claiming a >95% iQY after solution-based chemistry passivation of the surface recombination sites.[12] This work shows both the potential of near complete surface defect passivation of sulfide TMDs (with monolayer at the direct bandgap regime to allow for this form of characterization) that prevents nonradiative recombination of traps at the lower pump regime. However, further studies revealed that the solution does not have the same impact on selenides owning to differences in chemistry.[5]

Other reported surface passivation examples also use wet chemistry on MoS_2 and are validated using direct STM characterizations via thiol treatment. The sample is then imaged with STM to directly observe changes in the local electronic distribution. This work clearly shows thiols occupying sulfur vacancies on the MoS_2 surface.[11] Interestingly however, subsequent optical characterization of thiol functionalized MoS_2 did not demonstrate PL improvement. In fact, many have shown lower overall PL emission.[15] More studies are needed to elucidate the complex dynamics of TMD systems due to the existence of trions and multi-quasi-particle interactions.

While advancements on surface defect identification and passivation are made on distinct members of the TMD family (MoS_2 and WS_2 PL iQY > 95%), more is needed for further understanding and eventual complete passivation of surface defects across all TMD members, sulfides and selenides alike.

2.2 NO_2 Doping on WSe_2 And Predicted Configurations
It is now clear that surface defects exist on TMDs. While a large effort exists for passivation, understanding of the intrinsic natures of defects is also vital. A parallel effort in defect engineering becomes a clear alternative while passivation efforts progresses – if we cannot passivate all known defects in the near future, we can at least leverage the existing defect sites into practical uses. In the following, WSe_2 is chosen as a material of interest while we investigate surface defect engineering towards electronics applications.

The most prevalent TMD used towards electronic devices study is MoS_2.[16] A corresponding p-type TMD is therefore necessary to consolidate any practical platform towards future complementary FET devices. WSe_2, a p-type TMD whose few layer characteristics already demonstrate near perfect room temperature subthreshold swing and high dynamic switching range is a great starting point for further defect engineering.[17] Unfortunately, the contact doping required to observe the intrinsic WSe_2 channel advantages were unstable as NO_2 gas molecules physiosorbed on the TMD surface. Therefore, we moved towards exploring a permanent contact doping scheme of WSe_2 based FETs in order to realize better performance p-type TMD FETs.[18]

2.2.1 Fabrication and NOₓ Covalent Functionalization

A back-gated WSe_2 FET is fabricated *via* standard electron beam lithography or photolithography and exposed to NO_2 at 150°C for a set reaction time of 4-12 hours. Given the strong oxidizing nature of NO_2, we predict an induced NO_x chemisorption process on WSe_2 due to the temperature and treatment time utilized. A defect-oriented model is proposed where NO_2 chemisorbs on WSe_2 surface and bulk defect sites (*e.g.*, selenium vacancies), forming stable electron withdrawing $WSe_{2-x-y}O_xN_y$ species that lead to *p*-doping (Figure 2.1(a-b)). At the temperatures used here, NO_2 gas is partly decomposed to form O and NO,[19, 20] making various covalent functionalization schemes possible. Figure 2.1(b) depicts three most likely scenarios. Figure 2.1(b)-i shows direct W oxidation resulting from the O of NO_2 occupying a Se vacancy followed by NO_2 thermal disassociation and desorption of NO. Figure 2.1(b)-ii shows the alternative NO_2 adsorption configuration with N directly bonding to W at the presence of a Se vacancy. Figure 2.1(b)-iii illustrates N of NO covalently bonded with W, where NO is created through NO_2 disassociation.
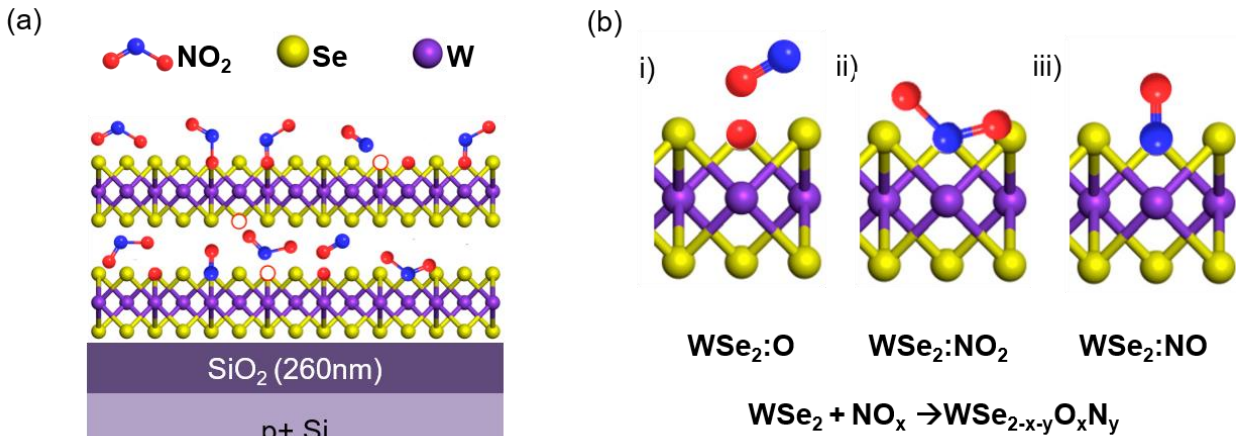
Figure 2.1. (a) Schematic of NO_x chemisorption process at the WSe_2 bulk and surface (b) Proposed specific NO_x chemisorption at the selenium vacancy sites can lead to three distinct configurations: i) WSe_2:O ii) WSe_2:NO_2 iii) WSe_2:NO

Transfer characteristics of doped devices are measured before and after NO_x functionalization (Figure 2.2). Here the thickness of WSe_2 flake is ~ 5 nm. Before NO_2 exposure, we observe a clear *p*-FET characteristic with an on/off ratio of ~1000 and a low I_{on} of ~10^{-8} A/μm due to severe contact resistance resulting from the Schottky barrier present between WSe_2 and Pd.[17] After NO_x chemisorption, we observe a drastic increase of I_{on} by about 1000x, and gate's inability to control the channel conduction. Gate control loss is due to hole doping by NO_x chemisorption that moves the Fermi level (E_F) to close proximity of the valence band edge (E_V). The excessive states present in the vicinity of E_F then render gate modulation of E_F ineffective, reflecting a degenerate *p*-doping situation. The doping stability is studied by examining the changing transfer characteristics of the doped sample upon air exposure. As seen in Figures 2.2(b), the device undergoes a gradual current drop for the first 2-3 hours, and eventually stabilizing at a set current level. This initial current drop is attributed to desorption of physisorbed NO_x species leaving the WSe_2. As expected, our doping mechanism is a combination of

NO$_x$ physi- and chemisorption on WSe$_2$ where *only* chemisorbed NO$_x$ contributes to stable doping. The falling current *versus* time is fit to Langmuir isotherm assuming current being directly related to the physisorbed NO$_x$ coverage *via* $I(t) = I_{initial} + \frac{\psi}{1+\psi}(1 - e^{-\frac{t}{\tau}})$ where *t* is the air exposure time, *I$_{initial}$* is the initial current level right after chemisorption, ψ is a dimensionless parameter characterizing surface coverage, and τ is the desorption time constant. We extract the desorption time constant $\tau \sim 40$ minutes from NO$_x$ physisorption, comparable to other physisorption-based gas sensors (such as ion-sensitive FET sensors) operating at room temperature.[21] Notably, the doping effect is irreversible even after thermal annealing of the sample at 300°C in Ar$_2$, which further supports our proposed scheme of NO$_x$ chemisorption leading to stable doping.
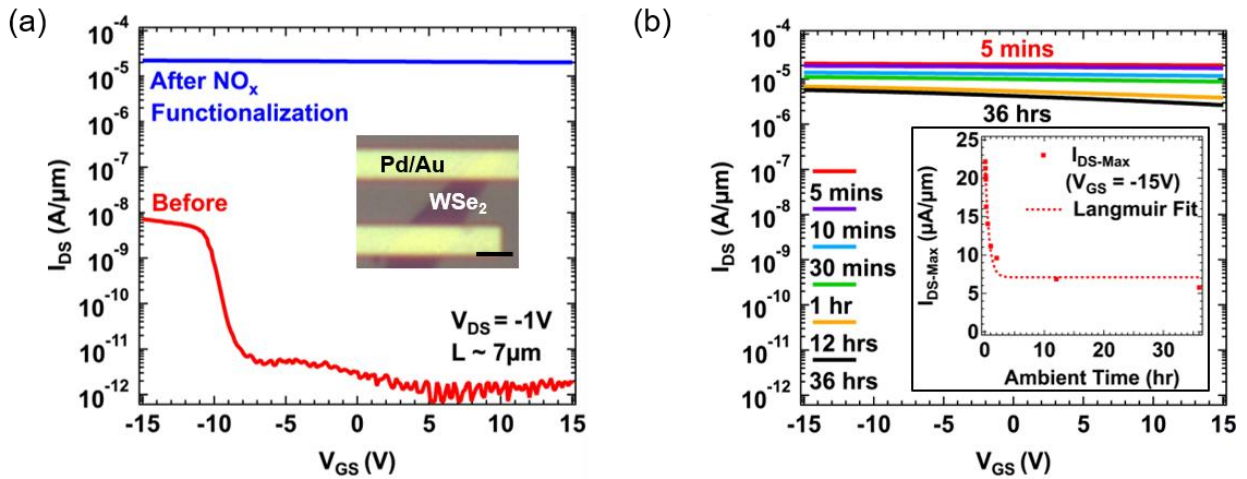
Figure 2.2. *(a) I$_{DS}$-V$_{GS}$ of before and after NO$_2$ treated devices. Inset: Optical microscopy of fabricated device using Pd/Au contacts, scale bar is 2 μm (b) Initial current drop after doping is attributed desorption of weakly physisorbed NO$_2$. Inset: Drain current change is fitted to a time-dependent Langmuir isotherm desorption model vs. air exposure time. Dash line represents fitted curve.*

2.3 X-ray Absorption Spectroscopy (XAS) of NO$_2$ Functionalized WSe$_2$

2.3.1. XAS Theory

The scheme of covalent functionalization allowed us to take advantage of many vacuum-based characterization techniques as the molecular NO$_x$ species are firmly chemisorbed to the TMD surface. One characterization used is XAS, or x-ray absorption spectroscopy. XAS is chosen due to its relatively high atomic sensitivity towards low atomic number species (such as nitrogen in our dopant species). This allows us to conduct reliable analysis in chemical changes of the dopant specie even if the dopant concentration is low (~0.1% atomic percentage).

Shortly, high monochromatic x-ray generated via synchrotron is delivered into the sample, triggering electron and photon emission as the electrons in the molecular orbitals (K-edge is usually selected due to larger absorption cross section) are excited and

relaxed back into their respective ground states. During relaxation, the excess energy can either emit directly (photon) or excite a neighboring electron into the vacuum level, resulting in secondary (Auger) electron emission. This technique is therefore both surface and bulk sensitive, depending on the detector configuration and specie of observation.

For example, electron ejection (also known as total electron yield, or TEY) will usually only occur in the first few nanometers of the sample due to the shorter mean free path and difficulty of electron collection deeper from the surface due to sample charging and other experimental considerations. On the other hand, photon ejection (total fluorescence yield or TFY) is a more bulk sensitive process due to its longer mean free path (~>50nm) in the sample towards emission. Therefore, a comprehensive analysis of the species of interest can be done in both depth regime.[22]

For this experiment, X-ray absorption spectroscopy of NO_x chemisorption in WSe2 characterization was taken at Beamline 8.0.1 at Advanced Light Source, Lawrence Berkeley National Laboratory. N K-edge spectrum was calibrated carefully by measuring h-BN reference sample for energy calibration. The energy resolution at N K-edge region is about 0.1 eV and the vacuum of experiment chamber is lower than 5×10^{-9} Torr.

2.3.2. NO_x Species Present
As mentioned above, surface covalent functionalization enables in-depth material characterization techniques in UHV environments, in contrast with that of the unstable surface physisorbed molecules.[17, 23] The nitrogen K absorption edge is examined here via XAS.

A collection of both total electron yield (penetration depth of ~10 nm) and total fluorescence yield (penetration depth of ~100 nm) show similar emission trend, signifying various nitrogen containing species in both depth regimes. The results suggest that the chemisorption is occurring at both the surface and interface between the layers of WSe_2. As a function of absorbed photon energy for N 1s electrons, a larger energy translates to a higher N oxidation state, as it becomes harder to remove electrons due to stronger electrostatic interactions. We observe 3 peaks at ~396eV, ~401eV, and ~406eV which we assign to N-W (from $W-NO_x$ species), NO, and NO_2 species respectively based on literature values.[24-29] Therefore XAS results substantiate all three predicted configurations shown in section 2.2.
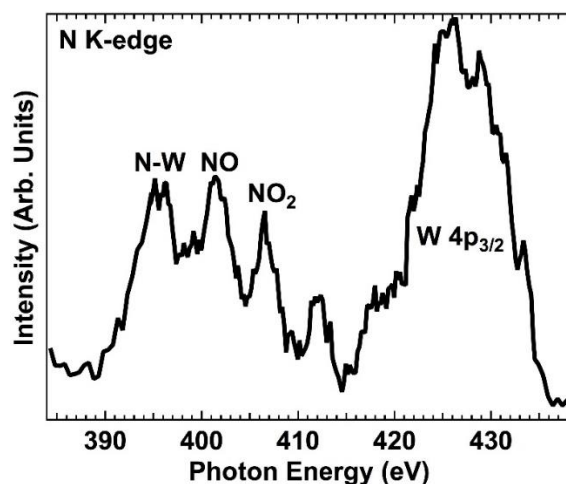
Figure 2.3. *Total electron yield of Soft X-ray Absorption Spectroscopy (XAS) NO_x functionalized samples. Identifiable peaks N K-edge indicates N-W, NO, and NO_2 species in host after NO_x chemisorption.*

2.4 X-ray Photoelectron Spectroscopy (XPS) of NO_x Functionalized WSe_2

2.4.1. XPS Theory

In addition to XAS, x-ray photoelectron spectroscopy (XPS) is used here to analyze the binding energy change after covalent functionalization of the host atomic species such as tungsten and selenium. Similar to XAS, XPS also involves an injection of monochromatic x-ray into the sample material and measuring the energy of the subsequent ejection of electrons. By measuring the kinetic energy of the free electrons, details of the species' chemical make ups (and individual oxidation states of the atoms via binding energy) can be quantitatively inferred by comparing against a calibrated standard of electron kinetic energy for various atoms and differing orbital values.

Additionally, the position of the valence band in relation to the fermi level can also be measuring via XPS. By simply observing the amount of electron ejection vs. energy applied, one can infer the position of the valence band edge via population mapping of the valence band structure.[30]

2.4.2. NO_x Species Present

Core W levels were investigated *via* XPS. According to Figure 2.4 (b), six visible peaks were observed after doping compared to only two visible peaks before NO_x chemisorption. The six peaks correspond to three doublets (each doublet possessing a unique W $4f_{5/2}$ and W $4f_{7/2}$ peak value), each doublet indicating a different W containing species with W of different oxidation states. Doublet III at 35.81 eV is assigned to WO_x with at an almost 6^+ oxidation state.[31, 32] Doublets I and II (31.8 and 32.5 eV for W $4f_{7/2}$ values respectively) are assigned to different stoichiometric ratio of $WSe_{2-x-y}O_xN_y$ species (also observable at the Se 3d level in Figure 2.4 (b) and corresponds to W oxidation state between 0 and 4^+ (ref. [33]). Note that the N stoichiometric ratio y is less than 0.003, corresponding to an atomic concentration of 0.1% and falling below the XPS detection limit. XAS, with a higher sensitivity due to Synchrotron excitation source however, clearly

identifies the N present and underlines the importance of using both XAS and XPS to probe the complete composition of the chemisorbed species present on WSe2.

The valence band edge of WSe2 was also examined by XPS. We observe a 0.8eV shift of E_F (Figure 2.4(c)) upon NO_x chemisorption with E_V-E_F ~50 meV extracted *via* linear extrapolation of the valence band tail. This large E_F shift is indicative of *p*-doping of WSe2 and suggests a degenerate doping level (E_V-E_F < 3kT) by NO_x functionalization. From E_V-E_F, we extract a hole concentration of p ~ 1.3×10^{19}cm^{-3} by using the Joyce Dixon approximation[34] using an effective density of states[35] of N_v at 2.54×10^{19}cm^{-3}.
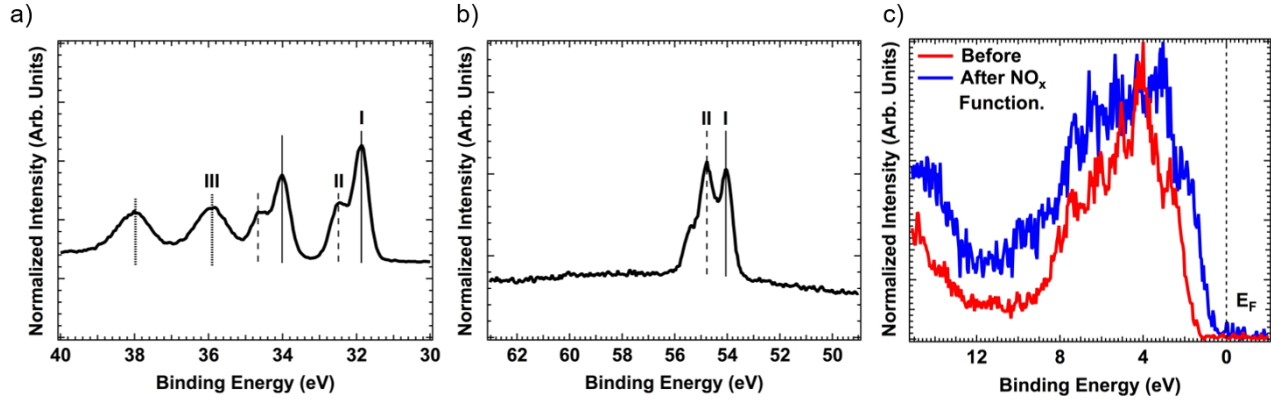
Figure 2.4 *(a) Tungsten core level via X-ray Photoelectron Spectroscopy (XPS) showing the formation of various $WSe_{2-x-y}O_xN_y$ species. Labels I, II, and III indicate W doublets of different oxidation states (b) Se 3d core level after NO_x chemisorption. Labels I and II indicate two different species of different Se oxidation states. (c) Valence band edge of WSe2 before and after NO_x; a definitive ~0.8 eV shift of the valence band edge is shown with respect to the Fermi level.*

2.5 Density Functional Theory Simulation

While XAS and XPS have narrowed down the resultant species after covalent functionalization on the sample surface, a host of possible configurations still exist given the ambiguity of the various oxidation states present. Density functional theory is subsequently used to predict the exact chemical configurations necessary that creates the measured doping electrical characteristics.

Therefore*, ab initio* simulation was used to examine the thermodynamic stability of $WSe_{2-x-y}O_xN_y$ species after NO_x functionalization and the changing band structure of WSe2 as a result. From Density Functional Theory (DFT) calculations, we observe energetically favorable adsorption of O, NO and NO_2 at Se vacancies (Table 1), which is consistent with the experimental observations. Notably, based on DFT calculations, adsorption was found to be unfavorable without the presence of Se vacancies.

In specific, First principles calculations were utilized based on DFT[36, 37] with plane wave basis sets and Projector Augmented Wave (PAW) pseudopotentials[37, 38] implemented in the Vienna *Ab initio* Simulation Package (VASP).[36, 39, 40] The electronic wave functions were represented by plane wave basis with a cutoff energy of 600 eV.

The exchange and correlation interactions are incorporated as a functional of the Generalized Gradient Approximation (GGA).[38, 41, 42] A 5×5 supercell of monolayer WSe_2 host was used for the simulations. Each model has ~18 Å vacuum to avoid interaction between replica images as a result of the periodic boundary conditions. NO, NO_2 and O were separately placed near a singular Se vacancy of WSe_2 (or pristine WSe_2) and allowed to relax energetically while the host cell size was kept fixed after optimization.

Adsorbates on Se Vacancies		
$\Delta E_{NO2:WSe2}$	$\Delta E_{NO:WSe2}$	$\Delta E_{O:WSe2}$
-1.0eV	-2.8eV	-4.8eV

Table 2.1: Binding energies of three adsorbates (NO_2, NO, O) on Se vacancies of WSe_2. The error for binding energy is within 0.1eV.

Out of all adsorbates, only NO adsorption is predicted to contribute to *p*-doping of WSe_2 based on DFT simulations. Figure 2.5 shows the relaxed configuration of chemisorbed NO with N bonding to W, similar to Figure 2.1(b)-iii configuration. By examining the band structure, we find that NO:WSe_2 configuration creates two defect bands close to the valence band edge shown in Figure 2.5(b). The red dash line, overlapping with one of the NO adsorption induced defect bands, represents E_F. The other two chemisorbed species have minimal effects on the carrier concentration of WSe_2 based on the DFT simulations (Figure 2.5(c)).
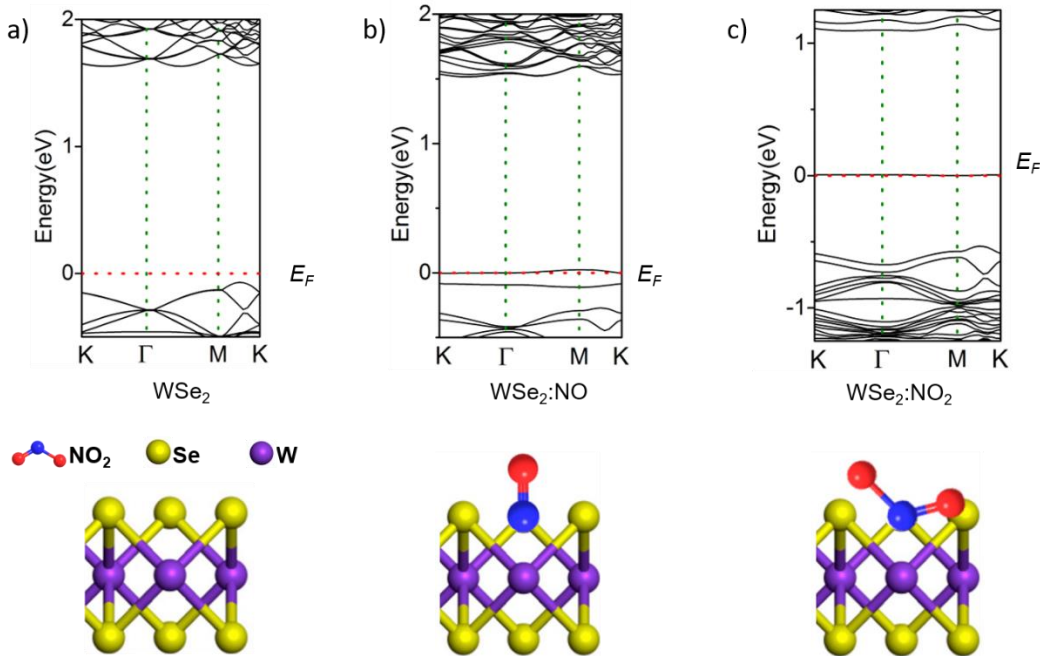

Figure 2.5 Ab initio simulation results showing (a) 5×5 supercell with optimized atomic configuration of NO on Se vacancy, with N atom bonding with surrounding W atoms. (b)

Band structure of WSe₂ and (c) band structure after NO adsorption in Se vacancy. The red dotted line indicates the Fermi level.

2.6 Structural Characterization

While XPS and XAS substantiated the covalent functionalization scheme, and helped identified the species responsible for doping with the aid of DFT, further characterizations are required to ensure that the no long range defect is introduced via covalent functionalization. To this end, we conducted x-ray diffraction (XRD), photoluminescence (PL), and Raman spectroscopy experiments on the sample to ensure long range crystal lattice integrity.

2.6.1. Photoluminescence

Photoluminescence involves exciting a sample optically and measuring the energy of the resultant output photon. By exciting the semiconducting sample with photons of a chosen wavelength (energy), excitons can be generated as long as the excitation energy rises above the bandgap minus excitonic binding energy (optical bandgap). Optical emission then originates from excitonic annihilation and directly correlates to the excitonic energy levels. Additionally, quantum yield can be inferred from properly calibrated PL measurements as emission intensity is directly correlated to the number of photons emitted, which when compared to the pump (excitation) leads to an efficiency ratio.

2.6.2. X-ray Diffraction

In x-ray diffraction, a large sample is placed under a monochromatic x-ray for investigation (with the wavelength chosen to conform to the expectation of the material's lattice constant). When illumination happens at an angle, the incoming x-ray will diffract with the different material planes, with the resultant reflections coming off of the crystal to interfere either destructive or constructively. The sample is rotated within an angle range, effectively allowing diffraction pattern to be created in every unique direction. Subsequently, the compiled reflection intensity is plotted vs. the angle of rotation, allowing for an accurate determination of the sample's lattice constants.

2.6.3. Raman Spectroscopy

Similar to photoluminescence, Raman spectroscopy also involves optical excitation and observation of the same from the sample in question. However, the excitation targets here are the electrons participating in intermolecular bonding. Therefore, the resultant photon emission is extremely sensitive to bond length and energy changes, in addition to any mechanical deformation that the material might undergo under external stimulus.

2.6.4. Characterization on NOₓ Covalent Functionalized WSe₂

The following includes PL, XRD, and Raman characterization on NOₓ functionalized WSe₂. XRD data in Figure 4a demonstrates that the overall WSe2 crystal structure remains intact as the two Miller index peaks 002 and 103 are preserved with similar intensities and no visible θ shifts. Figure 4b demonstrates the retention of the primary phonon modes E2g and A1g at 249 and 251 cm^{-1}, respectively, for a trilayer WSe2 before and after doping, consistent with the literature.[20,21] PL spectra in Figure 4c shows the two peaks (1.47 and 1.6 eV) of a tri-layer WSe2 unaffected by NOₓ

chemisorption.[22,23] From our XRD, Raman and PL characterizations, we conclude that doping functionalization does not compromise the unique properties of WSe$_2$ at the macroscopic level.
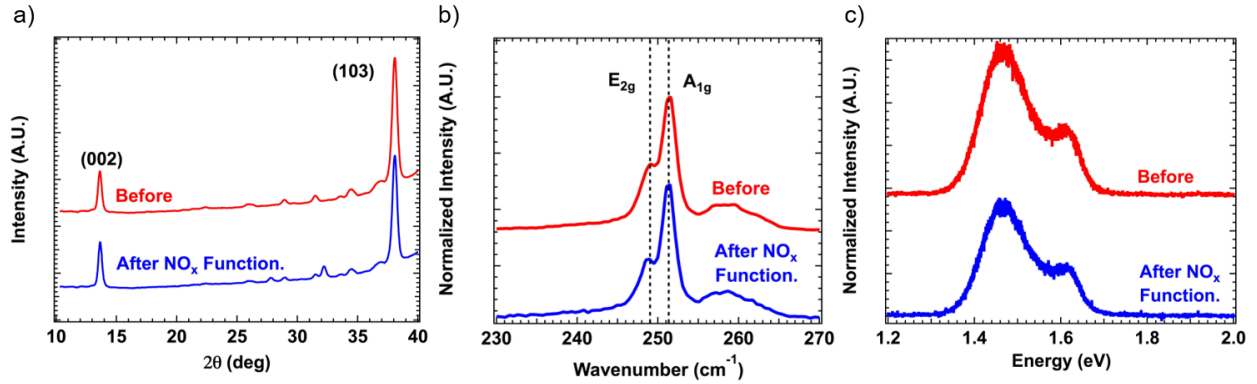

Figure 2.6. *(a) X-ray Diffraction (XRD) pattern of WSe$_2$ before and after WSe$_2$ doping. (b) Raman and (c) Photoluminescence (PL) spectra of the same tri-layer WSe$_2$ flake after NO$_x$ chemisorption.*

2.7 Layer Thickness Dependence and Contact Resistance Reduction

2.7.1. NO$_x$ Layer Dependence

Electrical measurements of WSe$_2$ devices before and after NO$_x$ chemisorption were performed. Two studies were conducted, the first being a time dependent doping study at varying thicknesses. Figure 5(a) shows a representative transfer characteristic of 7.5nm thick WSe$_2$ back-gated device as a function of NO$_x$ doping time. A progressively heavier *p*-doping can be observed, reflected by an increasing I_{on} and diminishing gate control. The increasing I_{on} displays a degree of doping tunability *via* doping time, with I_{on} eventually saturating to degenerate behavior. Doping concentration is explicitly extracted across three devices with different flake thicknesses of 0.7nm, 7.5nm and 78nm (monolayer is determined by optical microscopy and the rest determined by AFM in Figure S2) respectively *versus* doping time (Figure 5(b)). Assuming negligible R_c due to the thinning Schottky barrier at higher doping concentrations and therefore higher tunneling current, we can estimate doping concentration by first finding the 2D sheet charge density $n_{2D} = (I_{DS}L)/(qWV_{DS}\mu_p)$ at V_G=0 where V_{DS} is the drain voltage, L and W the length and width of the channel, q the unit electron charge and μ_p the field effect hole mobility respectively. From n_{2D}, we find volume doping concentration which saturates to ~1×10^{19}cm^{-3} across all three devices. The similar saturated doping level across all three devices demonstrates a uniform volume doping throughout the WSe$_2$ surface and body, supporting the XAS results discussed earlier. Notably, the electrically extracted saturation doping concentration is consistent with that extracted from XPS measurements.

25
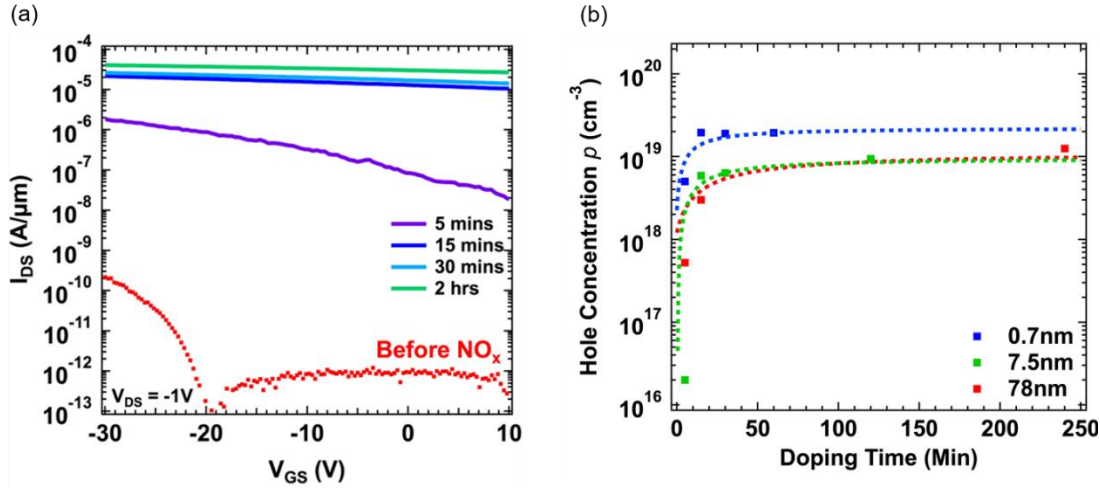
Figure 2.7 (a) Representative I_{DS}-V_{GS} for WSe₂ device exposed to NO₂ at different functionalization time. (b) Extracted doping concentration vs doping time for different flake thicknesses. All doping levels saturate at ~10^{19} cm⁻³

2.7.2. Transfer Line Method (TLM) on Backgate NOₓ Functionalized WSe₂

Contact resistance, R_c was extracted before and after NOₓ chemisorption using the transfer line method (TLM).[43] Figure 2.8(a) shows the transfer characteristics of TLM devices with channel lengths of 500nm, 1μm, 1.5μm and 2μm fabricated on a WSe₂ flake with a thickness of ~7 nm (Figure 2.8(b) inset). The observed low I_{on} and ambipolar behavior prior to doping implies a large R_c due to Schottky barrier height near the WSe₂ mid-gap. After doping however, we see a significant increase in I_{on} indicating a decrease in R_c. Using $R_{total} = 2R_{contact} + R_{channel}(L)$, where R_{total} and $R_{channel}$ are the unit-width normalized total resistance and channel resistance, R_c is found to be 0.13GΩ-μm and 1.27kΩ-μm before and after NOₓ chemisorption, respectively (Figure 2.8(b)-(c)). NO₂ doping is shown to reduce the R_c by a remarkable 5 orders of magnitude. Finally, we revisit WSe₂ doping extraction including R_c, and find again consistent doping level p ~ 1.6×10^{19}cm⁻³.
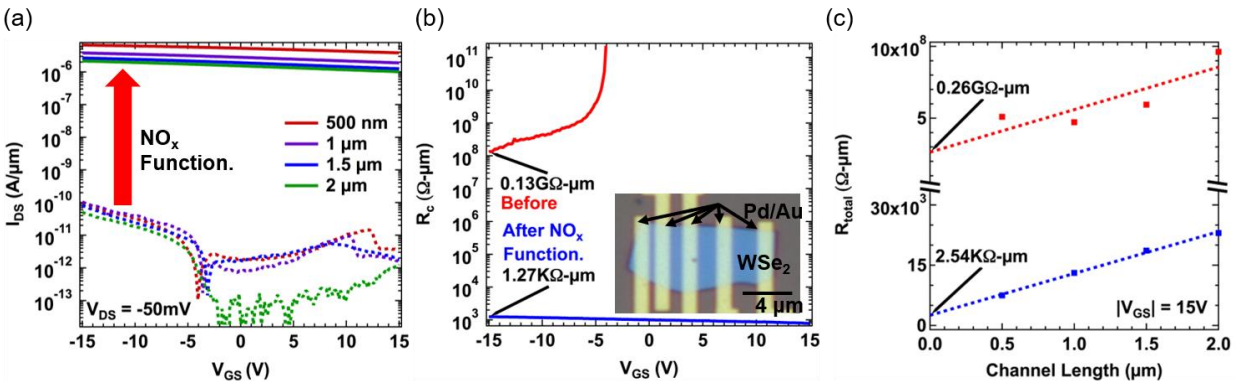
Figure 2.8. (a) I_{DS} -V_{GS} of TLM device before and after NO₂ treatment, showing a (b) 5 orders of magnitude decrease in contact resistance. Inset: Optical microscopy of fabricated back-gated device used for TLM. (c) Extracted total resistance change before/after NOₓ functionalization at $|V_{GS} = 15 \, V|$.

2.8 Conclusion

In summary, we have demonstrated air stable p-doping of WSe_2 via covalent functionalization by NO_x at an elevated temperature of 150 °C. The stability of this covalent bonding scheme enables indepth characterization via XAS and XPS, confirming $WSe_{2-x-y}O_xN_y$ species formation due to $NO_x$ chemisorption on both the $WSe2$ surface and body. From XPS, a shift of ~0.8 eV of E_F toward E_V also concludes a degenerate doping situation. In addition, all observed $WSe_{2-x-y}O_xN_y$ species are shown to be energetically favorable from *ab initio* simulations, with $NO:WSe_2$ identified as the dominant configuration leading to p-doping. Our time dependent doping study also indicates doping tunability, and the TLM study further confirms the extracted doping concentration of 1.6 x 10^{19} cm^{-3} while also showing a remarkable ~5 orders of magnitude R_c reduction via NO_x functionalization. Controllable semiconductor doping is an important and fundamental enabler in the general field of electronic devices, and degenerate materials can be utilized anywhere from contact materials to junctions in tunneling devices. Therefore, our demonstration of air stable doping through covalent functionalization of WSe_2 presents another route for further enhancing and manipulating TMDC functionalities and applications.

As mentioned above, the steady progression of TMD surface defect passivation also requires parallel surface defect engineering for developing a deeper understanding of the TMD surface defects and extraction of key material properties. This work demonstrates that defects can also be engineered to satisfy specific electronic device requirements needed for material behavior and underline a possible alternative to complete surface passivation in realizing nanoelectronics built via TMDs.

REFERENCES

1.   Geim, A. K.; Novoselov, K. S. *Nature Materials* **2007,** 6, 183.
2.   Lee, Y.-H.; Zhang, X.-Q.; Zhang, W.; Chang, M.-T.; Lin, C.-T.; Chang, K.-D.; Yu, Y.-C.; Wang, J. T.-W.; Chang, C.-S.; Li, L.-J.; Lin, T.-W. *Adv. Mater.* **2012,** 24, (17), 2320-2325.
3.   Benameur, M. M.; Radisavljevic, B.; Héron, J. S.; Sahoo, S.; Berger, H.; Kis, A. *Nanotechnology* **2011,** 22, (12), 125706.
4.   Addou, R.; Colombo, L.; Wallace, R. M. *ACS Appl. Mater. Interfaces* **2015,** 7, (22), 11921-11929.
5.   Amani, M.; Taheri, P.; Addou, R.; Ahn, G. H.; Kiriya, D.; Lien, D.-H.; Ager, J. W.; Wallace, R. M.; Javey, A. *Nano Lett.* **2016,** 16, (4), 2786-2791.
6.   McDonnell, S.; Addou, R.; Buie, C.; Wallace, R. M.; Hinkle, C. L. *ACS Nano* **2014,** 8, (3), 2880-2888.
7.   Cui, N.-Y.; Brown, N. M. D.; McKinley, A. *Appl. Surf. Sci.* **1999,** 151, (1), 17-28.
8.   Tsai, C.; Li, H.; Park, S.; Park, J.; Han, H. S.; Nørskov, J. K.; Zheng, X.; Abild-Pedersen, F. *Nat. Commun.* **2017,** 8, 15113.
9.   Jin, Z.; Li, X.; Mullen, J. T.; Kim, K. W. *Phys. Rev. B* **2014,** 90, (4), 045422.
10.   Fox, D. S.; Zhou, Y.; Maguire, P.; O'Neill, A.; Ó'Coileáin, C.; Gatensby, R.; Glushenkov, A. M.; Tao, T.; Duesberg, G. S.; Shvets, I. V.; Abid, M.; Abid, M.; Wu, H.-C.; Chen, Y.; Coleman, J. N.; Donegan, J. F.; Zhang, H. *Nano Lett.* **2015,** 15, (8), 5307-5313.
11.   Makarova, M.; Okawa, Y.; Aono, M. *The Journal of Physical Chemistry C* **2012,** 116, (42), 22411-22416.

12.	Amani, M.; Lien, D.-H.; Kiriya, D.; Xiao, J.; Azcatl, A.; Noh, J.; Madhvapathy, S. R.; Addou, R.; Kc, S.; Dubey, M.; Cho, K.; Wallace, R. M.; Lee, S.-C.; He, J.-H.; Ager, J. W.; Zhang, X.; Yablonovitch, E.; Javey, A. *Science* **2015,** 350, (6264), 1065.

13.	Gogoi, P. K.; Hu, Z.; Wang, Q.; Carvalho, A.; Schmidt, D.; Yin, X.; Chang, Y.-H.; Li, L.-J.; Sow, C. H.; Neto, A. H. C.; Breese, M. B. H.; Rusydi, A.; Wee, A. T. S. *Phys. Rev. Lett.* **2017,** 119, (7), 077402.

14.	Kim, H.; Lien, D.-H.; Amani, M.; Ager, J. W.; Javey, A. *ACS Nano* **2017,** 11, (5), 5179-5185.

15.	Cho, K.; Min, M.; Kim, T.-Y.; Jeong, H.; Pak, J.; Kim, J.-K.; Jang, J.; Yun, S. J.; Lee, Y. H.; Hong, W.-K.; Lee, T. *ACS Nano* **2015,** 9, (8), 8044-8053.

16.	Radisavljevic, B.; Radenovic, A.; Brivio, J.; Giacometti, V.; Kis, A. *Nature Nanotechnology* **2011,** 6, 147.

17.	Fang, H.; Chuang, S.; Chang, T. C.; Takei, K.; Takahashi, T.; Javey, A. *Nano Lett.* **2012,** 12, (7), 3788-3792.

18.	Zhao, P.; Kiriya, D.; Azcatl, A.; Zhang, C.; Tosun, M.; Liu, Y.-S.; Hettick, M.; Kang, J. S.; McDonnell, S.; Kc, S.; Guo, J.; Cho, K.; Wallace, R. M.; Javey, A. *ACS Nano* **2014,** 8, (10), 10808-10814.

19.	Zhang, Y. L.; Wu, Z. F.; Chen, B. H.; Xu, L. S.; Pan, H. B.; Ma, Y. S.; Jiang, Z. Q.; Zhu, J. F.; Huang, W. X. *Chin. Sci. Bull.* **2010,** 55, (34), 3889-3893.

20.	Huffman, R. E.; Davidson, N. *J. Am. Chem. Soc.* **1959,** 81, (10), 2311-2316.

21.	Poteat, T. L.; Lalevic, B. *Electron Device Letters, IEEE* **1981,** 2, (4), 82-84.

22.	Brown, G. E.; Waychunas, G. A. X-ray Absorption Spectroscopy: Introduction to Experimental Procedures. http://www-ssrl.slac.stanford.edu/mes/xafs/xas_intro.html

23.	Fang, H.; Tosun, M.; Seol, G.; Chang, T. C.; Takei, K.; Guo, J.; Javey, A. *Nano Lett.* **2013,** 13, (5), 1991-1995.

24.	Liu, G.; Rodriguez, J. A.; Hrbek, J.; Dvorak, J.; Peden, C. H. F. *J. Phys. Chem. B* **2001,** 105, (32), 7762-7770.

25.	Okumura, K.; Amano, J.; Yasunobu, N.; Niwa, M. *J. Phys. Chem. B* **2000,** 104, (5), 1050-1057.

26.	Overbury, S. H.; Mullins, D. R.; Huntley, D. R.; Kundakovic, L. *J. Catal.* **1999,** 186, (2), 296-309.

27.	Tronc, M.; King, G. C.; Read, F. H. *J. Phys. B: At., Mol. Opt. Phys.* **1980,** 13, (5), 999.

28.	Wight, G. R.; Brion, C. E. *J. Electron. Spectrosc. Relat. Phenom.* **1974,** 4, (4), 313-325.

29.	Colton, R. J.; Rabalais, J. W. *Inorg. Chem.* **1976,** 15, (1), 236-238.

30.	Hollander, J. M.; Jolly, W. L. *Acc. Chem. Res.* **1970,** 3, (6), 193-200.

31.	Biloen, P.; Pott, G. T. *J. Catal.* **1973,** 30, (2), 169-174.

32.	Kerkhof, F. P. J. M.; Moulijn, J. A.; Heeres, A. *J. Electron. Spectrosc. Relat. Phenom.* **1978,** 14, (6), 453-466.

33.	Cho, D. H.; Chang, T. S.; Shin, C. H. *Catal. Lett.* **2000,** 67, (2-4), 163-169.

34.	Joyce, W. B.; Dixon, R. W. *Appl. Phys. Lett.* **1977,** 31, (5), 354-356.

35.	Späh, R.; Lux-Steiner, M.; Obergfell, M.; Bucher, E.; Wagner, S. *Appl. Phys. Lett.* **1985,** 47, (8), 871-873.

36.	Kresse, G.; Furthmüller, J. *Comput. Mater. Sci.* **1996,** 6, (1), 15-50.

37.	Yang, R. G. P. a. W., *Density-Functional Theory of Atoms and Molecules.* Oxford University Press: New York, 1989.

38.	Kohn, W.; Sham, L. J. *Phys. Rev.* **1965,** 140, (4A), A1133-A1138.

39.	Blöchl, P. E. *Phys. Rev. B: Condens. Matter* **1994,** 50, (24), 17953-17979.

40.	Kresse, G.; Joubert, D. *Phys. Rev. B: Condens. Matter* **1999,** 59, (3), 1758-1775.

41.	Kresse, G.; Furthmüller, J. *Phys. Rev. B: Condens. Matter* **1996,** 54, (16), 11169-11186.

42.	Kresse, G.; Hafner, J. *Phys. Rev. B: Condens. Matter* **1993,** 47, (1), 558-561.

43.	Berger, H. H. *Solid-State Electron.* **1972,** 15, (2), 145-158.

Chapter 3 Edge Defects and Edge Recombination Velocity

3.1. Edge Defects

Chapter 2 gave an overview of TMD surface defects, passivation strategies, and engineering approaches. From here, we proceed to investigate edge defects, their quantitative characterization techniques, and possible passivation schemes. Edge defects are becoming a topic of intense interest due to a). the relatively well understood utilization of TMD based long channel devices and b). the need of aggressive lateral scaling to match the length scale current SiGe based FETs operate in to enable adequate performance comparison. Traditionally, 3D materials consist of bulk and surface defects, the latter of which become relevant when scaling becomes aggressive and surface area to volume ratio increases substantially. Therefore, 2D TMDs (with its strong material anisotropy in the z-direction) can be thought to have, instead of bulk and surface, surface and edge defects, the latter of which also strongly relevant in aggressively scaled regimes. Figure 3.1 underlines this material corollary, and stresses that proper understanding of TMDs at the low dimensions will require a deep understanding of the edge defects, similar to that of surface defects for 3D materials. In this chapter, we introduce the types of edge defects present and derive a quantitative metric for describing nonradiative carrier recombination edge sites, directly inferring edge defect concentration.
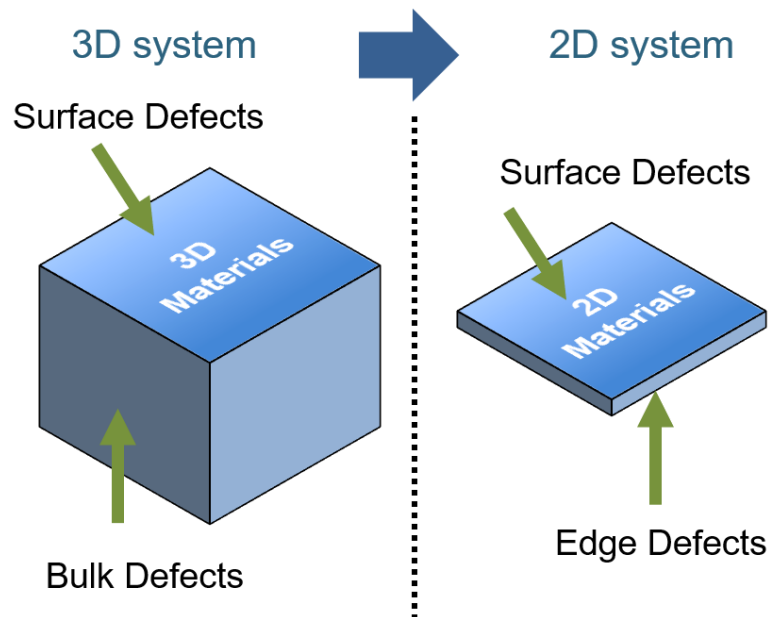

Figure 3.1 *Illustrative approach to classifying the two types of defects that exist in 3D material systems compared to that of 2D. Therefore, at aggressive scaling, edge defects of 2D systems become important to understand, just like that of surface defects of 3D systems.*

3.1.1. Ideal Edges

TMDs possesses hexagonal unit cells. Referring to the Z projection of a TMD monolayer, the hexagonal lattice is identical to that of a graphene lattice. Expectedly, the edge structure can also vary between the two different edge types of "zig-zag" and "armchair", sharing the same name with the two well known cases of graphene edge types.
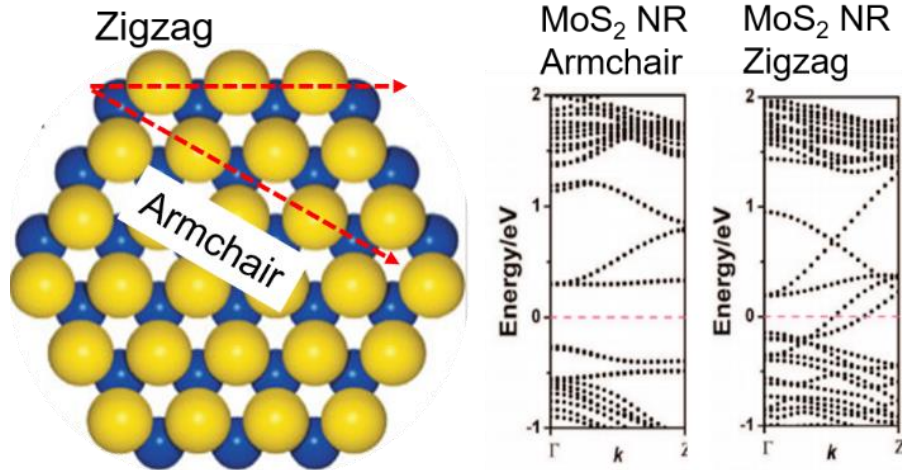
Figure 3.2. *Top-down view of TMDs with the yellow ball model signifying a transition metal element and the blue ball model signifying a chalcogen element respectively. Under ideal conditions and fabricating nanoribbons along either the zigzag or armchair direction along the red dotted line, DFT simulation predicts either a semiconducting (armchair) or metallic (zigzag) behavior from band structure.[1]*

Simulations have shown that nanoribbons (NR) with these two distinct edge structures have different band structures. Zigzag is known to be semiconducting while armchair is known to be metallic.[1, 2] However, not much experimental validation exists for the simulation predictions, likely due to both complications in an ideal edge synthesis and its subsequent characterization. The most recent work of bottom up synthesized $MoSe_2$ edges characterized via STM seem to suggest conflicting results with simulation and realizing zigzag $MoSe_2$ NRs with a small ~half eV bandgap. However, the "ideality" of the edge is still in question with the authors admitting possible excessive selenium adatoms during NR formation.[3] Overall the experimental validation of ideal edge behavior is a topic in investigation.

For any ideal TMD nanostructure termination, all edge structures are either armchair, zigzag, or a linear superposition of the two. Edge defects simply means any termination structure deviating from the ideal cases presented here, consisted either of the same or different elements from the AB_2 host.

3.1.2. Experimental Edge Realizations and Challenges

Various approaches are used to towards synthesize TMD edge structures. Due to this, seemingly conflicting results can be reported between TMDs of similar structures

(with some edges acting as luminescence sites where others recombine carriers non-radiatively).[3-5] Currently, top down is more utilized towards achieving TMD nanostructures due to more indepth understanding of the process involved and relative ease of operation. A host of techniques ranging from dry etching, electron and ion bombardments have all been applied to realize different edge types.[6-9] However, all top-down realized edges so far possesses different variations from the "ideal" edge structure aforementioned.

In the atomic limit, MoS_2 nanoribbons have been realized via transmission electron microscopy (TEM). At the limit of 1 nm ribbon width, the material becomes conductive due to the loss of standard MoS_2 stoichiometry as the chalcogens are more prone to removal than its transition metal counterpart. The proposed stoichiometry (Mo_5S_6) obviously deviates away from an "ideal" edge structure.[7] More generally, gas etch has been employed to pattern TMDs during nanoelectronics fabrication, without in-depth characterization of the edge structure at the atomic resolution.[8]

Overall, fundamental roadblock exists for achieving "ideal" edge structure from a top down approach. The presence of an etch mask for example, and the intrinsic "sidewall" formation that occurs in the etching process all contributes to foreign adatoms or covalently bonded at the edge.[10] Therefore, the proper approach, even in a top down scheme, is to rely on techniques that do not prominently introduce foreign atoms into the system while realizing new edge sites. Following this vein, the closest realization of "intrinsic" edge structure comes from thermal annealing of a CVD MoS_2 at high temperature. While the utility of such techniques is still questionable, the work itself signifies a major step in "intrinsic" edge realization from a top down scheme.[11]

By comparison, bottom up synthesis of TMDs also possess more challenges compared to top down TMD synthesis and bottom up synthesis of other similar 2D materials such as graphene. Here, the culprit lies most likely in the yet thoroughly understood chemistry of the system, and the complications in 3 stacked atom syntheses compared to just one layer of graphene. As of late, the closest experimental realization of "ideal" edge structure is the aforementioned nanoribbon synthesis via "phase change".[3] The subsequent characterization however conflicts with simulation predictions and is still a point of current contention.

3.1.3. Edge Characterization Methods

Given the varieties of edge structures possible both via top down and bottom up, a universal characterization method is required to compare the defects accrued across all these different methods and evaluate how close each edge type realized is to the ideal case. Similar to that of the surface defects, the most direct techniques involve either direct surface metrology or optical characterizations. Unlike surface case however, edge is a "1D" structure vs. that of the surface "2D" structure. This difference limits direct surface characterization to methods such as STM or TEMs, both of which are utilized extensively in the previous collection of cited works.

While STM or TEMs can offer direct structural evidence of edge defects and aid in characterization the exact atomic deviations however, the characterization method suffers from two limitations. First, their intrinsically low spatial range and stringent sample requirements prevents both techniques from being a facile evaluator of general edge qualities. Second, structural characterization still lacks vital information such as carrier interactions and subtleties of recombination behaviors relevant for devices applications.

To address the second issue raised while retaining high spatial resolution, efforts have been made towards non-destructive optical characterization combined with superior spatial resolution probe-based characterizations. This combined technique is demonstrated via the use of ultra-sharp Au tips to enhance the electrical field of the excitation laser into a subwavelength space via surface plasmon effects. Subsequently, emission from the material is also collected using the same probe, resulting in unprecedented spatial resolution PL mapping and qualitatively showing edge recombination centers for CVD grown MoS_2 in the 10s nm length regime.[12] This specific characterization now answers recombination dynamics, but still suffers from the characterization speed. Additionally, the reliance of surface plasmon means excitation and collection wavelength is limited to the resonance of the metal peak. Therefore, to conduct the same experiment on WS_2 (compared to MoS_2, whose respective monolayer emission are at ~620nm and ~660nm respectively), a new metal would be required for the campanile tip.

To achieve both a facile and meaningful characterization of edge defects in relation to their recombination mechanisms, a new technique is presented in the following section to satisfy these goals. This characterization method utilizes the traditional steady state and dynamic PL measurement techniques toward edge defect characterization. Monolayers are first patterned down into sizes comparable to the diffusion length, and then quantum yield is carefully measured and plotted as a function of further decreasing size. Additionally, the quantum yield is confirmed using both steady state and dynamic PL decay of the patterned TMD system. Finally, one can infer a quantitative metric relating to the quantum yield as a function of the changing critical dimension of the system, calculating directly the density of non-radiative recombination sites at the edge.[10]

3.2 Edge Recombination Experiment Approach

Figure 3.3 illustrates the expected light emitting behavior of spatially confined WS_2 monolayer disks under optical excitation, where nonradiative recombination happens mostly at the material edge. This edge quenching is associated with the introduction of non-radiative recombination sites during the etching process, and the intrinsic metallic nature of certain edge configurations.[13] To quantitatively characterize the radiative quenching, arrays of WS_2 monolayer disks of fixed diameters (*d*) are fabricated by lithography and dry etching. Subsequently, their PL iQY and effective carrier lifetimes ($\tau_{effective}$) are measured via steady-state and time-resolved PL spectroscopy (TRPL) respectively (see SI for experimental method details).[14] The process is then repeated for

different values of *d.* The circumference to surface area ratio increases as *d* decreases (Fig. 1b). As a result, PL iQY and $\tau_{effective}$ are expected to decrease with decreasing *d.* Finally, an expression from a diffusion-based model (details in SI) can be used to predict the $\tau_{effective}$ versus *d* relation. A fit of the data to the theoretical predictions determines ERV. Figure 1c shows the atomic force microscopy (AFM) images of patterned WS$_2$ monolayer disks of varying diameters: 1 μm, 750 nm, 500 nm, 250 nm and 100 nm. Note that for *d* = 100 nm, a disk array is adapted to achieve a higher signal-to-noise ratio for photoluminescence measurements.
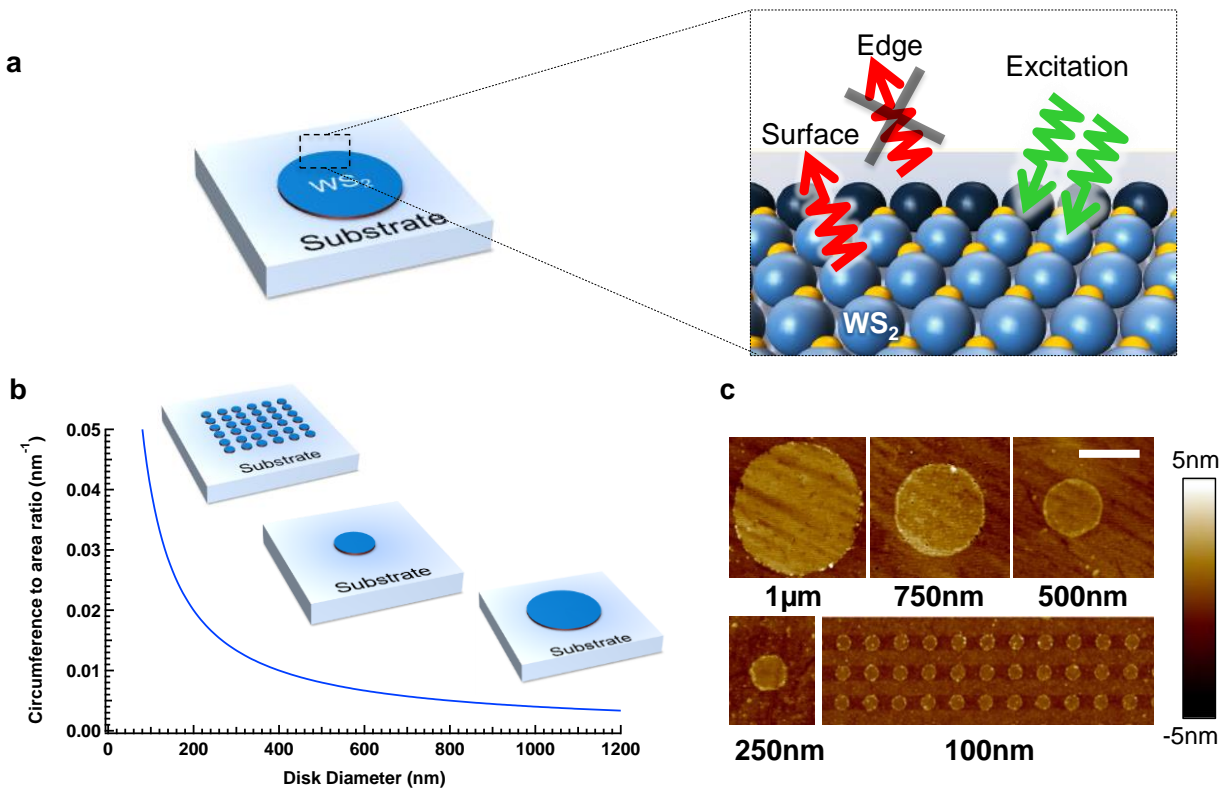
Figure 3.3 *Experimental approach used to probe the WS$_2$ monolayer edge after a top-down fabrication scheme. (a) Schematic showing optical excitation response. The monolayer only emits at the surface region away from the edge, while the edge itself is expected to recombine the generated carriers non-radiatively. Note that the darker ring at the edge is illustrative only and does not accurately represent the actual atomic structure of the WS$_2$ edge. (b) Circumference to area ratio of disks fabricated with different diameters, showing a steady increase as diameter decreases (c) Atomic force microscopy (AFM) of WS$_2$ disks of all chosen diameters. Both the single disks (1 mm to 250 nm) and the array structure (100 nm) are presented. The scale bar is 500 nm for all AFM scans.*

3.3. Photoluminescence and Internal Quantum Yield (iQY)

Figure 3.4a shows the PL spectra of WS$_2$ disks ranging from 1 μm to 100 nm in diameter, with the corresponding normalized spectra shown in the inset. The PL spectra

are normalized with respect to the fill factor, directly correlating the decreasing intensity trend to an increasingly dominant edge recombination mechanism. Additionally, no obvious sub-gap emission or peak change is observed across spectra of different diameters shown by the inset, signifying that the radiative recombination mechanism and the optical bandgap remains unaffected for the explored diameter range.[15]

The photoluminescence internal quantum yield (PL iQY) of the WS$_2$ disks is extracted as a function of pump intensity (corresponding to a calculated exciton generation rate). As shown in Figure 2b, there is a monotonic decrease of iQY as d decreases. The general iQY behavior for larger d disks is consistent with the analytical model proposed in previous studies where a pump independent and pump dependent behavior is observed at different generation regimes.[14, 16] Specifically, the generated carriers in WS$_2$ monolayers at steady state, G, can be balanced via a steady state recombination rate, R, via:

$$G = R = B_{nr}n^2 + B_r n^2 \qquad (1)$$

where B_{nr} is the non-radiative free carrier recombination rate due to surface defects, n is the free carrier concentration, and B_r is the formation rate of excitons in the system. At steady state, B_r can be further described via

$$B_r n^2 = \frac{\langle N \rangle}{\tau_{rad}} + C_{bx}\langle N \rangle^2 \qquad (2)$$

where $\langle N \rangle$ is the exciton concentration, τ_{rad} is the radiative recombination lifetime, and C_{bx} is the biexcitonic recombination rate.

The above model includes three recombination mechanisms with distinct recombination rates (surface radiative $1/\tau_{rad}$, surface non-radiative B_{nr}, and biexcitonic C_{bx}). The first two mechanisms have the same power dependence and compete directly at the lower generation regime as $R \propto n^2 \propto \langle N \rangle$, while the last mechanism becomes dominant at higher generation regime with $R \propto \langle N \rangle^2$ and contributes to the iQY pump dependence. The model also accurately describes the experimental iQY behavior of an unetched WS$_2$ monolayer shown in Figure 2b, and can be fitted closely utilizing similar values of $1/\tau_{rad}$ and C_{bx} mentioned in our previous work.[16] As d decreases however, we observe a corresponding iQY decrease at lower generation regime and a convergence of iQY independent of d at the higher generation regime. The clear d dependence at lower pump power points to an edge recombination rate competing with the radiative and surface non-radiative recombination rates. The iQY convergence at higher pump power points to the previously mentioned biexcitonic recombination mechanism, overriding the d dependence. As expected, iQY at smaller d seems to exhibit minimal pump dependence, even at the higher generation rates, likely due to an increasingly dominant edge recombination competing with the biexcitonic recombination mechanism.
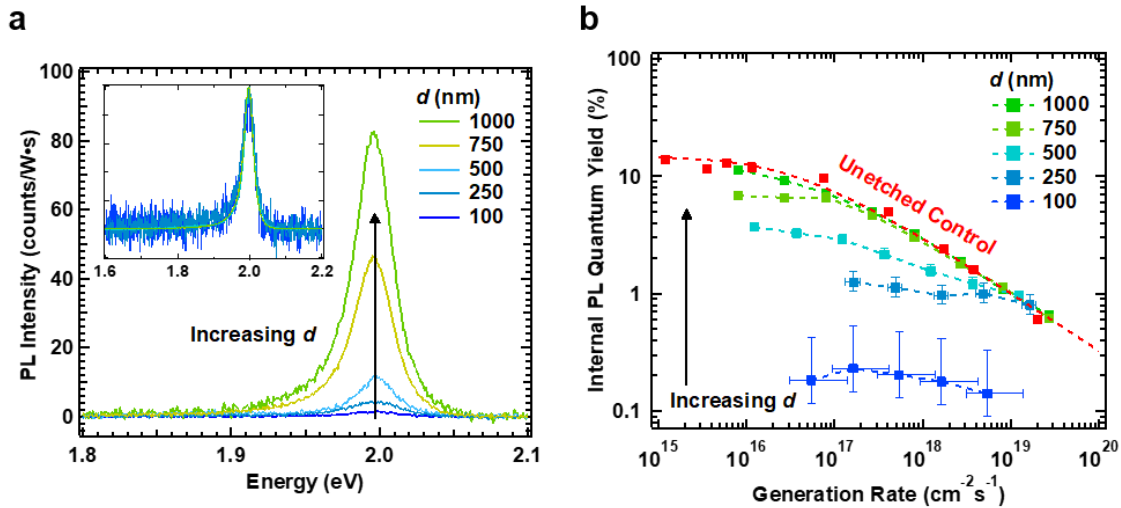
Figure 3.4. *Optical characterizations of WS$_2$ monolayer disks. (a) Photoluminescence (PL) measurements of WS$_2$ disks with increasing diameter (corrected for fill factor), showing a steady increase in the emission intensity. The inset shows normalized spectra and indicates that no significant sub-gap emission is observed across all changing diameters. (b) PL internal quantum yield of WS$_2$ versus generation rate, as a function of disk diameter. Error bars associated with the samples originate from absorption measurements.*

3.3.1 Calibrated Laser Spot Size

Laser spot size for this experiment is of particular importance due to our disk sizes, and the fabricated single disk (or array) structures have all been designed to accommodate for this factor. We measured the beam shape in our micro-PL system by taking an image of the beam using our optical microscope. A profile of the beam intensity is shown in Fig. S1 a, and can be fit using a Gaussian distribution with a standard deviation of +/- 0.7 □m. All single disk sizes fall within +/- 1 standard deviation from the mean (1.4 □m). Fig. S1 b shows the variation in intensity due to the beam's Gaussian nature as a function of disk size. We see that the excitation peak intensity variation yields ~30% difference between the largest (1 □m) and smallest (250 nm) single disk structures. We utilize the Gaussian beam distribution to calculate the incident laser power on the sample.

To accommodate for the measured beam spot size, single disks from 1 □m to 250 nm in diameter are fabricated in the middle of an 8 □m x 8 □m field (whose field size is chosen to give comfortable tolerance to both stage drifts and accommodate the measured beam spot size), where the exposed regions are subsequently etched away, leaving only the desired WS2 monolayer disk at the field center. The field clearance allows the optical setup to only collect the luminescence contribution from the monolayer disk itself, and not from nearby unetched WS2. For disk diameters of 100 nm, a disk array is fabricated across an 8 μm x 8 μm field with a center to center disk spacing of 200 nm. The array is designed to maximize signal to noise ratio due to low iQY of the 100 nm disks.

Lastly, special care is also taken during measurement to ensure that the single disk rests directly under the peak excitation intensity. To verify this, each spectra of the single disk sample is taken multiple times as the stage is shifted in all 4 planar directions. This is repeated until the photoluminescence signal is maximized, where we assume that the peak of the laser intensity is exciting the sample disk.
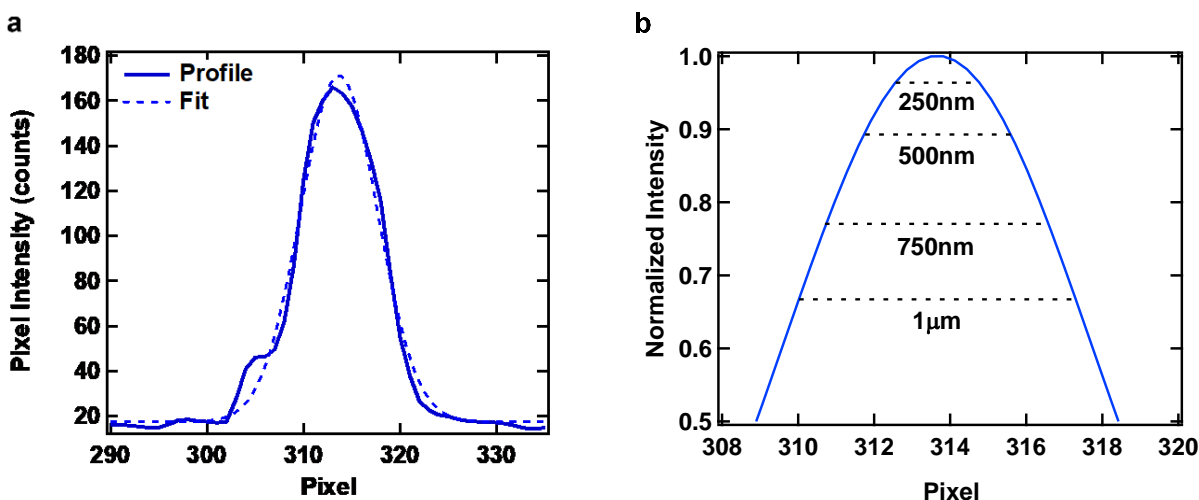

Figure 3.5. *Laser spot size calibration. (a) Intensity profile of the laser spot size measured in the micro-PL microscope camera. A ~123 nm/pixel scale is determined using a calibrated length standard. A standard Gaussian distribution is to fit the profile with a single standard deviation 0.7 µm in length. (b) Comparison of disk size with that of the beam shape. The Gaussian beam shape yields a ~30% difference in the peak intensity between the largest (1 µm) and the smallest (250 nm) single disk size samples.*

3.3.2 Subwavelength Absorption

Due to the subwavelength nature of the disk diameters (compared to the 514nm excitation wavelength), it is important to experimentally measure absorption for the smaller disk sizes. WS2 disk arrays of 500 nm, 250 nm, and 100 nm were fabricated on quartz for absorption measurements. Specifically, repeating disks of a chosen diameter is patterned across an 8 □m x 8 □m field (with a center to center spacing of 2d). The samples are mounted in a transmission microscope, allowing for measurement of the reflected and transmitted laser power in the sample and on a blank quartz substrate. Fig. S2 shows the absorption calculated from the reflection and transmission results for all three array sizes. Due to the array structure utilized in all three sizes, the measured absorption incorporates both the intrinsic absorption change and the array fill factor. A constant fill factor of ~20% is calculated given the center to center spacing, and the intrinsic absorption is then extracted. The results here allow us to calculate both the generation rate and PL iQY of the smaller disk samples at the subwavelength regime.

36

It is important to note that due to its low absorption value the 100 nm diameter sample shows significant measurement variation. This is directly reflected by the error bars in Figure 2b.
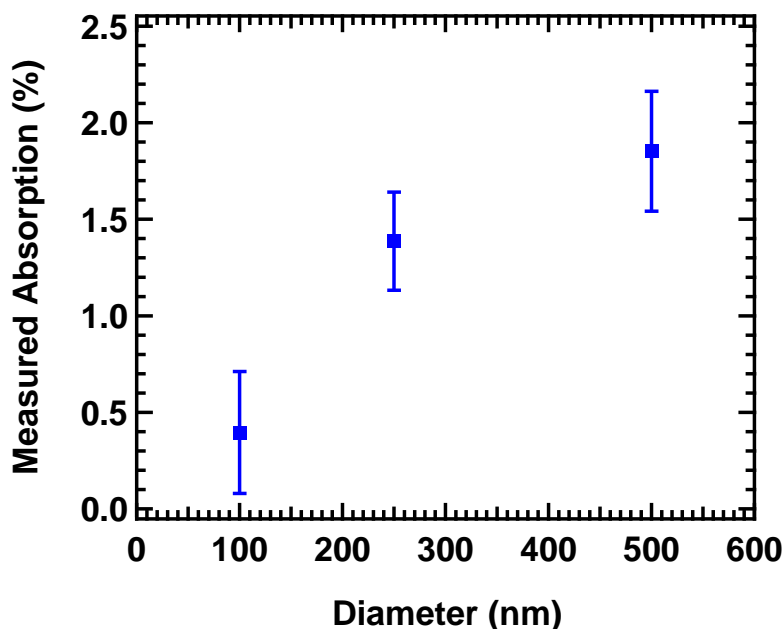
Figure 3.6. *Absorption Measurements of disks with d $\geqslant$ 500 nm. A disk array is utilized for all three sizes in order to maximize signal to noise ratio. The absorption is derived by a one beam transmission/reflection setup where the signal is collected by a photodetector and read by a lock-in amplifier. The error bars represent uncertainty of multiple reflection and transmission measurements.*

3.4 Time-Resolved Photoluminescence (TRPL) Lifetime

3.4.1 TRPL Theory

Compared to PL, TRPL measures the optical recombination process responsible for the light emission at a relevant time scale. Similar to PL, a packet of photon is sent towards the TMD sample at the appropriate energy for carrier excitation and later optical recombination. In TRPL however, the photon packets are sent in a periodic manner (pulsed laser excitation) at a frequency called the repetition rate, where the photon number is counted. After excitation, the generated carriers will undergo different recombination mechanisms in the TMD where the radiative component will be collected by the microscope setup and sent to a photon counting diode (silicon-based avalanche photodiode or streak camera depending on the anticipated decay time). Ideally, the repetition rate and photon packet sizes are optimized such that enough time is given to the TMD to equilibrate before the next excitation pulse.

On the detector side, a timing mechanism is connected between the pulsed excitation source. This way the detector can correlate the oncoming photon with the

specific photon responsible for the emission. Due to photon loss in instrument collection, sample quantum yield, and detector deadtime, approximately a few emission photons can be collected per excitation pulse. Therefore, by repeated bombarding the sample with photon packets and binning the output photon into the appropriate delay time interval between excitation and collection, a histogram of the decay profile can be mapped as more counts are collected as a function of the delay time interval. Overtime, the histogram will come to represent a single decay curve due to statistical likelihood of collecting more photons closer to instantaneous moment of excitation.

3.4.2. TRPL Lifetime Extraction

To further understand the edge recombination mechanism and measure ERV, we use TRPL to extract the lifetimes of carriers in WS_2 disks as a function of their diameters. Figure 3 shows the generated exciton concentration decay versus time of different diameter disks, demonstrating a faster lifetime decay as d decreases. As expected, two different regimes of lifetime decay are observed in the TRPL data. At the higher generated exciton density regime, biexcitonic recombination is observed (corresponding to the converging iQY in Figure 3.4b at the higher generation rate), dominating the lifetime decay across all disk sizes independent of d. As the exciton concentration decays over time however, lower order recombination mechanisms become observable. These mechanisms can be classified into three types: radiative and non-radiative surface mechanisms, and a non-radiative edge mechanism. To determine the ERV, we fit a decay lifetime $\tau_{effective}$ incorporating all three aforementioned lifetime components at the lower generated exciton density assuming negligible biexcitonic recombinations. In this approximation, a single exponential decay fit can be applied via:[17]

$$\frac{d\langle N \rangle}{dt} = -\frac{\langle N \rangle}{\tau_{\mathrm{effective}}} \tag{3}$$

where $\tau_{effective}$ conforms to the following Matthiessen's relation:

$$\frac{1}{\tau_{\mathrm{effective}}} = \frac{1}{\tau_{\mathrm{rad}}} + \frac{1}{\tau_{\mathrm{nrad}}} + \frac{1}{\tau_{\mathrm{edge}}} \tag{4}$$

Specifically, τ_{rad} and τ_{nrad} are the surface radiative and non-radiative recombination lifetime measured as 3.4 ns and 2.4 ns respectively in our previous work.[10] Decay curves in Figure 3 are fitted using both a single exponential decay at low generated exciton density as well as convoluting the single exponential decay with a measured instrument response function iteratively against experimental data to ensure accuracy.[18]
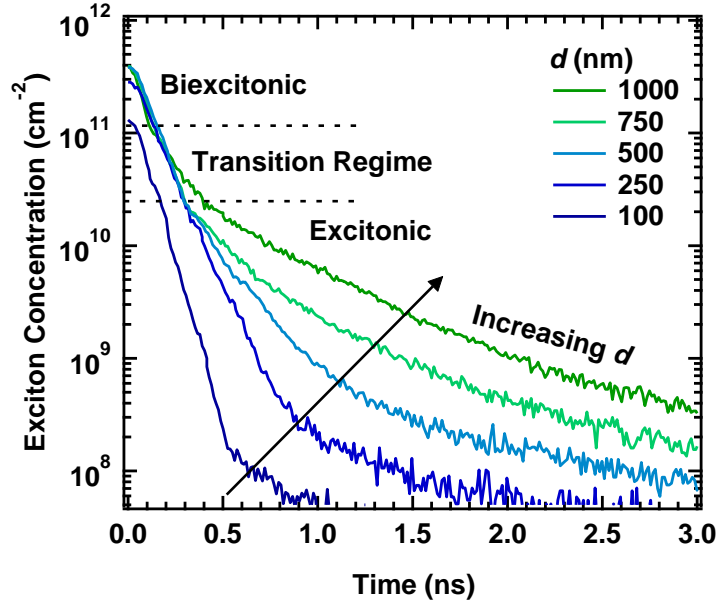
Figure 3.7. *Time resolved photoluminescence (TRPL) measurements of WS$_2$ disks. Two distinct decay regimes (with a visible transition) is observed for larger WS$_2$ disk sizes, while only one regime is seen for smaller sizes. Lifetime extraction is done at the lowest possible generated exciton density where mono-excitonic recombination mechanisms dominate and a clear size dependence is present.*

3.5 Edge Lifetime and its relation with diameter

Going forward, an important task is to establish a direct quantitative relation between τ_{edge} and disk diameter *d*. Starting with existing diffusion models[3], we provide here a detailed derivation of the edge recombination velocity expression:

$$\tau_{\text{edge}} = \frac{d}{4 \times \text{ERV}} \tag{1}$$

We assume that the carriers are governed by diffusive dynamics, with the diffusion coefficient D independent of the carrier concentration.

We also express distance in units of $d/2$, with d being the disk diameter. Time (and the relaxation time) is measured in units of $d^2/4D$. With these units, the dimensionless diffusion equation becomes (assuming cylindrical symmetry):

$$\frac{\delta C}{\delta t} = \frac{1}{r}\frac{\delta}{\delta r}\left(rD\frac{\delta C}{\delta r}\right) - \frac{C}{\tau} \tag{2}$$

With $C(r,t)$ being the carrier concentration, r the dimensionless radius, and τ the dimensionless relaxation time. The edge induced recombination rate is represented as a flux of carriers at the edge of the disk. In dimensionless form, this boundary condition is given by:

$$-D\left.\frac{\delta C}{\delta r}\right|_{r=1} = \alpha C|_{r=1} \tag{3}$$

With $\alpha = {d}/{2D} \times \mathrm{ERV}$, the dimensionless recombination velocity. The solution to this equation can be constructed in the form of a Dini series. Assuming that the initial condition is a uniform concentration of carriers, C_o, the solution is given by:

$$C(r,t) = C_o \sum_{n=1}^{\infty} \frac{2\alpha}{(k_m^2 + \alpha^2)} \frac{J_0(k_m r)}{J_0(k_m)} \exp[-(k_m^2 + {1}/{\tau})t] \tag{4}$$

With $J_v(x)$ being the Bessel function of the order v and k_m being the mth root of:

$$k_m J_1(k_m) = \alpha J_0(k_m) \tag{5}$$

This expression gives the complete solution to our problem.

The total light emitted at dimensionless time t is proportional to the total number of carriers:

$$\mathrm{intensity} \propto \frac{2\pi}{\tau_{\mathrm{rad}}} \int_0^1 dr\, r\, C(r,t) \tag{6}$$

With τ_{rad} being the relaxation time for radiative recombination. In the long-time limit, the intensity becomes proportional to:

$$\mathrm{intensity} \propto \exp[-(k_1^2 + {1}/{\tau})t] \tag{7}$$

The total dimensionless relaxation time becomes $(k_1^2 + {1}/{\tau})^{-1}$, with the corresponding edge relaxation time becoming k_1^2. Restoring dimensions, we find that

$$\tau_{\mathrm{edge}} = \frac{d}{4D} k_1^{-2} \tag{8}$$

For small α, the solution to (5) for k_1 can be approximated as $k_1 = \sqrt{2\alpha}$.[4] Substituting this expression into (S.8) and noting that $\alpha = {d}/{2D} \times \mathrm{ERV}$, we find:

$$\tau_{\mathrm{edge}} = \frac{d}{4D} k_1^{-2} = \frac{d}{4D} \frac{1}{2\alpha} = \frac{d}{4 \times \mathrm{ERV}} \tag{9}$$

The quality of the $k_1 = \sqrt{2\alpha}$ approximation can be assessed via Fig. 3.5 that plots both the exact solution for k_1 and its approximate expression for $0 < \alpha < 1$.
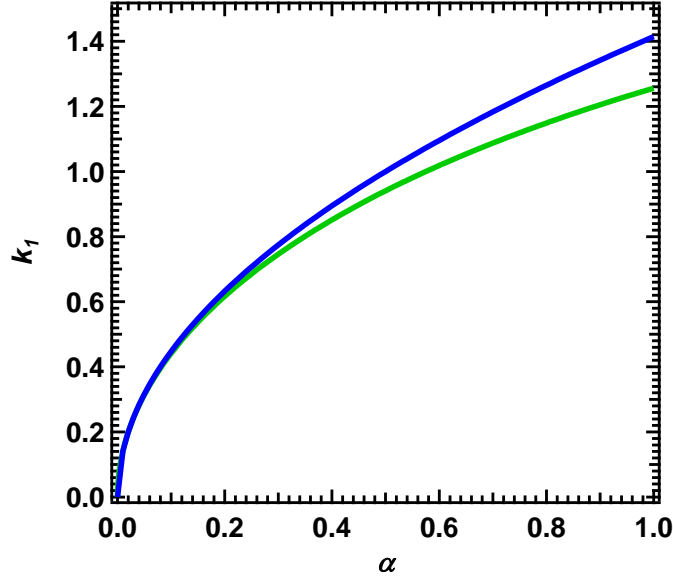
Fig. 3.8. *Graphical comparison for both the exact solution to (S.5) for k_1 (blue curve) and the approximation $k_1 = \sqrt{2\alpha}$ (black curve). The error at $\alpha = 1$ is approximately 13%.*

3.6 Edge Recombination Velocity (ERV)

Figure 3.9a plots $1/\tau_{\text{effective}}$ vs. $1/d$ across multiple disk samples using the previously fitted $\tau_{\text{effective}}$ values. The error bars indicate the standard deviation of all measured samples with the same designed d. To find the ERV, we first experimentally determine τ_{rad} and τ_{nrad} from an unetched WS$_2$ monolayer and collect them under a single time constant τ_{surface}:

$$\tau_{\text{surface}} = \left(\frac{1}{\tau_{\text{rad}}} + \frac{1}{\tau_{\text{nrad}}}\right)^{-1} = 1.37\,\text{ns} \qquad (10)$$

Subsequently, τ_{edge} is extracted from the measured $\tau_{\text{effective}}$ for each disk diameter. Using the diffusion model presented in Supporting Information, τ_{edge} and ERV are related by the following expression:

$$\tau_{\text{edge}} = \frac{d}{4 \times \text{ERV}} \qquad (11)$$

where ERV has units of length/time.

With equation (11), we fit the experimental $1/\tau_{\text{effective}}$ vs. $1/d$ curve with a linear slope of (4 x ERV), and find an ERV of ~4 ± 0.2 x 10^4 cm/s. Notably, the y-intercept of the fitted line also directly indicates the asymptotic value of $\tau_{\text{effective}}$ where $\tau_{\text{effective}}$ approaches τ_{surface} as d approaches infinity.

It is important to compare the steady-state PL iQY in Figure 3.4a against the lifetime measurements shown in Figure 3.7 to verify self-consistency between the two experiments. To this end, we directly compare the iQY values extracted from both

41

measurements. For the TRPL data in Figure 3.7, we find the time resolved extracted iQY via:

$$iQY = \frac{\tau_{\text{effective}}}{\tau_{\text{rad}}} \tag{12}$$

Figure 3.9b shows from the iQY comparison between quantities calculated from measured decay curves of TRPL (blue) and those directly extracted from steady state PL (green) at the low excitation regime. Both sets of iQY values show a similar trend of decay and are in good agreement. The error bars on the PL iQY curve represent the uncertainty in the absorption measurements, while the error bars on time resolved extracted iQY curve reflect the spread in the extracted $\tau_{\text{effective}}$ mentioned previously.
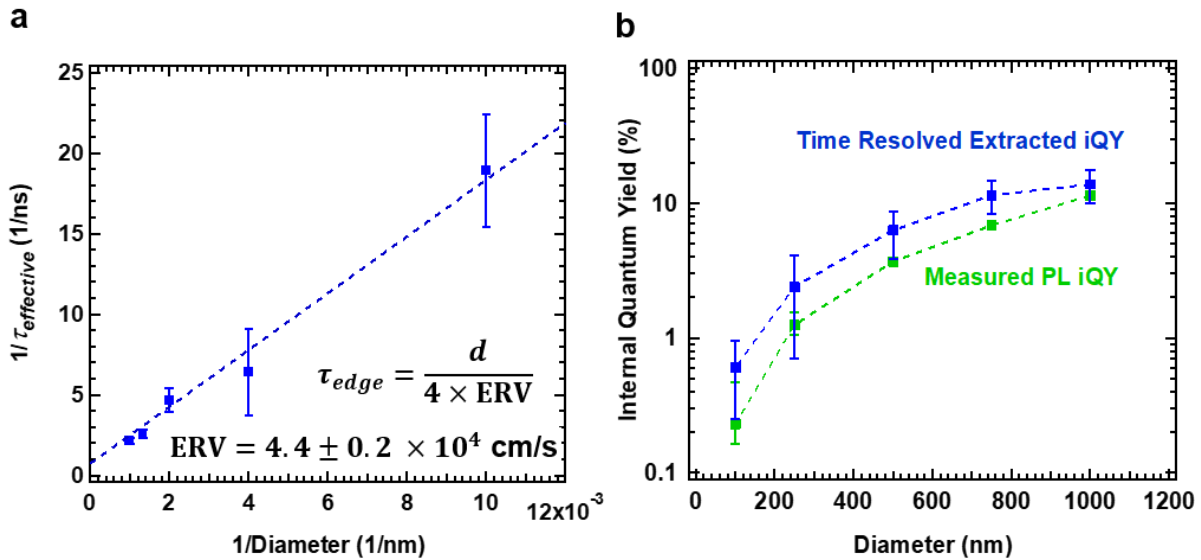
Figure 3.9. *(a) Reciprocal of effective lifetime measured by TRPL versus reciprocal of diameter. Error bars signify the standard deviation of multiple samples of the same designed diameter. (b) Extracted internal quantum yield from both steady-state PL (green) and TRPL (blue) measurements. Error bars on the steady-state PL iQY curve represent absorption error.*

3.6 ERV Significance

To understand ERV as a metric of non-radiative edge recombination in 2D semiconductors, we draw attention to a similar metric extensively utilized by the optoelectronics community, called surface recombination velocity (SRV). SRV is used for describing the surface quality of a 3D semiconductor by quantifying the non-radiative carrier recombination sites at the surface, and is a key figure of merit for projecting the maximum performance of the enabled optoelectronic devices based on a 3D semiconductor.[19] Generally, SRV can range from high quality passivated silicon surface of <1 cm/s to unpassivated silicon surfaces spamming into the 10^4 - 10^5 cm/s regimes.[20-22]

Similar to SRV and the critical role it plays in quantifying surface recombination, ERV can also serve as a key figure of merit for non-radiative carrier recombination at the edge of 2D materials. To see this, we define ERV as:

$$\text{ERV} = {N_t}/{l} \, \sigma_{1D} v_{\text{th}} \qquad (13)$$

where ${N_t}/{l}$ is a linear density of non-radiative recombination sites along a defined perimeter, σ_{1D} is the atomic capture radius of diffusing excitons, and v_{th} is the thermal velocity of excitons. Equation (8) follows from the general lifetime expression:

$$\frac{1}{\tau_{\text{edge}}} = \frac{N_t}{A} \sigma_{1D} v_{\text{th}} \qquad (14)$$

and making the appropriate substitution from equation (11) where ${N_t}/{A}$ is the areal density of non-radiative recombination sites.

Equation (13) allows us to calculate the density of non-radiative recombination sites at a 2D material edge. To illustrate this, we approximate the non-radiative edge recombination sites density ${N_t}/{l}$ on our measured WS$_2$ system using a capture radius on the order of the atomic radius $\sigma_{1D} \sim 10^{-8}$ cm, and an exciton thermal velocity $v_{\text{th}} \sim 10^5$ cm/s.[23, 24] The v_{th} value is estimated using experimentally measured diffusion length of excitons in transition metal dichalcogenides (10^{-4} to 10^{-5} cm) divided by the measured lifetime ($\sim$1 ns).[25, 26] The value used also falls within the range of reported exciton v_{th} from inorganic materials such as GaAs/AlGaAs quantum wells and thin silicon (10^6 to 10^7 cm/s) to organic molecules such as Anthracene (10^4 cm/s).[27-30] With our measured ERV we calculate ${N_t}/{l} \approx 4.4 \times 10^7$ cm^{-1}, corresponding to a non-radiative recombination site per $\sim$2Å edge length. The estimated density hints at non-radiative recombination at nearly every edge atom, underlying the need for better passivation schemes in the future. This is expected given that certain edge orientations are calculated to exhibit metallic behavior.[13]

3.7 Conclusion

In summary, a simple direct optical characterization method enables the experimental measurement of ERV, a quantitative metric directly related to the optical quality of the edge of 2D materials. Using WS$_2$ as a model material system, we measure ERV of 4×10^4 cm/s for Cl-plasma etched edges. The approach can be extended to other optically active 2D semiconductors. In the future, ERV can be used as an edge quality metric to explore the effectiveness of different edge passivation schemes.

The realization of the aforementioned characterization technique, along with the quantitative recombination metric, serves as a step towards standardizing edge characterization in the community as the possible edge structures remain as varied as the possible number of synthesis method. With quantitative metric, we can now proceed

to investigate further edge passivation methods, along with expanding the ERV characterization towards other members of the TMD family to identify new potentials for laterally confined TMDs.

REFERENCES:

1.   Li, Y.; Zhou, Z.; Zhang, S.; Chen, Z. *J. Am. Chem. Soc.* **2008,** 130, (49), 16739-16744.
2.   Davelou, D.; Kopidakis, G.; Kaxiras, E.; Remediakis, I. N. *Phys. Rev. B* **2017,** 96, (16), 165436.
3.   Chen, Y.; Cui, P.; Ren, X.; Zhang, C.; Jin, C.; Zhang, Z.; Shih, C.-K. *Nat. Commun.* **2017,** 8, 15135.
4.   Kim, M. S.; Yun, S. J.; Lee, Y.; Seo, C.; Han, G. H.; Kim, K. K.; Lee, Y. H.; Kim, J. *ACS Nano* **2016,** 10, (2), 2399-2405.
5.   Gutiérrez, H. R.; Perea-López, N.; Elías, A. L.; Berkdemir, A.; Wang, B.; Lv, R.; López-Urías, F.; Crespi, V. H.; Terrones, H.; Terrones, M. *Nano Lett.* **2013,** 13, (8), 3447-3454.
6.   Lin, T.; Kang, B.; Jeon, M.; Huffman, C.; Jeon, J.; Lee, S.; Han, W.; Lee, J.; Lee, S.; Yeom, G.; Kim, K. *ACS Appl. Mater. Interfaces* **2015,** 7, (29), 15892-15897.
7.   Fox, D. S.; Zhou, Y.; Maguire, P.; O'Neill, A.; Ó'Coileáin, C.; Gatensby, R.; Glushenkov, A. M.; Tao, T.; Duesberg, G. S.; Shvets, I. V.; Abid, M.; Abid, M.; Wu, H.-C.; Chen, Y.; Coleman, J. N.; Donegan, J. F.; Zhang, H. *Nano Lett.* **2015,** 15, (8), 5307-5313.
8.   Huang, Y.; Wu, J.; Xu, X.; Ho, Y.; Ni, G.; Zou, Q.; Koon, G. K. W.; Zhao, W.; Castro Neto, A. H.; Eda, G.; Shen, C.; Özyilmaz, B. *Nano Research* **2013,** 6, (3), 200-207.
9.   Liu, X.; Xu, T.; Wu, X.; Zhang, Z.; Yu, J.; Qiu, H.; Hong, J.-H.; Jin, C.-H.; Li, J.-X.; Wang, X.-R.; Sun, L.-T.; Guo, W. *Nat. Commun.* **2013,** 4, 1776.
10.   Zhao, P.; Amani, M.; Lien, D.-H.; Ahn, G. H.; Kiriya, D.; Mastandrea, J. P.; Ager, J. W.; Yablonovitch, E.; Chrzan, D. C.; Javey, A. *Nano Lett.* **2017,** 17, (9), 5356-5360.
11.   Chen, Q.; Li, H.; Xu, W.; Wang, S.; Sawada, H.; Allen, C. S.; Kirkland, A. I.; Grossman, J. C.; Warner, J. H. *Nano Lett.* **2017,** 17, (9), 5502-5507.
12.   Bao, W.; Borys, N. J.; Ko, C.; Suh, J.; Fan, W.; Thron, A.; Zhang, Y.; Buyanin, A.; Zhang, J.; Cabrini, S.; Ashby, P. D.; Weber-Bargioni, A.; Tongay, S.; Aloni, S.; Ogletree, D. F.; Wu, J.; Salmeron, M. B.; Schuck, P. J. *Nat. Commun.* **2015,** 6, 7993.
13.   Huo, N.; Li, Y.; Kang, J.; Li, R.; Xia, Q.; Li, J. *Appl. Phys. Lett.* **2014,** 104, (20), 202406.
14.   Amani, M.; Lien, D.-H.; Kiriya, D.; Xiao, J.; Azcatl, A.; Noh, J.; Madhvapathy, S. R.; Addou, R.; Kc, S.; Dubey, M.; Cho, K.; Wallace, R. M.; Lee, S.-C.; He, J.-H.; Ager, J. W.; Zhang, X.; Yablonovitch, E.; Javey, A. *Science* **2015,** 350, (6264), 1065.
15.   Tongay, S.; Suh, J.; Ataca, C.; Fan, W.; Luce, A.; Kang, J. S.; Liu, J.; Ko, C.; Raghunathanan, R.; Zhou, J.; Ogletree, F.; Li, J.; Grossman, J. C.; Wu, J. *Sci. Rep.* **2013,** 3, 2657.
16.   Amani, M.; Taheri, P.; Addou, R.; Ahn, G. H.; Kiriya, D.; Lien, D.-H.; Ager, J. W.; Wallace, R. M.; Javey, A. *Nano Lett.* **2016,** 16, (4), 2786-2791.
17.   Ivan Pelant, J. V., *Luminescence Spectroscopy of Semiconductors*. Oxford University Press: New York, 2012; p 542.
18.   Preus, S. *DecayFit - Fluorescence Decay Analysis Software*, 1.4; FluorTools: 2014.
19.   Shockley, W., *Electrons and Holes in Semiconductors with Applications to Transistor Electronics*. D. Van Nostrand Company, Inc: Princeton, New York, 1950; p 576.
20.   Wolford, D. J.; Gilliland, G. D.; Kuech, T. F.; Smith, L. M.; Martinsen, J.; Bradley, J. A.; Tsang, C. F.; Venkatasubramanian, R.; Ghandi, S. K.; Hjalmarson, H. P. *J. Vac. Sci. Technol., B* **1991,** 9, (4), 2369-2376.
21.   Baek, D.; Rouvimov, S.; Kim, B.; Jo, T.-C.; Schroder, D. K. *Appl. Phys. Lett.* **2005,** 86, (11), 112110.
22.   Yablonovitch, E.; Allara, D. L.; Chang, C. C.; Gmitter, T.; Bright, T. B. *Phys. Rev. Lett.* **1986,** 57, (2), 249-252.
23.   Nakamura, M.; Suzuki, T.; Fujita, M. *Phys. Rev. B* **1987,** 35, (6), 2854-2862.
24.   Schramm, G. *Phys. Status Solidi A* **1991,** 125, (2), K113-K116.
25.   Kato, T.; Kaneko, T. *ACS Nano* **2016,** 10, (10), 9687-9694.
26.   Kumar, N.; He, J.; He, D.; Wang, Y.; Zhao, H. *J. Appl. Phys.* **2013,** 113, (13), 133702.
27.   C. I. Harris, B. M., Ro. Holtz, H. Kalt, J. L. Mert. *J. Phys. IV* **1993**

03 (C5), C5-171-C5-174.

28.   Tamor, M. A.; Wolfe, J. P. *Phys. Rev. Lett.* **1980,** 44, (25), 1703-1706.

29.   Avakian, P.; Merrifield, R. E. *Mol. Cryst.* **1968,** 5, (1), 37-77.

30.   Levinson, J.; Weisz, S. Z.; Cobas, A.; Rolón, A. *J. Chem. Phys.* **1970,** 52, (5), 2794-2795.

Chapter 4 Scanning Probe Lithography and Extension of ERV Characterization

4.1 Scanning Probe Lithography

The previous chapter introduced an important metric for edge defect characterization and elucidated the need for less defective edges toward future applications of TMDs in the lateral nanoscale regime. The WS_2 ERV work utilized a chlorine plasma towards etching, and various forms of passivation were applied in an effort to reduce the ERV post etching. However, the myriad of techniques attempted did not yield any significant improvement to either the ERV or PL as indicated below:

Wet Treatments	PL Peak Intensity Change in 100nm WS_2 Disk Arrays
Bis (trifluoromethane) sulfonimide (TFSI) Solvent: Dichloroethane (2mg/ml)	~ 2-3x enhancement
Triethyloxonium Hexachloroantimonate: Solvent: Chlorobenzene (0.1M)	< 2x change
Sulfuric Acid (1M)	< 2x change
Hydrochloric Acid (>1M)	< 2x change
Hydrofluoric Acid (10:1)	~ 3x reduction and observed defect peak
Ammonium Sulfide (20% in water) Solvent: H_2O (0.2g/15ml)	~ 2x reduction
Gas Annealing	
Forming Gas (300 ºC)	< 2x reduction and large peak broadening
O_2 Plasma (40W for 5 seconds)	< 2x reduction
Ambient Oxygen Anneal (250 ºC)	< 2x change
Physical Depositions	
Al_2O_3 (70 cycles at 250 ºC) – ALD	< 2x change
ZrO_3 (70 cycles at 200 ºC) – ALD	>3x reduction
SiO_2 (10nm) – eBeam Evaporation	< 2x change
WO_3 (2 cycles at 350 ºC) – ALD	~ 2x reduction and large peak broadening

***Table 4.1**: List of treatment applied to WS_2 post the chlorine plasma etch and their respective effects towards steady state PL emission. All samples here are etched into the 100nm diameter.*

Of the techniques listed above, some attempted at direct passivation after dry etch. Others methods (such as forming gas anneal) were aimed at first opening up the chemically reactive sites by removal of carbon-based resists and unwanted sidewall depositions, followed by passivation. Recalling a previous top down approach towards "ideal edge" realization, and knowing the limitations of a plasma dry etch, we realized that perhaps the path towards lower ERV is to change the patterning method rather than

finding an appropriate patterning method after the fact. A strong candidate for this top down patterning technique is scanning probe lithography (SPL).

SPL possesses a two-fold advantage in top down patterning in regards to edge passivation: 1) the method requires no resist, and therefore will not introduce excessive polymer residue during the patterning process. 2) The method can yield nanometer spatial resolution (dependent on the specific tip radius). More generally, SPL has been utilized extensively in many different material systems and are roughly separated into 3 different categories underlining the difference in the patterning mechanism: mechanical, thermal, and electrochemical.[1-4]

Mechanical SPL involves the utilization of an AFM to directly fabricate new patterns on a substrate. The reproducibility of patterning is directly based on the longevity of the tip used, and generally only simple patterns can be created due to the mechanical motion that can easily affect regions of material outside of the area directly meant for modification. In addition, repetitive runs will yield residue tip deposition and interfere with the tip profile depending on the surface hardness and tip robustness.

Thermal SPL (t-SPL) has been able to achieve the most complex patterns. By integrating a resistive heating element onto the cantilever, precise control of the local temperature can be made by the application of a bias onto the tip. By varying the temperature on the surface of interest, both lateral but also vertical control of the etching profile can be made, leading to patterns utilizing depth variation as shading. The result is the re-creation of the Mono Lisa (Figure 4.1 a and b) on polymer or other soft material surfaces.[2]
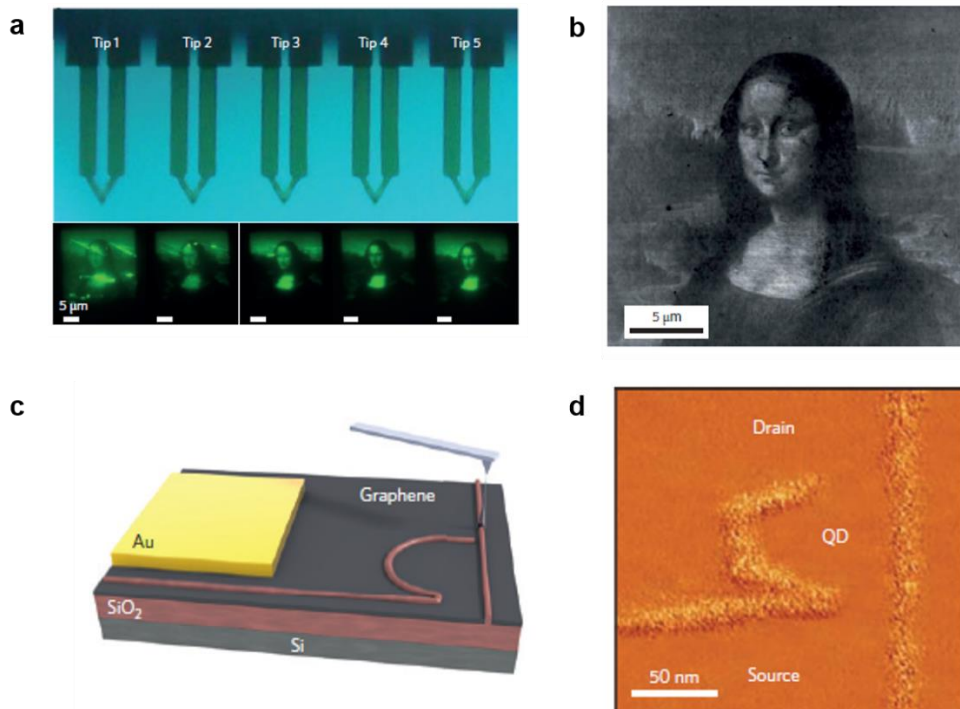
Figure 4.1. Examples of scanning probe lithography in action. a). A series of t-SPL probes aligned with the corresponding fluorescence of Mono Lisa pattern converting a precursor film into poly-p-phenylene vinylene (PPV). b) AFM topology of a specific t-SPL Mono Lisa pattern. c). Oxidation induced via the electrochemical reaction of scanning probe lithography on graphene. Schematic shows the process of tip writing. d). AFM topology of oxidized graphene.

For 2D materials, electrochemical SPL is the most suited method. Electrochemical approach has the advantage of not significantly wearing out the mechanical properties of the tip, while also not requiring detailed modifications of the tip or cantilever for heater integration. Various work has also been done on silicon and graphene (Figure 4.1 c and d), along with elucidating work showing the effects of humidity, voltage applied, time dwell time, and effects of native oxide, along a host of other controlling factors. By varying such levers of control, lines down to 10nm thickness can be realized on silicon.[4, 5]

More recently, electrochemical SPL has been applied to 2D material with demonstrable success. Both MoS_2 and WSe_2 has been oxidized, with oxides that are later etchable in water.[6, 7] Limited utilization of SPL on 2D materials have also been demonstrated. In the MoS_2 work, narrow conduction channels were created via oxidation confinement (after contact deposition) to backgated MoS_2 devices. However, much more work is needed in order to completely characterize the narrow channel device behavior, as regions near the contact are not patterned at all, leading to obvious leakage path. The following presents the electrochemical application of SPL on MoS_2, $MoSe_2$, and WSe_2, and various applications SPL can be used, both in expansion of ERV characterization but also optical applications in general.

4.2 Edge Passivation via SPL

Scanning probe lithography (SPL) has been utilized to pattern TMDs of differing thickness.[6,7] In this chapter, we expand this patterning platform to monolayer MoS_2, $MoSe_2$, WS_2, and WSe_2 on SiO_2/Si substrates while investigating the various parameters that can affect the oxidation process. These parameters include tip bias, dwell time, humidity, and setpoint amplitude. By fine tuning these parameters, we demonstrate a SPL oxidation resolution at <100nm and thickness dependent oxidation of thicker TMDs by varying tip dwell time. In addition, we extract ERVs of four TMD members (MoS_2, $MoSe_2$, WS_2 and WSe_2) patterned via SPL oxidation and water submersion removal. The variations in the observed ERVs highlight SPL as a tool to reveal material dependent edge defects while expanding the ERV characterization platform.

Figure 4.2 a) - b) illustrate the SPL process on monolayer TMDs via atomic force microscope (AFM). During lithography, a diamond-like-carbon (DLC) coated silicon tip (Bruker, DDESP V2) is brought close to the surface (with an amplitude setpoint of ~0.6nm) while a voltage is applied across from the tip (V_{tip} = -12V) to the substrate (V_{sub} = 10V). In addition, the AFM chamber is maintained at ~35-40% humidity. After oxidation, the entire

flake is submerged in DI water, where the oxidized region is selectively removed while leaving the rest of the flake intact. Figure 4.2 c) shows a MoS$_2$ monolayer patterned into grids of three different sizes – 1µm, 500nm and 250nm respectively – using SPL.
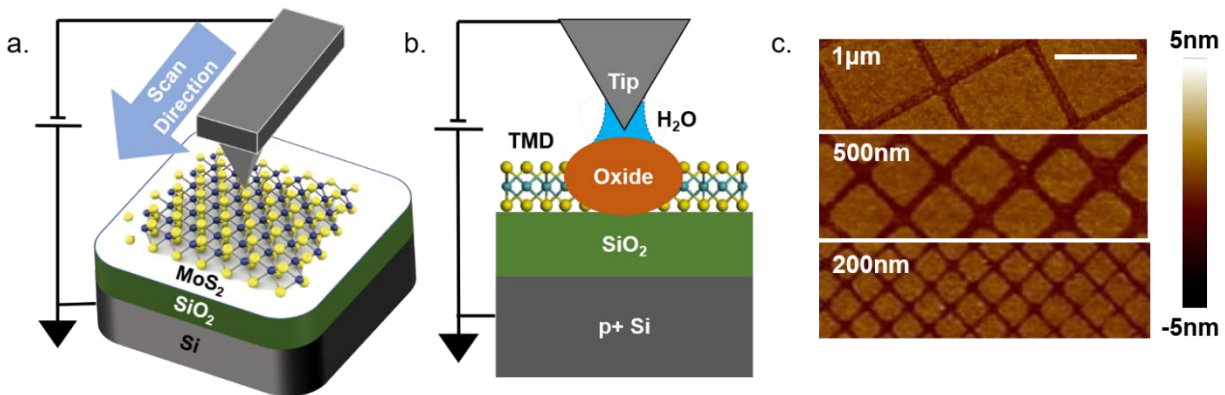

Figure 4.2 *a). A representative schematic of the oxidation is illustrated. B). The sideview illustration details the specific components relevant to oxidation. The AFM tip scans across the flake during oxidation while a bias is applied between the tip to the AFM chuck. A water bridge is also induced during the writing process C). Grid patterns of MoS$_2$ realized after water removal of the MoOx patterned area. Scale bar represents 500nm.*

SPL lithography consists of two parts – oxidation and oxide removal via water. To enable oxidation, a water bridge formation between the AFM tip and the TMD surface has to happen first. After the bridge formation, the available water and electric field will increase an already favorable oxidation process, speeding up the general reaction as follows: [6, 8-10]

$$MX_2 + x\,H_2O \leftrightarrow MO_x + y\,H_2 + XO_y \qquad (1)$$
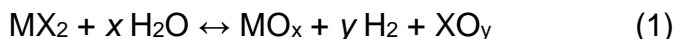
where M stands for the transition metal of interest, and X the chalcogen of interest. x and y also take on different values dependent on the specific TMD in question. After successful oxidation, the sub-stochiometric transition metal oxides can be removed via water (MoO$_x$ and WO$_x$) as reported elsewhere.[6, 11]

4.1.1. Highspeed Data Capture of AFM Tip Sensor

During SPL, movement of the tip is measured to ensure reliable and predictable operation. The AFM used included highspeed data capture channels that allowed observation of the AFM sensor during writing. Figure 4.3. a) shows the oscillation amplitude of the tip, where during writing the amplitude becomes small due to close proximity with the surface, and large distance otherwise when moving from pixel to pixel. Similarly, Figure 4.3 b) shows the tip height sensor moving from one pixel to the next, breaking the water bridge between movements as one pixel is written and moving on to another.
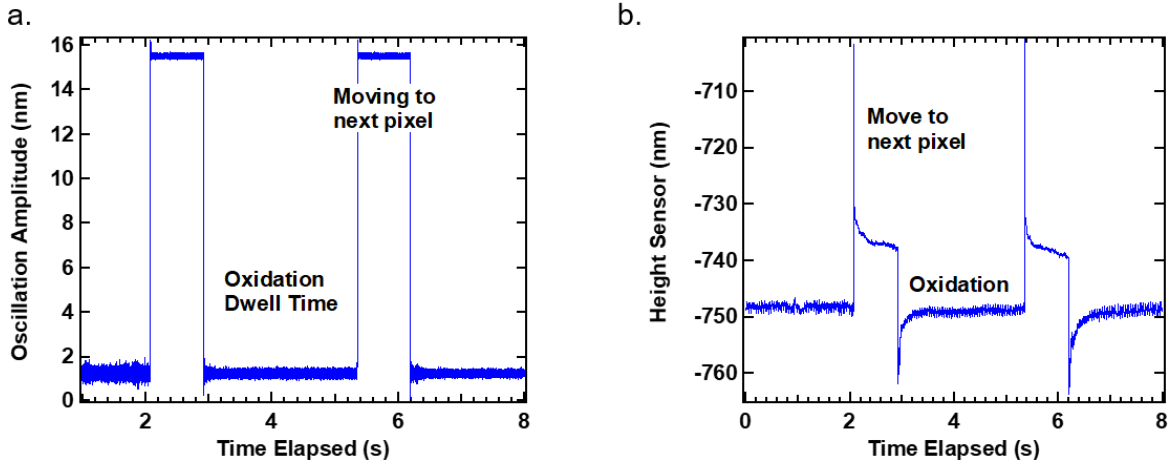
Figure 4.3. *Highspeed Data Capture of AFM sensors during the SPL process. a).
Oscillation amplitude for the AFM tip - very little oscillation happens during the writing
process due to the proximity of the tip with the sample surface (pixel took ~1 second for
adequate oxidation in this example), while the tip oscillates as usual when moving from
one pixel to another. b). Tip height during a write sequence. The tip generally remains
~15nm away from the surface when moving from pixel to pixel, while stays very close to
the surface during the actual oxidation process.*

4.3 SPL Parameter Dependence

To elucidate the oxidation mechanism, we first focus on the appropriate conditions
when a water bridge formation is favorable. After water bridge formation, the resultant
oxidation area is directly related to the size of the water bridge coverage over the TMD
surface. While the details of the water bridge formation is described elsewhere,[12] we
qualitatively relate the key experimental parameters with the known model to establish
consistency.

Generally, water bridge formation is favorable when the following energy relation
is satisfied:

$$\Delta U = U \text{ (water bridge)} - U_o \text{ (vapor)} = \Delta U_s + \Delta U_c + \Delta U_{vdW} + \Delta U_e < 0 \quad (2)$$
$$\text{where } \Delta U_e \left(V_{tip} \right), \Delta U_c \left(RH \right), \Delta U_{vdW} \left(V_{setpoint} \right) \quad (3)$$

The potential energy difference, ΔU, shows a competitive process between water
condensation and water vapor formation. To determine whether a bridge forms, the
surface energy (U_s), condensation energy (U_c), vdW energy (U_{vdW}), and electrostatic
energy (U_e) of the system is summed together. When $\Delta U = U$ (condensation) $- U_o$ (vapor)
< 0, the bridge forms. As ΔU becomes more negative (or more favorable for water bridge
formation), the water bridge also increases in width, resulting in a larger TMD surface
coverage and oxidation area. We expect increasing tip bias V_{tip} (increasing ΔU_e),

50

decreasing tip to surface distance (increasing ΔU_{vdW}) and increasing humidity (decreasing ΔU_c) to all contribute to a more stable, and wider water bridge formation.

The previously mentioned parameters are investigated and their effects shown in Figure 4.4. Figure 4.4 a) shows the impact of tip bias V_{tip} on the oxidation process. When V_{tip} changes from -12V to -2V, the oxidized area becomes smaller, implying a smaller water bridge as V_{tip} approaches 0V. This conforms to our expectation as V_{tip} affects the water bridge formation via:

$$U_e = \frac{\varepsilon_o}{2} \int \varepsilon \mathbf{E}\, d\vec{r} \qquad (4)$$

Here ε_o is the permittivity of air, $\mathbf{E}$ is the electric field immediately before condensation, and ε permittivity of the relevant liquid (water). It can been seen that at a smaller V_{bias}, the electric field $\mathbf{E}$ between the tip and TMD surface will be smaller, leading to a smaller U_e. From equation (2) we see that a smaller ΔU_e (when a tip bias is applied vs. when a tip bias is not applied minimizes $|\Delta U|$, correlated to a smaller water bridge formation and consistent with Figure 4.4 a).
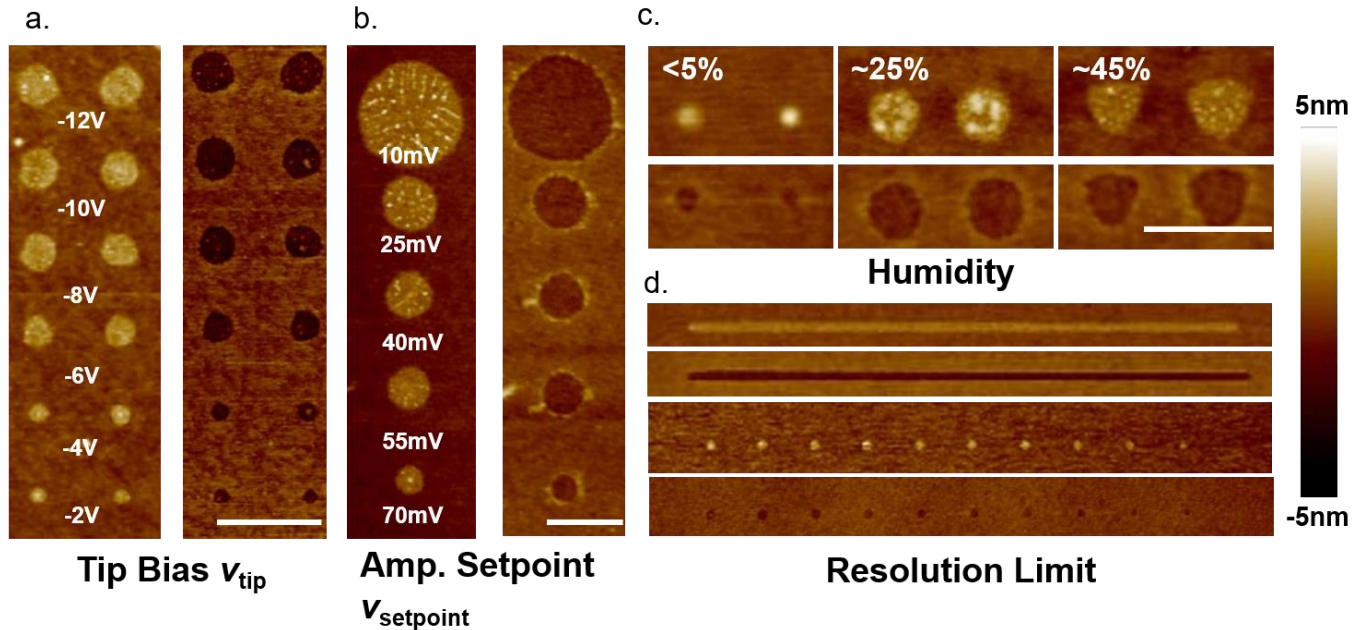
Figure 4.4. *Effects on oxidation via parameter variation. a). Tip voltage bias variation; higher tip voltage corresponds to larger area oxidation at a fixed tip diameter. b). Amplitude setpoint variation; the closer the tip approaches the surface, the larger the oxidized spot at a fixed tip diameter. c). Humidity variation; adequate size of oxidized TMD requires a high enough humidity, where above the threshold no significant variation in oxidation exists. d). Finest resolution limit achievable via SPL, showing both dots and lines at <100nm resolution respectively. Scale bars are 500nm.*

Subsequently, the impact of amplitude setpoint, $V_{setpoint}$, on oxidation is investigated. $V_{setpoint}$ is the feedback parameter AFM attempts to maintain during tapping mode and SPL. The voltage value refers to the tip amplitude oscillation at a predetermined drive amplitude of the piezo, by either decreasing or increasing the net distance of the tip and the TMD surface. The value in mV is directly related to the oscillation amplitude where 10mV = 0.626 nm. The vdW force between water molecules can be described via the following the energetic relation:

$$U_{vdw} = \frac{H}{12\pi} \int \frac{1}{\xi^2} ds \qquad (5)$$

where H is the Hamaker constant, ξ being a constant related to the shape of the water bridge (and can be approximated as the distance between the top and bottom layers of the water molecules). We see in equation (5) that the tip-surface distance enters into the vdW energy calculation via ξ, where a larger separation translates to a smaller U_{vdW} and vice versa. Therefore, we expect that a lower setpoint during lithography will lead to a larger oxidized area (due to a more stable and larger water bridge) while a higher setpoint leads to a smaller oxidized area. Figure 4.4 b) confirms this expectation as we change the tip-to-surface distance from 0.63nm to 4.4nm.

Lastly, relative humidity, RH, is defined as the ratio between water vapor concentration in the air normalized to the saturation concentration of vapor in the air. RH influences the oxidation process by controlling the condensation energy (U_c) where the following relation applies:

$$U_c = \frac{R_g T}{V_m} \ln(\frac{1}{\text{RH}}) \int d\vec{s} \qquad (6)$$

where R_g is the gas constant, T is the temperature, and v_m is the molar volume of liquid.

From equation (6), we expect very limited oxidation (and very small water bridge formation) at lower humidity. Lower RH translates into a higher U_c, implying difficulty in liquid condensation and easier vapor formation. Qualitatively, lower RH means a dryer environment, which drives water vapor formation over condensation. As U_c increases, ΔU from equation (2) becomes more positive, translating to a smaller water bridge coverage. Conversely, water bridge width should increase at higher RH, leading to an increased oxidation area. Interestingly, further increase in RH should result in a slower increase of the oxidation area to the natural log function. Figure 4.4 c substantiates our hypothesis and demonstrates a significant difference in the oxidation area as RH changes from <5% to 25%, whereas the oxidation size increase between 25% and 45% is significantly reduced.

After examining the mechanism behind water bridge formation, we discuss the oxidation process itself. Strictly speaking, V_{tip} can be either positive or negative (with respect to the TMD surface) for a successful water bridge formation.[12] However, negative V_{tip} is needed to induce the oxidation reaction. While some TMDs (MoS_2, $MoSe_2$, WS_2, and WSe_2 being the relevant TMD members) spontaneously oxidize under ambient conditions (at a very slow rate),[8, 9] we postulate that the negative tip bias supplies a large amount of OH^- from the water bridge to the TMD surface, speeding up the general reaction detailed in equation (1).

Finally, by optimizing the various parameters discussed above, we demonstrate the smallest dimension of dots and lines achievable via SPL in Figure 4.4 d). Both the line width and the dot diameters are < 100nm. The condition is set at V_{tip} = -2V (with a substrate bias of 10V), $V_{setpoint}$ = 30mV, and RH ~ 35%. Any further efforts at pushing ΔU closer to 0 lead to inconsistencies in the patterning. Smaller dimension has been reported via SPL on TMDs elsewhere, and we attribute other factors (such as tip radius or tip type, affecting surface energies ΔU_s) to also play a role in reaching the highest resolution possible.[6]

4.4 Thickness Dependent SPL

In tuning various SPL parameters for oxidation, we find an interesting effect of oxidation dwell time t_{dwell} in relation to multilayer TMDs. While the impact of t_{dwell} is not explicitly included in equation (2), we postulate a longer t_{dwell} will give more time for oxidation to complete at some specific water bridge coverage. While the impact of t_{dwell} is lessened for monolayer TMDs (due to the small amount of TMD that needs to be oxidized), thicker TMDs will need more time for complete oxidation. Therefore, we postulate a thickness dependence oxidation as t_{dwell} increases. Figure 4.5 shows a time dependence of the oxidation process for both monolayers and multilayer TMDs.
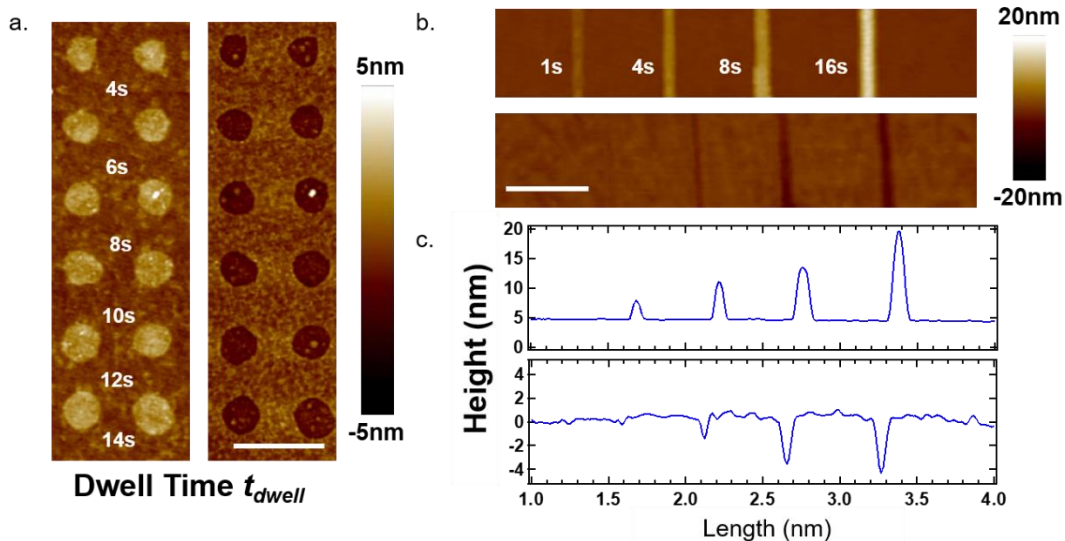
Figure 4.5. Dwell time effects on oxidation of both monolayer and multilayer TMDs. a). Dwell time variation on monolayer oxidation. After an initial increase of oxidation size due to dwell time increase (4 – 6 seconds), further increase of the dwell time can no longer further increase the oxidation area. b). Dwell time effect on thick TMDs. Increasing dwell time can increase the oxidation thickness. 4 different τ_{dwell}'s are used on a TMD multilayer, where each successive increase shows a thicker oxidation and deeper water removal. c) AFM topology of the TMD surface presented in b) after oxidation and water removal respectively. Scale bars are 500nm.

For monolayers, t_{dwell} starts having negligible effects on the oxidation pattern after a slight increase in oxidized area going from 4-6 seconds. This is most likely because monolayer oxidation completes quickly (~ 4 seconds). Figure 4.5 b) shows the same dwell time variation applied to thicker TMD layers. Here, a clear depth dependence is seen when t_{dwell} increases. Similar to SPL oxidation of silicon[4, 5], deeper layers of TMDs are oxidized at longer t_{dwell}, resulting in thicker oxides accompanied by a deeper trench after water submersion shown in Figure 4.5 c). Interestingly, this oxidation depth dependence on t_{dwell} also highlights the potential of SPL used towards controllable layer-by-layer oxidation of thicker TMDs for various applications.

4.5 SPL on MoS$_2$ with Superacid Treatment

Compared to the more commonly used lithography techniques (such as photo- or e-beam lithography combined with wet or dry etching), SPL (combined with water removal) can avoid many nonidealities such as resist residues, electron backscattering effects, and various etching-related contaminations.[13, 14] Therefore, we use SPL to pattern monolayer MoS$_2$, MoSe$_2$, WS$_2$, and WSe$_2$ TMDs in the same fashion shown in Figure 4.3 c), and measure their respective ERVs to assess their edge qualities.

Shortly, all four TMDs are patterned down into square arrays with three different length l (1μm, 500nm and 250nm). As l decreases, the increased circumference to surface area ratio means a higher contribution of the edge recombination effects, resulting in lower photoluminescence (PL) intensity after fill factor correction (Figure 4.9). Utilizing time-resolved PL (TRPL) for lifetime measurements, we identify the lower carrier concentration regime (at ~10^{-1} W/cm^2 power density for all four TMDs) to extract the relevant effective lifetimes.[15, 16] The effective lifetime ($\tau_{effective}$) is broken down into a surface lifetime ($\tau_{surface}$) and an edge lifetime (τ_{edge}):

$$\frac{1}{\tau_{effective}} = \frac{1}{\tau_{surface}} + \frac{1}{\tau_{edge}} \tag{7}$$

The surface lifetimes are measured on unetched monolayers as 1.5, 10.9, 1.18, and 0.9 ns for MoS$_2$, MoSe$_2$, WS$_2$, and WSe$_2$ respectively. τ_{edge} is then extracted and

correlated to ERV via equation (8). Due to the square cross sections of the flake, the ERV derivation changes slightly[17] with details discussed in section 4.5.1:

$$\tau_{edge} = \frac{l}{2 \times \text{ERV}}$$

(8)

Extraction of MoS_2 ERV can prove particularly challenging. Figure 4.6 a) shows the TRPL of MoS_2 for various sizes, including an unetched monolayer control. In addition to the lifetime being close to the instrument response function (which is remedied by employing iterative re-convolution), the unetched control $\tau_{effective}$ is very close to that of the etched samples of all three sizes. This introduce a very large error in τ_{edge} extraction using equation (7). A more accurate extraction of τ_{edge} therefore ideally requires that $\tau_{surface} \gg \tau_{effective}$, or where length dependence is clearly observed from the TRPL series.
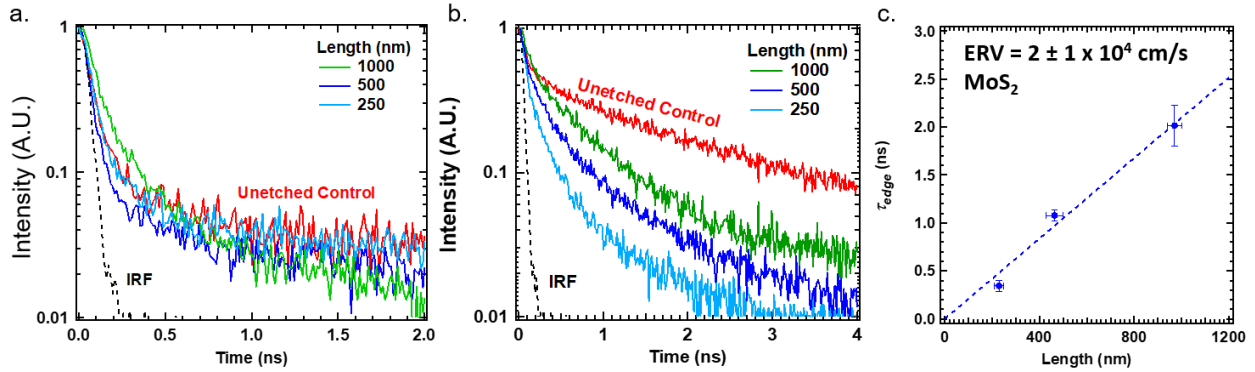

Figure 4.6. *Edge Recombination Velocity (ERV) extraction of MoS2 before and after superacid treatment. a). Time resolved photoluminescence (TRPL) of MoS2 squares of varying length with 250nm, 500nm and 1mm, including an unetched control before TFSI treatment b). TRPL of MoS2 grids after TFSI treatment, edge dependence can now be clearly extracted. c). tedge vs. l of MoS2, with an ERV ~ 2 x 10⁴ cm/s.*

By employing a previously known passivation scheme, MoS_2 $\tau_{surface}$ can be improved with bis(trifluoromethane) sulfonimide (TFSI)[15], satisfying $\tau_{surface} \gg \tau_{effective}$ and thereby elucidating the edge recombination mechanisms. Figure 4.6 b) shows the sample after TFSI treatment, where the edge dependence becomes clear for extraction, with the corresponding ERV shown in Figure 4.6 c).

4.5.1 ERV Derivation for Square Cross Sections

The methodology to finding the τ_{edge} vs. ERV is the same as in our previous work, and the process with the appropriate square boundary condition is detailed elsewhere (Shockley's recombination velocity derivation using a germanium filament).[17, 18] Shortly, we confirm the approximation of our τ_{edge} vs. ERV expression with the analytical model and check for percentage error. Accordingly, the exact expression for edge lifetime in relation to the recombination velocity is:

$$\frac{1}{\tau_{edge}} = 2D\left(\frac{\eta_o}{l}\right)^2 \tag{9}$$

$$\chi = \eta_o \tan(\eta_o) = \frac{ERV * l}{D} \tag{10}$$

As shown above, D is the exciton diffusion coefficient, η_o is the smallest solution to equation (10) (yielding the longest lifetime), and χ is a collective term for calculation. Equation (10) originates from applying the boundary condition of recombination velocity to all 4 edges assuming uniform carrier distribution at $t = 0$. Equation (9) goes to equation (8) as

$$\eta_o \tan(\eta_o) \rightarrow \eta_o{}^2 \tag{11}$$

Assuming a $D \sim 20$ cm^2/s and upper limit of $l = 1\mu$m, at an ERV ~ 5 x 10^4 cm/s, the error between the two approximation is 8.5%.[19] At lower ERVs, the error decreases and equation (8) becomes a more accurate τ_{edge} vs ERV relation.
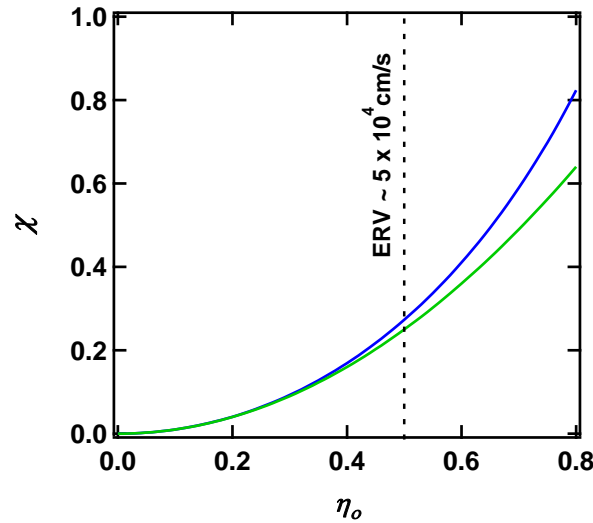

Figure 4.7. *Graphic representation of deviation error. x-axis represents either $\eta_o{}^2$ (green) or $\eta_o \tan(\eta_o)$ (blue). At ERV = 5 x 10^4 cm/s, the error resulting from the approximation is ~ 8.7%. Smaller ERVs will only result in smaller error, reinforcing the validity of our approximation.*
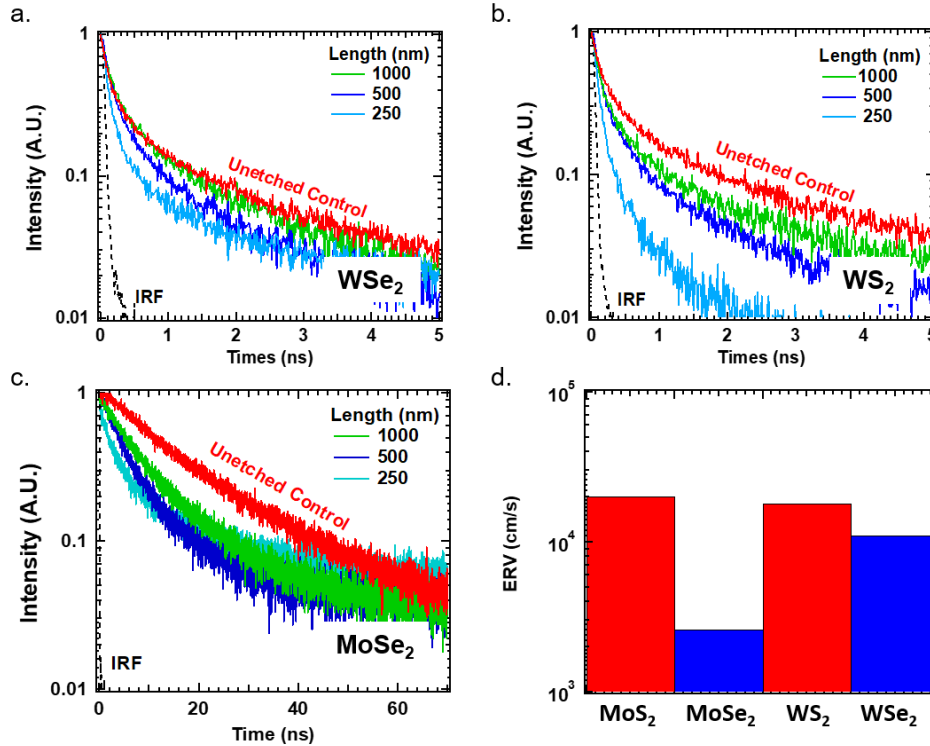
4.6 ERV on MoSe₂, WS₂, WSe₂ enabled via SPL

Figure 4.8. *Edge Recombination Velocity (ERV) extraction of WSe2, WS2 and MoSe2 are shown respectively from a) to c). d). Compiled data of ERV for all four relevant TMDs. Selenium based compounds are observed to have relatively lower ERVs compared to the sulfides.*

Figure 4.8 a)-c) shows the TRPL of WSe_2, WS_2, and $MoSe_2$ respectively, and the extracted ERVs of all four materials compiled at Figure 4.8 d) (individual ERV extractions are detailed in Figure 4.10). The extracted ERVs are 2 x 10^4 cm/s, 2.6 x 10^3 cm/s, 1.8 x 10^4 cm/s and 1.1 x 10^4 cm/s for MoS_2, $MoSe_2$, WS_2, and WSe_2 respectively. Generally, the selenides possess slightly lower values compared to their respective sulfide counterparts. Interestingly, $MoSe_2$ ERV is approximately an order smaller than the other three TMDs. This ERV variation corresponds very clearly to the much longer $\tau_{surface}$ of $MoSe_2$ (~116ns) compared to the $\tau_{surface}$ of the other three TMD (~3ns, ~10ns, and ~20ns for WS_2, MoS_2 with TFSI, and WSe_2 respectively).[16] This large material consistent ERV difference highlights the differences in the edge defect density as a function of the material rather than the etching process. Therefore, SPL demonstrates itself as an ideal lithography method for future ERV study due to the limited edge defects it creates during patterning.

4.6.1. Steady State PL of Selected TMDs

Steady state PL of all four TMDs, $MoSe_2$, MoS_2, WSe_2, and WS_2 are shown in Figure 4.9 after fill factor correction. This also clearly shows the edge defect recombination rate increasing as the disk diameter size shrinks.
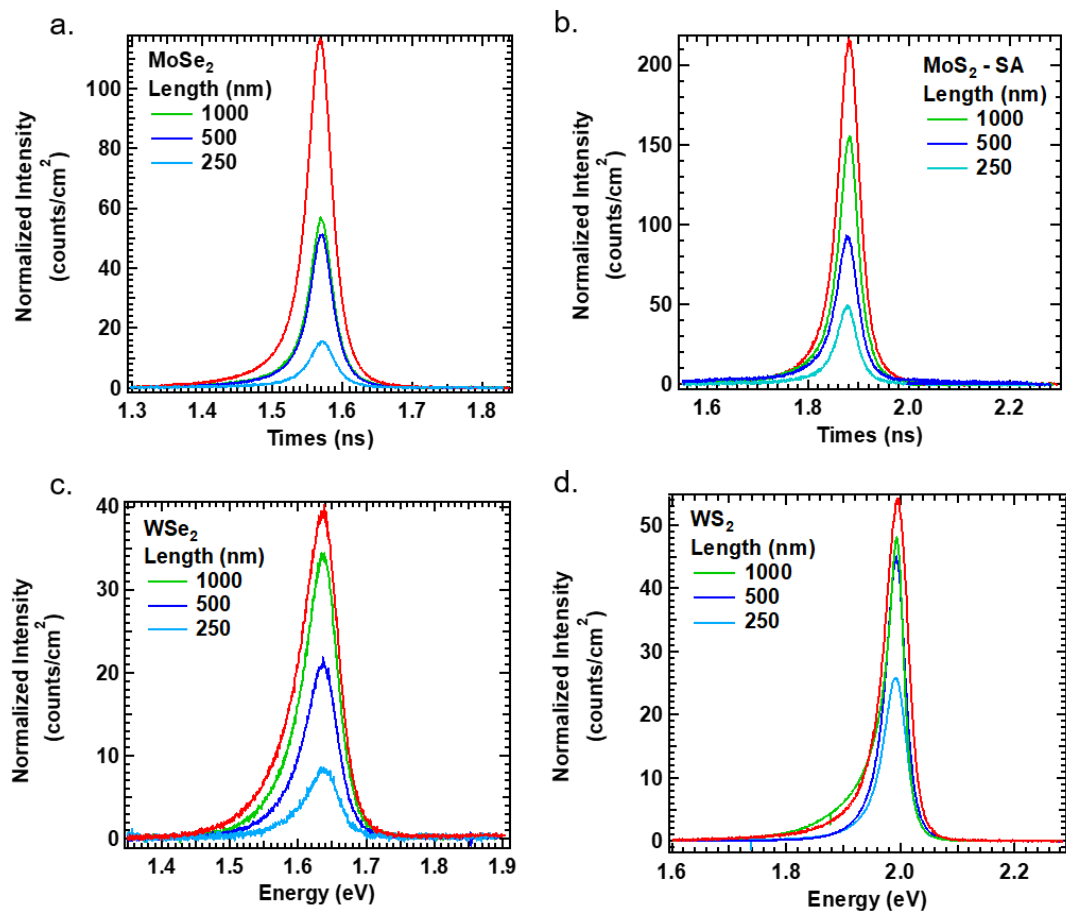
Figure 4.9. *Area normalized PL spectra of all four TMDs for all 3 sizes of interest. The red spectra in each graph signifies the intensity of a control monolayer without etching. The materials are a) MoSe₂ b) MoS₂ c) WSe₂ and d) WS₂ respectively.*

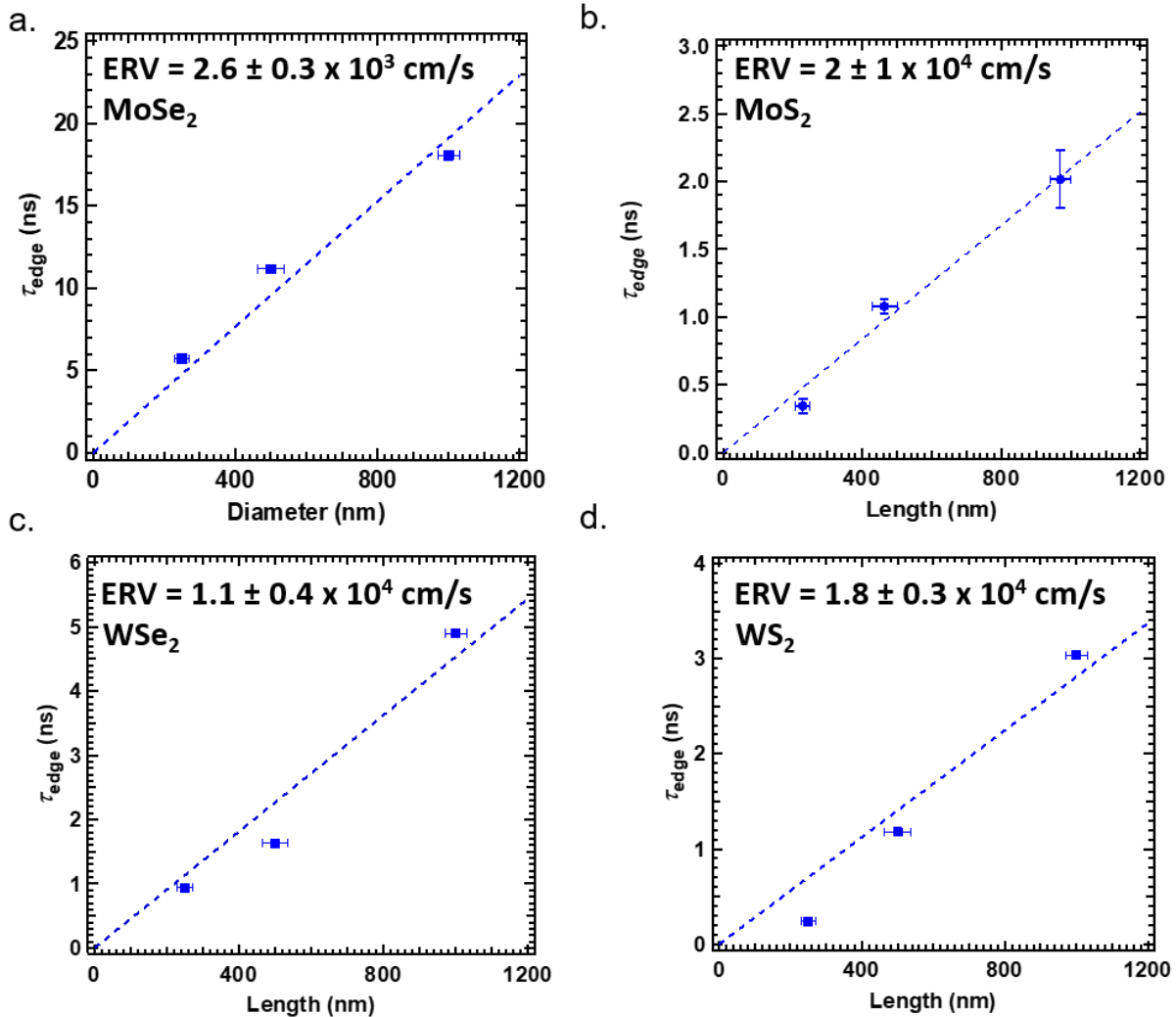### 4.6.2. τ_{edge} vs. Length of Selected TMDs

Figure 4.10. *Extracted τ_{edge} of all four TMDs for all 3 sizes of interest. The materials are a) MoSe₂ b) MoS₂ c) WSe₂ and d) WS₂ respectively. Note the significantly longer MoSe₂ edge lifetime reflective of its surface properties.*

τ_{edge} vs. Length of all four TMDs, $MoSe_2$, MoS_2, WSe_2, and WS_2 are shown in Figure 4.10. The corresponding extracted ERVs are also shown here for reference.

4.7 Conclusion

In conclusion, an in-depth investigation of the various parameters affecting SPL lithography is discussed. Voltage bias, amplitude setpoint, and humidity have all shown tunability on TMD monolayer oxidation consistent with known theory, reaching sub-100nm resolution. In addition, dwell time of SPL can used to control the thickness of oxidized multilayer TMDs, demonstrating the possibility of layer-by-layer oxidation control. Finally, SPL has been applied to four different TMD materials MoS_2, $MoSe_2$, WS_2, and

WSe$_2$. ERVs are extracted from the four patterned TMDs with a large variation between different material systems. The varied ERVs highlight the limited edge defects SPL creates during patterning, reinforcing SPL as a patterning technique towards future edge passivation and examination of material dependent edge structure variations.

REFERENCES:

1.   Knoll Armin, W.; Pires, D.; Coulembier, O.; Dubois, P.; Hedrick James, L.; Frommer, J.; Duerig, U. *Adv. Mater.* **2010,** 22, (31), 3361-3365.
2.   Garcia, R.; Knoll, A. W.; Riedo, E. *Nature Nanotechnology* **2014,** 9, 577.
3.   Chen, H.-A.; Lin, H.-Y.; Lin, H.-N. *The Journal of Physical Chemistry C* **2010,** 114, (23), 10359-10364.
4.   Avouris, P.; Martel, R.; Hertel, T.; Sandstrom, R. *Applied Physics A* **1998,** 66, (1), S659-S667.
5.   Ma, Y.-R.; Yu, C.; Yao, Y. D.; Liou, Y.; Lee, S. F., *Tip-induced local anodic oxidation on the native SiO2 layer of Si (111) using an atomic force microscope*. 2001; Vol. 64.
6.   Dago, A. I.; Ryu, Y. K.; Garcia, R. *Applied Physics Letters* **2016,** 109, (16), 163103.
7.   Espinosa, F. M.; Ryu, Y. K.; Marinov, K.; Dumcenco, D.; Kis, A.; Garcia, R. *Applied Physics Letters* **2015,** 106, (10), 103503.
8.   Kc, S.; Longo, R. C.; Wallace, R. M.; Cho, K. *Journal of Applied Physics* **2015,** 117, (13), 135301.
9.   Zhang, X.; Jia, F.; Yang, B.; Song, S. *The Journal of Physical Chemistry C* **2017,** 121, (18), 9938-9943.
10.   Liu, H.; Han, N.; Zhao, J. *RSC Advances* **2015,** 5, (23), 17572-17581.
11.   Bothra, S.; Sur, H.; Liang, V. *Microelectronics Reliability* **1999,** 39, (1), 59-68.
12.   Thierry Ondarcuhu, J.-P. A., *Nanoscale Liquid Interfaces: Wetting, Patterning and Force Microscopy at the Molecular Scale*. 1 ed.; Pan Stanford: New York, 2013.
13.   Takashi Kamikubo;   Takayuki Abe;   Susumu Oogi;   Hiroto Anze;   Mitsuko Shimizu; Masamitsu Itoh;   Tetsuro Nakasugi;   Tadahiro Takigawa;   Tomohiro Iijima;   Yoshiaki Hattori; Toru Tojo. *Japanese Journal of Applied Physics* **1997,** 36, (12S), 7546.
14.   James D. Plummer, M. D. D., Peter B. Griffin, *Silicon VLSI Technology: Fundamental, Practice, and Modeling*. Pearson Education: India, 2009.
15.   Amani, M.; Lien, D.-H.; Kiriya, D.; Xiao, J.; Azcatl, A.; Noh, J.; Madhvapathy, S. R.; Addou, R.; Kc, S.; Dubey, M.; Cho, K.; Wallace, R. M.; Lee, S.-C.; He, J.-H.; Ager, J. W.; Zhang, X.; Yablonovitch, E.; Javey, A. *Science* **2015,** 350, (6264), 1065.
16.   Amani, M.; Taheri, P.; Addou, R.; Ahn, G. H.; Kiriya, D.; Lien, D.-H.; Ager, J. W.; Wallace, R. M.; Javey, A. *Nano Letters* **2016,** 16, (4), 2786-2791.
17.   Zhao, P.; Amani, M.; Lien, D.-H.; Ahn, G. H.; Kiriya, D.; Mastandrea, J. P.; Ager, J. W.; Yablonovitch, E.; Chrzan, D. C.; Javey, A. *Nano Letters* **2017,** 17, (9), 5356-5360.
18.   Shockley, W., *Electrons and Holes in Semiconductors with Applications to Transistor Electronics*. D. Van Nostrand Company Inc.: Princeton, New Jersey, 1950.
19.   Wang, R.; Ruzicka, B. A.; Kumar, N.; Bellus, M. Z.; Chiu, H.-Y.; Zhao, H. *Phys. Rev. B* **2012,** 86, (4), 045406.

Chapter 5 Conclusion

In this final chapter we will recap and summarize the list of goals achieved in understanding and engineering the surface and edge defects of TMDs. Specifically, we will review the three projects separately and evaluate logical next steps expanding on the available findings. Finally, we will synthesize the information learned and evaluate the state of TMD surface and edge defect characterizations techniques towards future investigative research topics.

5.1 NO$_2$ Surface Functionalization
5.1.1. Summary
In chapter two, we demonstrate air stable p-doping, up to the degenerate limit, by chemisorption of NO$_2$ on WSe$_2$ performed at a sample temperature of 150 ^{o}C. Synchrotron-based soft X-ray absorption spectroscopy (XAS) and X-ray photoelectron spectroscopy (XPS) depict formation of various WSe$_{2-x-y}$O$_x$N$_y$ species upon NO$_x$ chemisorption on WSe$_2$. Formation of these species and their effects on the electronic properties of WSe$_2$ are also examined by *ab initio* simulations, which confirm the experimental observations. Notably, the chemisorption process retains WSe$_2$'s long-range crystal structure and optical properties. This doping process leads to a 5 orders of magnitude reduction in contact resistance (R_c) between WSe$_2$ and Pd metal, and results in a degenerate doping concentration of 1.6 x 10^{19} cm^{-3}. From this study, we display a route toward an air stable p-doping method on WSe$_2$ that can be efficiently utilized for various device schemes in the future.

5.1.2. Outlook and Challenges
While the project realized air stable degenerate p-doping and drastically reduce R_c, of WSe$_2$ based devices, two main challenges remain: process integration of the doping method and patternable doping.

The doping method, while air stable, experiences various unpredictability for device fabrication integration. During functionalization experiments, it is clearly seen that the doping process does not survive any solvent based process such as resist development or acetone submersion. Nor does the process survive any moderate to high temperature (>150 ^{o}C) treatment under other environments except inert noble gas (N$_2$ or Ar$_2$). Realistically, the straightforward solution is to incorporate doping as one of the last fabrication steps. This renders process integration incompatibility irrelevant. Obviously, this restriction will make achieving patternable doping much more challenging, as will be discussed below.

Other alternatives to improving functionalization stability against fabrication processing such as tuning chemical reaction is also a valid, though more complex topic of investigation. One interesting approach is to induce controllable intercalation of charged species directly into the van der Waals gaps. Much work has already been done in this area, but most of the doping involved utilizing column I or II atoms and therefore

results in n-type doping.[1, 2] However, the observed stability can be a point of interest for any bi-layer TMD devices or more.

On the other hand, patternable doping is also an important problem to solve in order to expand on the functionalization scheme into a practical framework. We realized during experiments that NO_2 diffusion can happen under standard resist masking and inferred from electrical results that interlayer penetration is also possible. This obviously underlines the difficulty in controlling the doping location. One possible approach is to design a TMD device in the PNP configuration ($WSe_2 - MoS_2 - WSe_2$ heterostructure for example), where after all relevant processing, a blanket p-type doping can be implemented, effectively rendering the channel semiconducting (or slightly n or p-type depending on the degree of compensation) while still leaving the contact areas degenerately p+ doped. The challenge here lies in the proper heterostructure stacking (out of plane or in-plane conduction) and the heterostructure fabrication itself such that R_c of heterostructure conduction does not overshadow the R_c improvement gained from surface functionalization.

5.2. Edge Recombination Velocity

5.2.1 Summary

Here, we introduce a metric called the edge recombination velocity (ERV) for 2D materials, to quantify the impact of edges on carrier recombination processes. ERV is defined as the total recombination events per unit time at the edge, divided by the product of perimeter length and excess carrier number per unit area. ERV is a direct measure of the tendency for an edge to enhance the recombination rate. Presumably, ERV depends on the detailed structure of the edge in question, and can, accordingly, be altered through chemical treatments akin to those used in surface passivation. We note that ERV in a 2D material is analogous to the surface recombination velocity (SRV) used to quantify the surface quality of 3D materials.[3] ERV can be extracted by characterizing the photoluminescence properties of patterned arrays of monolayer disks. We use tungsten disulfide (WS_2) monolayers as a model material system, measuring an ERV of ~4.4 x 10^4 cm/s after a chlorine plasma patterning.[4] The ERV value provides a baseline for 2D material edge quality and an assessment platform relevant to any optically active members of the 2D material family.

5.2.2 Outlook and Challenges

Having derived a relevant quantitative metric for evaluating edge quality, an obvious direction is to decrease the ERV of various materials (via passivation) in an attempt to improve edge quality. This is addressed in chapter 4 as a motivation of the SPL follow up and will be discussed in 5.3.2. In addition, ERV possesses the following relation:

$$\text{ERV} = {N_t}/{l} \, (\sigma_{1D} v_{th}) \qquad (1)$$

We inferred the edge defect density (N_t/l) in chapter 3 via a reasonable assumption of the capture radius (σ_{1D}) along with the exciton thermal velocity (v_{th}). However, capture cross section of various surface defects can vary widely depending on the material and the measurement technique applied. This is seen clearly in 3D materials in relation to SRV measurements.[5] We expect the same for the 2D material case. Therefore, ERV can also be leveraged as a metric to capture the more elusive aspects of the TMD physics, such as different defect capture radius (or their corresponding trap states within the bandgap) and the excitonic thermal diffusion mechanisms.

Additionally, ERV is probed optically, measuring the number of non-radiative recombination centers at the edge. Various DFT simulations have yielded results implying non-radiative recombination of zigzag edges, even under "pristine" condition.[6] If experiments are consistent with DFT simulations, this implies that a completely "perfect" edge can be achieved while a non-zero density of non-radiative recombination edge sites still exists. This means that ERV can be potentially used in the future to directly ascertain the percentage of zigzag/armchair characteristic of any relevant TMD nanostructure given close to perfect edge passivation/fabrication methods are available.

Finally, the utility of ERV can be drastically extended when more aspects of the TMD material can be understood, underlining the metric's potential in further advancing the understanding of the TMD material system.

5.3. Scanning Probe Lithography and ERV Extension

5.3.1 Summary

Scanning probe lithography (SPL) has been previously utilized to pattern various TMDs of differing thickness.[7, 8] In chapter 4, we expand on this patterning platform to monolayer MoS_2, $MoSe_2$, WS_2, and WSe_2 while investigating the various parameters that can affect the oxidation process, such as tip bias, dwell time, humidity, and setpoint amplitude. By fine tuning the aforementioned parameters, we demonstrate the SPL oxidation resolution of <100nm in width and a tunable oxidation depth from varying the pixel dwell time. In addition, we extract ERVs of four aforementioned TMD members patterned via SPL and demonstrate 10x variation between different TMD members. This variation highlights the reduced impact SPL has on the ERV itself and highlights the intrinsic edge properties of the material in question.

5.3.2. Outlook and Challenges

While SPL patterned ERV has shown material variation, a variety of treatments (similar to the methods mentioned in Table 4.1) conducted on the SPL edges have also influenced the observed PL intensity in various ways. This means that SPL edges are more susceptible to passivation schemes than dry etched edges (chapter 3) and stresses the need at finding the proper edge passivation scheme in the future.

To achieve maximum radiative recombination at the edge, edge structures can either be chemically passivated, or modified to create local band bending that reflects the carriers back into the surface for radiative recombination similar to that of SRV.[9] The

obvious complication stems from the fact that excitons are intrinsically neutral in charge and are insusceptible to drift fields after formation. However, energy barriers can still be introduced to stem the flow of excited electron or hole carriers by driving the carriers (via an electric potential) towards the surface before excitonic formation.

5.4 Future Work

This thesis has tackled TMD defects from different directions: surface defect engineering via covalent functionalization, edge defect characterization via optical probing techniques, and expanding the ERV characterization platform via a patterning method (scanning probe lithography) that limits the impact of process induced defects on the edges while emphasizing the material associated intrinsic edge defects themselves.

While the first project is more of a "proof of concept" that demonstrates the importance of strong chemical binding for future practical charge transfer techniques applied towards carrier modulation of TMDs, this author hopes that the introduction of ERV, and SPL defined edges, can help pave the way towards a systematic understanding of the TMD edge properties, and gives a clear direction in driving future edge-related TMD innovations towards a quantifiable and practical goal.

REFERENCES

1.   Zeng, Z.; Yin, Z.; Huang, X.; Li, H.; He, Q.; Lu, G.; Boey, F.; Zhang, H. *Angew. Chem. Int. Ed.* **2011,** 50, (47), 11093-11097.
2.   Deshpande, M. P.; Patel, P. D.; Vashi, M. N.; Agarwal, M. K. *J. Cryst. Growth* **1999,** 197, (4), 833-840.
3.   Shockley, W., *Electrons and Holes in Semiconductors with Applications to Transistor Electronics*. D. Van Nostrand Company: Princeton, New Jersey, 1950.
4.   Lin, T.; Kang, B.; Jeon, M.; Huffman, C.; Jeon, J.; Lee, S.; Han, W.; Lee, J.; Lee, S.; Yeom, G.; Kim, K. *ACS Appl. Mater. Interfaces* **2015,** 7, (29), 15892-15897.
5.   J. M. Langer, W. W. In *Surface Recombination in Semiconductors*, International Conference on Defects in Semiconductors, Sendai, 1995; Sendai.
6.   Li, Y.; Zhou, Z.; Zhang, S.; Chen, Z. *J. Am. Chem. Soc.* **2008,** 130, (49), 16739-16744.
7.   Dago, A. I.; Ryu, Y. K.; Garcia, R. *Appl. Phys. Lett.* **2016,** 109, (16), 163103.
8.   Espinosa, F. M.; Ryu, Y. K.; Marinov, K.; Dumcenco, D.; Kis, A.; Garcia, R. *Appl. Phys. Lett.* **2015,** 106, (10), 103503.
9.   Schnitzer, I.; Yablonovitch, E.; Caneau, C.; Gmitter, T. J. *Appl. Phys. Lett.* **1993,** 62, (2), 131-133.